A Unified Probabilistic Computational Framework for Cross-Domain Compensated Medical Imaging

by

Ameneh Boroomand

A thesis
presented to the University of Waterloo
in fulfillment of the
thesis requirement for the degree of
Doctor of Philosophy
in
Systems Design Engineering

Waterloo, Ontario, Canada, 2016

This thesis consists of material all of which I authored or co-authored: see Statement of Contributions included in the thesis. This is a true copy of the thesis, including any required final revisions, as accepted by my examiners.

I understand that my thesis may be made electronically available to the public.

Statement of Contributions

The following papers are used in this thesis. They are described below:

A. Boroomand, B. Tan, A. Wong, and K. Bizheva, "Axial resolution improvement in spectral domain optical coherence tomography using a depth-adaptive maximum-a-posterior framework," in SPIE Photonics West (BiOS), Vol. 9312, pp. 931241–931241, March 2015.

This paper is incorporated in Chapter 4 of this thesis.

Contributor	Statement of Contribution
A. Boroomand (Candidate)	Conceptual design (80%)
	Data analysis(90%)
	Writing and editing (80%)
B. Tan	Data collection (80%)
A. Wong	Conceptual design (20%)
	Data analysis (10%)
	Writing and editing (10%)
K. Bizheva	Data collection (20%)
	Writing and editing (10%)

A. Boroomand, M.J. Shafiee, A. Wong, and K. Bizheva, "Lateral resolution enhancement via imbricated spectral domain optical coherence tomography in a maximum-a-posterior reconstruction framework," in SPIE Photonics West (BiOS), Vol. 9312, pp. 931240-931240, March 2015.

This paper is incorporated in Chapter 4 of this thesis.

Contributor	Statement of Contribution
A. Boroomand(Candidate)	Conceptual design (80%)
	Data analysis(90%)
	Writing and editing (70%)
M.J Shafiee	Conceptual design (10%)
A. Wong	Conceptual design (10%)
	Data analysis (10%)
	Writing and editing (20%)
K. Bizheva	Data experiments (100%)
	Writing and editing (10%)

A. Boroomand, A. Wong, and K. Bizheva, "A Stochastically Fully Connected Conditional Random Field Framework for Super Resolution OCT," accepted for presenting in SPIE Photonics West (BiOS) conference, Feb 2017.

This paper is incorporated in Chapter 5 of this thesis.

Contributor	Statement of Contribution
A. Boroomand (Candidate)	Conceptual design (80%)
	Data analysis(90%)
	Writing and editing (80%)
A. Wong	Conceptual design (20%)
	Data analysis (10%)
	Writing and editing (10%)
K. Bizheva	Data experiments (100%)
	Writing and editing (10%)

A. Boroomand, M.J. Shafiee, F. Khalvati, M. Haider and A. Wong, "Noise-Compensated, Bias-Corrected Diffusion Weighted Endorectal Magnetic Resonance Imaging via a Stochastically Fully-Connected Joint Conditional Random Field Model," in IEEE Trans Med Imaging, Vol.PP, 2016.

This paper is incorporated in Chapter 6 of this thesis.

Contributor	Statement of Contribution
A. Boroomand (Candidate)	Conceptual design (70%)
	Data analysis(100%)
	Writing and editing (70%)
M.J Shafiee	Conceptual design (10%)
	Writing and editing (10%)
F. Khalvati	Data experiment (80%)
	Writing and editing (10%)
M. Haider	Data experiment (20%)
	Results evaluation (100%)
A. Wong	Conceptual design (20%)
	Writing and editing (10%)

A. Boroomand, M.J. Shafiee, F. Khalvati, M. Haider and A. Wong, "A Unified Bayesian-Based Compensated Magnetic Resonance Imaging," in 38th Annual International Conference of the IEEE Engineering in Medicine and Biology Society (EMBC), Orlando, USA, August 2016.

This paper is incorporated in Chapter 6 of this thesis.

Contributor	Statement of Contribution
A. Boroomand (Candidate)	Conceptual design (70%)
	Data analysis(100%)
	Writing and editing (80%)
E. Li	Writing and editing (5%)
M.J Shafiee	Conceptual design (10%)
F. Khalvati	Data experiment (80%)
	Writing and editing (5%)
M. Haider	Data experiment (20%)
	Results evaluation (100%)
A. Wong	Conceptual design (20%)
	Writing and editing (10%)

Abstract

The quality of medical imaging is an important factor that can directly affect on the results of different medical imaging tests which routinely being used for various clinical studies and related research. The existence of any type of image imperfection such as different noise and artifacts can make some difficulties for the correct analyzing and consequent interpretation of medical imaging test results and even may impact on the overall decision of the performed clinical procedure. Due to this issue, there is always a motivation for the quality enhancement of medical imaging that needs to be done by correcting for the different image degradation that typically arise during medical image capture or reconstruction.

Computational compensated imaging provides a useful, cheap and easy solution for the quality enhancement of different types of medical imaging when it compares to the similar hardware-based compensation methods. A computational compensated medical imaging basically aims to recover a compensated (true) image from degraded medical measurement that is affected by the different types of acquisition/reconstruction image degradation. Compensating for each single image degradation issue can be useful for the quality improvement of medical imaging. Having a computational compensated imaging framework to jointly correct for multiple acquisition/reconstruction degradation issues can improve the functionality of current existing compensated imaging frameworks as they mostly account only for a single specific type of degradation issue.

This work presents a novel probabilistic based computational compensated medical imaging which is able to jointly account for several acquisition/reconstruction degradation issues from the different domains in a unified computational framework. The developed computational cross-domain compensated medical imaging specifically takes advantage of a stochastically fully connected conditional random field (SFC-CRF) model in its framework which improves the performance of the proposed compensated medical imaging in producing of a desired compensated medical image.

A compensated optical coherence tomography (C-OCT) imaging is developed within the framework of proposed computational cross-domain compensated medical imaging and with aiming to jointly compensate for the degradation due to the optical aberrations and speckle noise in OCT imaging. The developed C-OCT imaging is expanded to design a compensated super resolution OCT (C-SR-OCT) imaging framework which is able to generate a super resolution OCT (SR-OCT) image of higher quality from multiple OCT measurements. The proposed computational cross-domain compensated medical imaging is also used to develop a compensated magnetic resonance imaging (CMR) framework which aims to improve the quality of MR imaging from different modalities by jointly correcting

for the MR image degradation due to the intrinsic properties of MR scanner, bias field inhomogeneities and inherent MR noise. The results of all three designed compensated medical imaging platforms for the OCT imaging and MR imaging elaborate the promising efficacy of proposed probabilistic based computational compensated medical imaging framework for the quality enhancement of different medical imaging techniques.

Acknowledgements

I would like to express my sincere gratitude to my supervisors Professor Alexander Wong and Professor Kostadinka Bizheva for their guidance, advice, and moral support throughout my Ph.D. studies under their supervision. They have contributed enormously to my growth as a researcher.

I wish to thank my doctoral committee members, Prof. John Zelek, Prof. Andrea Scott, prof. Mahmoud El-Sakka and Prof. Luigina Sorbara for their valuable comments and suggestions.

I wish to acknowledge the University of Waterloo Faculty of Engineering, and the Natural Sciences and Engineering Research Council (NSERC) of Canada for financial support of my research.

I would also like to thank my friends and colleges in the Vision and Image Processing (VIP) lab and all my dear friends and colleagues at University of Waterloo for their support during these years.

Finally, I would like to express my deepest gratitude and love to my parents for their unconditional love and support. My special gratitude and love goes to my dear sisters Arefeh, Alaleh and Ghazaleh for all their continuous support and encouragement.

Dedication

To my loved ones, my beloved parents and sisters.

Table of Contents

List of Tables

List of Figures

Nomenclature

A_k	Regarded OCT measurement in K-space
b	Bias field inhomogeneity
c	Clique structure
c_p	Pairwise clique structure
$\mathbb{C}$	Compensation function
C	Set of clique structures
$\mathbb{C}_{ps}$	Prostate class in Bayes classifier
$\mathbb{C}_b$	Background class in Bayes classifier
d_{Aq}	Acquisition degradations
d_{Rec}	Reconstruction degradations
D	Degradation function
D_{sup}	Super resolution degradation function
D_{sys}	System characteristic function
E	Energy function
E^{sup}	Energy function in modeling of super resolution compensated imaging.
f^u	Unary feature function
f^p	Pairwise feature function
$\mathbb{F}$	Data fidelity model
$\mathcal{F}$	Fourier transform
G	Graphical model
h_{MR}	Intrinsic properties of the MR scanner
H	OCT optical aberrations
J	Objective function
J_{FC}	Fisher criterion metric
L	Likelihood term
$\mathcal{L}$	Discrete lattice
M	Degraded measurement
M^{new}	New data observation
n	Number of pixels
$\aleph$	Noise
$\aleph_{spk}$	Speckle noise
P	Probability function
$P(e)$	Probability of error
P^{SD}	Spatial similarity probability distribution
P^D	Data similarity probability distribution

R	Regularization function
S	Random field space
t	Iteration
V	Potential function
w^u	Control parameter for unary term in CRF model
w^p	Control parameter for pairwise term in CRF model
w^h	Control parameter for higher order potential in HCRF model
w^c	Control parameter for higher order potential in FC-CRF model
W	Number of multiple data measurements
Y	True compensated image
Y^G	Ground truth MR phantom image
Z	Normalization term in CRF model
ρ	Learning rate of gradient based optimization method
ς	Regularization parameter
Ω	Set of all admissible solutions compensated image
Υ	Graph sparsity threshold
σ	Standard deviation
σ_{cl}	Parameter for control effect of pairwise term in C-SR-OCT imaging
σ_r	Variance of a selected image ROI
σ_{ps}	Variance of a selected ROI on prostate gland
ϱ	hyper-parameter in blind compensated imaging
μ_r	Mean value for selected image ROI
μ_{ps}	Mean value for selected ROI on prostate gland
N	Pixel neighborhood
Ψ_h	Higher order potential function
Ψ_u	Unary potential function
Ψ_p	Pairwise potential function
Ψ_u^{sup}	Unary potential function in formulation of super resolution compensated imaging
Ψ_p^{sup}	Pairwise potential function in formulation of super resolution compensated imaging
Θ	CRF model parameters
Θ_h	HCRF model parameters
Θ_h	HCRF model parameters
τ_{sr}	Parameter for control distance based unary term in C-SR-OCT imaging.
ι	Stochastic indicator function
ϑ	Set of graph nodes
§	Set of graph edges

Chapter 1

Introduction

Medical imaging techniques are an important and critical compartment of today's medicine which are required for performing many different medical procedures and clinical tests. Taking advantage of different medical imaging techniques facilitates the disease investigation and follow-up procedure and also can help in earlier diagnosis and proper treatment planning for the cure of many diseases. The results of any medical imaging test should be analyzed and interpreted with the help of an expert radiologist or with taking advantage of specifically designed automatic/semi-automatic processing softwares which aim to analyze and interpret the result of medical imaging by performing different processing tasks.

The correct interpretation and analyzing of medical images is highly dependent on the overall quality of acquired medical image such that any image imperfection may affect on the correct visualization of the results and therefore make some complication for the further required analysis and interpretation. Obtaining of medical images with higher quality leads to the better representation of different details, features and structures of the imaged tissue/organ such that can improve the validity of different required analysis as well as results interpretations that needs to be done by an expert or using various automatic/semi-automatic image processing softwares.

In general, all types of medical images suffer from a combination of image degradation issues that overall reduce the quality of acquired medical image and hence negatively impact on the optimal visualization of the different features, details and structures of the imaged tissue/organ. Different types of acquisition and reconstruction degradation issues may cause by some physical limitations of medical imaging system, using of a sub-optimal image reconstruction algorithms or due to the different specific properties and features of the tissue/structure that can intervene with the imaging procedure, all together result in

some imperfections on captured image.

Correcting for each single acquisition/reconstruction degradation issue is solely important for the quality enhancement of an acquired medical image. Compensated medical imaging technique generally aims to produce a compensated image from obtained degraded medical acquisition and by accounting for various types of acquisition and reconstruction degradation issues.

Many efforts have been done to develop both hardware-based and computational based compensated imaging techniques and to correct for the different acquisition/reconstruction degradation issues that commonly happen with the use of different types of medical imaging systems. Taking advantage of hardware-based image compensation techniques always need to do a modification on the design of the imaging system or to add a new hardware component to the system and therefore is more challenging and also highly costly when it compares to the similar computational image compensation approaches. In addition, any of the hardware-based medical image compensation techniques is only able to correct for a specific medical image degradation issue.

Computational compensated imaging methods often provide an easier and cheaper solution for the correction of different types of acquisition/reconstruction image degradation issues. Some computational compensated imaging methods are versatile and can be applied to the different types of medical imaging systems and with a small algorithm modifications or even with no change. Furthermore, using of computational compensated imaging technique is advantageous since it can be designed such that account for the multiple image degradation issues in a unified computational framework. Due to all these features, computational compensated imaging methods are growing fast for the aim of medical image compensation.

1.1 Motivation

Most of the previously proposed computational compensated imaging frameworks which have been used for the aim of quality enhancement in different types of medical imaging only account for a single image degradation issue or sequentially perform multiple compensation tasks using separate processing steps, when each step only correct for a single image degradation issue. Designing of a unified computational compensated imaging framework which jointly corrects for multiple image degradation issues can be beneficial for the following reasons:

- Having a unified computational compensated imaging framework provides a more optimized, cheaper as well as easier solution for performing of compensated medical imaging when it compares to the similar hardware approaches. Jointly correcting for several degradation issues is nearly impossible with the use of hardware-based compensation techniques. According to these, there is a great motivation to design a computational compensated imaging framework which is able to jointly correct for the different types of image degradations in a unified compensation framework.

- Employing of some conventional compensation methods to correct for a specific image degradation sometimes causes to another degradation issue or may increase the effect of some other degradations which are undesired. For example, conventional methods for the bias field inhomogeneities correction in magnetic resonance imaging may lead to the MR noise amplification in produced compensated image. In such a situation, adding another compensation step to correct for the secondary image degradation is necessary. Having a unified computational compensated imaging framework which jointly corrects for the both primary degradation issue and the effect of secondary raised degradation issue can optimize the performance of compensated imaging and consequently more enhances the overall quality of the produced compensated image.

- A computational compensated imaging model which has the ability of correcting for multiple image degradation factors from both reconstruction and acquisition types within a unified computational framework, can potentially reduce the complexity and processing time of the whole compensated imaging procedure. This is beneficial for many different required medical image processing and analyzing tasks that should be performed in real-time.

1.2 Thesis Contributions

- Designing and developing of a unified probabilistic computational cross-domain compensated medical imaging framework which is able to jointly correct for multiple image degradation issues is the main contribution of this thesis. This is described in detail in Chapter 3.

- The proposed probabilistic computational cross-domain compensated medical imaging framework provides a general image compensation model that can be easily modified to be used with different types of medical imaging systems and also to compensate for a variety of different acquisition and reconstruction image degradation factors.

- The developed probabilistic based compensated medical imaging framework takes advantage of a newly designed stochastically fully connected conditional random field (SFC-CRF) model in its framework, which improves the overall performance of proposed compensated imaging. Adding of SFC-CRF model to the design of proposed compensation framework is helpful for the incorporation of different structural knowledge about the imaged tissue/organ to the compensation framework. Using of any prior knowledge about the desired medical image can potentially improve the overall performance of the designed compensated imaging framework in reconstruction of a more true compensated image.

- The proposed probabilistic computational compensated medical imaging framework provides a cross-domain platform for performing of compensated medical imaging. Hence, image degradations from different domain spaces can be handled together using a unified compensated medical imaging framework.

- A compensated optical coherence tomography (C-OCT) imaging is developed within the framework of proposed probabilistic cross-domain compensated medical imaging as explained in Chapter 3 and presented in Chapter 4. The developed C-OCT imaging is able to generate compensated OCT images by jointly correcting for the optical aberrations and speckle noise which are recognized degradation issues in all types of OCT imaging.

- A compensated super resolution OCT (C-SR-OCT) model is developed with taking advantage of proposed probabilistic computational cross-domain compensated medical imaging framework of Chapter 3 as presented in Chapter 5. The designed C-SR-OCT framework is able to generate SR-OCT images of higher quality with taking advantage of multiple OCT acquisitions when it jointly accounts for the aberration caused by the OCT system, motion artifact and speckle noise which are common issues in OCT imaging.

- A compensated magnetic resonance (CMR) imaging framework is developed with using the proposed probabilistic cross-domain compensated medical imaging of Chapter 3 and presented in Chapter 6. The developed CMR imaging aims to account for the different degradation issues in MR imaging including MR aberrations due to intrinsic properties of MR scanner, bias field inhomogeneity and MR noise which all destroy the quality of MR imaging.

Chapter 2

Background

This chapter provides the required background and information related to the proposed computational compensated medical imaging framework. Compensated medical imaging is presented as a general inverse problem in Section 2.1. An overview of the most conventional methods for solving of the compensated imaging inverse problem is provided in Section 2.2. Blind compensated imaging is introduced in Sections 2.3 as an important class of compensated medical imaging which mainly focuses on the system related degradation compensation in medical imaging. Super resolution image compensation technique is introduced in Section 2.4 as a suitable approach for performing of compensated medical imaging in presence of multiple acquisitions. In addition, the main concept and theory behind random field modeling is explained in Section 2.5 when the conditional random field model (CRF) is presented as a well-known type of random field that could be incorporated to the different compensated imaging frameworks. Furthermore, the fully connected conditional random field (FC-CRF) model is introduced as an extension of standard CRF in Section 2.6 when it is compared to the standard CRF. A stochastic variant of the FC-CRF model is incorporated to the unified probabilistic cross-domain compensated medical imaging framework that is proposed in this thesis.

2.1 Compensated Medical Imaging

In all different types of medical imaging, the acquired medical image often provides a sub-optimal representation of the imaged tissue/organ structures due to the effect of different acquisition/reconstruction degradation factors that arise in using of various types of medi-

cal imaging techniques. Therefore, the degraded image needs to be compensated to provide a better representation of the different details and structures of the imaged tissue/organ.

Different types of medical imaging systems are equipped with the specific hardware components to compensate for the various types of acquisition/reconstruction image degradations. However, adding a hardware image compensation component to the medical imaging system is often a challenging task, needs to modify the designing of the system as well as is usually expensive. Computational compensated imaging techniques are now more of interest as they provide cheaper and easier solution for compensating of different acquisition/reconstruction degradations in various types of medical imaging systems.

A computational compensated imaging method generally aims to recover a compensated (true) image from degraded measurement that is affected by the different types of acquisition/reconstruction degradation factors.

Suppose that Y is the true image that aims to be recovered from the degraded measurement M, then the medical imaging process can be modeled as a general forward problem,

$$M = D(Y), \tag{2.1}$$

that represents the explicit relation between the true image Y and measurement M using the degradation function $D(.)$. In general, different types of acquisition/reconstruction degradations can be incorporated to the modeling of degradation function $D(.)$ when all deteriorate the overall quality of the acquired medical image. For many of the medical imaging systems and depending on the type of image degradation, the degradation function $D(.)$ can be assumed as a linear shift-invariant function such that the forward problem of Eq. (2.1) can be simply represented using a linear forward model. In addition, the measurement M and the true image Y could be assumed in a same domain, for example both can be in a spatial domain, or they can be defined in a cross-domain such as spatial-k-space or spatial-Fourier domains.

According to the forward problem of Eq. (2.1), a compensated medical imaging framework can be generally modeled as a inverse problem,

$$Y = \mathbb{C}(M) = D^{-1}(M), \tag{2.2}$$

where, $\mathbb{C}(.) = D^{-1}(.)$ refers to the compensation function that aims to compensate for the different types of acquisition/reconstruction degradations that negatively affects on the overall quality of the acquired medical image. A general diagram for both forward model of Eq. 2.1 and inverse model compensated medical imaging of Eq. 2.2 are shown in Fig. 2.1.

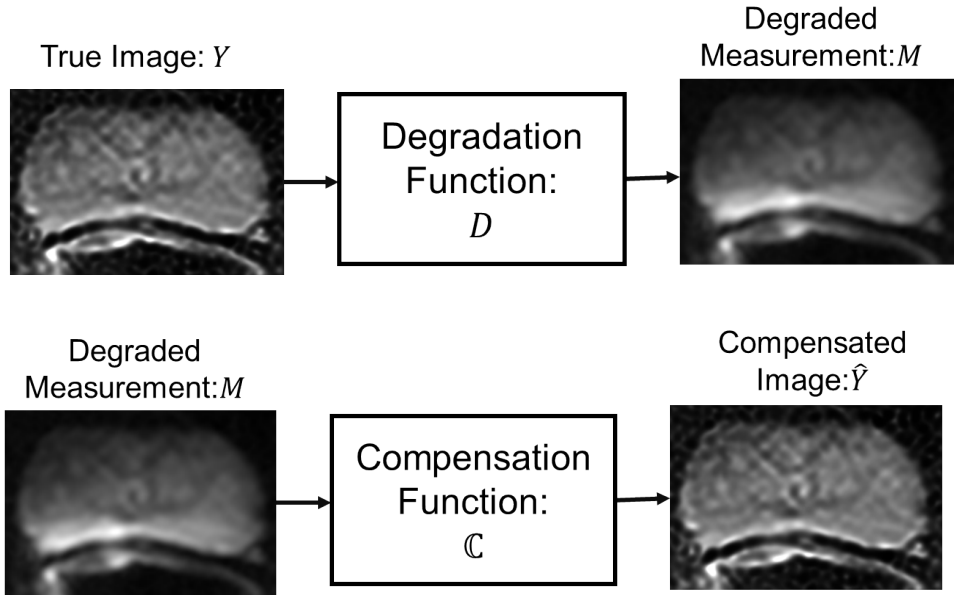

Figure 2.1: A general diagram for the compensated medical imaging model (top row) forward model, (bottom row) inverse model.

To perform compensated medical imaging, the inverse problem of Eq. (2.2) should be solved through an optimization step,

$$\hat{Y} = \underset{Y \in \Omega}{arg\,min}\ J(Y). \tag{2.3}$$

Here, J represent an objective function that should be minimized to find the best estimate of the true compensated image $\hat{Y}$ when Ω denotes to the set of all admissible solutions for image Y.

One main issue with the general inverse problem of Eq. (2.2) is the ill-possessedness characteristics of the problem, meaning that the solution of the inverse problem (here, the true compensated image Y) does not satisfy at least one of the existence, uniqueness, or stability conditions [44]. Therefore, this issue needs to be accounted in designing of the optimization step of Eq. 2.3 and to be able to find the best estimate of the compensated image, $\hat{Y}$, by solving the inverse problem of Eq. 2.2. Some of the general existing methods for solving of the inverse problem of Eq. (2.2) are reviewed in Section 2.2.

2.2 Methods for Solving of Compensated Imaging Inverse Problem

A large number of different computational methods are proposed to solve the general inverse problem of Eq. (2.2) and for the aim of compensated imaging when the most conventional approaches are grouped as follows:

1. Regularization Method
2. Bayesian Method

These methods are shortly reviewed in the following subsections.

2.2.1 Regularization Method

Solving the inverse problem of Eq.(2.2) and obtaining a stable solution for the aimed compensated image, $\hat{Y}$, is always challenging due to the different uncertainty factors such as noise and various types of artifacts that may arise in the process of medical image acquisition or reconstruction and using any type of medical imaging system. The solution of compensated imaging inverse problem is only reliable under the condition that being stable against the different uncertainty factors. Therefore, to find a stable solution for the compensated imaging inverse problem as well as to prevent from the over-fitting issue, most of the proposed computational methods take advantage of a regularization strategy to enforce the solution of compensated imaging inverse problem to be stable.

A general form of a regularization method to solve the inverse problem of Eq. (2.2) can be written as,

$$\hat{Y} = \underset{Y \in \Omega}{arg\,min}\ J(Y) = \underset{Y \in \Omega}{arg\,min}\{F(Y) + \varsigma R(Y)\} \tag{2.4}$$

where, $F(.)$ represent how well the optimization model fits the measurement (data fidelity term) and $R(.)$ is a regularization function. Here, ς is the regularization parameter which aims to maintain a proper balance between the amount of data fidelity and enforced regularization on the solution of the inverse problem [43]. Choosing a proper ς is important for finding the best estimate of the inverse problem solution. Different methods are proposed to determine the best value of the regularization parameter, when the most popular ones are as follows:

- **Visual inspection:** This way of regularization parameter setting is applicable for the case that the viewer has a pre-knowledge about the true compensated image and how it should be look like. In such a case, the visual inspection of the results can help to select the best value for the regularization parameter and through an empirical experiment procedure [43].

- **L-Curve method:** In this form of regularization parameter selection, compensated imaging being performed using different values of regularization parameter ς and the data fidelity term being plotted against the prior term when the plot is in a L-shape curve. Using this L-shape plot, the optimal value for the regularization parameter can be defined as the corner point of the curve [45, 18].

- **Generalized cross-validation (GCV) method:** The GCV method works based on the idea that, finding the inverse problem solution with taking advantage of all observations except one should be able to predict the left observation with the minimum prediction error. The optimal value of the regularization parameter can be calculated by minimizing the prediction error and using a search technique or optimization strategy [105, 104, 84].

In regularization based compensated medical imaging approach, the regularization function, $R(.)$, basically enforces a prior information over the final solution of the true compensated image, Y. The enforced prior information often can be determined based on the different characteristics and features of the imaged tissue/organ. For example, the smoothness of the imaged tissue at homogeneous regions or the presence of different sharp details and features such as edges and boundaries can be used as the prior information.

Based on the specific type of the constraint that aims to be enforced on the final solution of the true image Y and according to the different goals of compensated medical imaging, various types of regularization functions using different kind of norms and energy functions are being proposed.

1. **Tikhonov regularization [154]:** This is a popular regularization function which has been used with different compensated imaging algorithms. In general, Tikhonov regularization takes advantage of a form of image energy function such as, $R(Y) = \|Y\|_q$ or $R(Y) = \|\nabla Y\|_q$ to enforce the desired constraint on the final solution of compensated imaging inverse problem in Eq. 2.4. Here, $\|.\|_q$ is the Euclidean norm and ∇ is a gradient function. Two different forms of Tikhonov based regularization function are explained here.

- $R(Y) = \|Y\|_1$: Image energy function using ℓ_1 norm is a suitable option for enforcing more sharpness and sparseness on the final estimate of compensated medical imaging. This is due to the fact that the image energy function using ℓ_1 norm leads to the more Laplace form distribution which has a heavy-tail compared to the ℓ_2 norm that results in a Gaussian distribution for the image energy function.
- $R(Y) = \|\nabla Y\|_1$: Defines an energy function using the image gradient distribution. This has been introduced as a useful regularization function for the aim of different compensated medical imaging tasks. The famous total variation (TV) regularization as proposed in [132] takes advantage of the image gradient distribution for the regularization function. Using the image gradient distribution with ℓ_1 norm in TV leads to the better preserving of image discontinuities such as edges in the final estimate of compensated image $\hat{Y}$ and compared to the using of ℓ_2 norm $\|Y\|_2$ [171].

2. $R(Y) = \sum_{c \in C} V_c(Y)$: This is a typical form of regularization function using Markov random field modeling (MRF) which has been incorporated in different compensated imaging algorithms. MRF based regularization function basically takes advantage of a specifically designed potential function $V_c(.)$ which models the local interactions among the data and with c denoting a clique structure including a set of data sites (image pixels/voxels) in a specified neighborhood and C refers to the set of all possible clique structures. Summation over all the clique structures determines the overall data (image) energy. Different types of structural properties can be incorporated to the MRF based image compensation framework with the use of specific designed clique potential functions.

2.2.2 Bayesian Method

Bayesian based methods provide a statistical approach for computational compensated medical imaging as they effort to solve the inverse problem of Eq.(2.2) with assuming both measurement M and compensated true image Y in a random space [59, 51, 168, 150]. Withins such a statistical framework, different inherent measurement/system related uncertainties that typically exist in all different medical imaging systems can be incorporated to the compensated medical imaging inverse problem and through the Bayes rule [46]. Bayesian methods are recognized as a strong way of inferring unobservable data (here, true compensated image Y), given some observations (here, degraded measurement M).

According to the Bayes rule, the probability of the compensated true image Y given the measurement M is proportional to the,

$$P(Y|M) = \frac{P(Y)P(M|Y)}{P(M)} \tag{2.5}$$

where, $P(M)$ is the prior probability for measurement M. Two main variants of conventional Bayesian based methods that are widely used in the literature for the aim of image enhancement [101, 102, 67, 50] as well image reconstruction [15, 144, 16] are the Maximum Likelihood (ML) and Maximum a Posteriori estimation (MAP) as briefly explained here.

- **Maximum Likelihood Estimation**: In the Maximum Likelihood (ML) based compensated imaging context, the goal is to maximize the probability distribution of measurement, M, given the true compensated image, Y, among all possible solutions for Y according to,

$$\hat{Y}_{ML} = \underset{Y \in \Omega}{arg\,min}\ J_{ML}(Y) = \underset{Y}{arg\,min}\,(-log(P(M|Y)) \tag{2.6}$$

where, $L = P(M|Y)$ is known as the likelihood term. For many of compensated medical imaging approaches, it is assumed that the data (measurement) uncertainties can be modeled as zero-mean independent identically distributed (iid) Gaussian random variables which degrade the the overall quality of acquired measurements [88, 118]. In such a scenario, the likelihood term can be modeled as,

$$L = P(M|Y) = \prod_{i=1}^{n} \frac{1}{\sigma\sqrt{2\pi}} exp\left(-\frac{1}{2\sigma^2}(m_i - C(y_i))\right) \tag{2.7}$$

where, σ is the noise standard deviation and m_i, y_i respectively denote to the degraded measurement as well as compensated image at each single location i defined over the assumed random space of n sites. Accordingly, the ML based compensated medical imaging of Eq. (2.6) can be rewritten as,

$$\hat{Y}_{ML} = \underset{Y}{arg\,min}\left(-log\ \prod_{i=1}^{n} \frac{1}{\sigma\sqrt{2\pi}} exp\left(-\frac{1}{2\sigma^2}(m_i - C(y_i))\right)\right). \tag{2.8}$$

Other types of distribution such as Rician probability distribution is also used to model the likelihood term L in compensated medical imaging [143, 120, 9] and for the aim of image denoising.

One main issue with the ML based compensated medical imaging is that the noise gets amplified using the ML based image compensation [153, 145]. A constrained version of ML based compensated imaging is suggested to help with this issue and with the use of different constraints for different compensated imaging applications [71, 70, 74, 48]. For example, ML based compensated imaging using a simple positivity constraint [175, 153] is suggested,

$$\hat{Y}_{ML} = arg\min_{Y} \left(-log(P(M|Y))\right) \quad subject\ to \quad y_i \geq 0 \quad \forall i, \tag{2.9}$$

and with the use of an iterative method [153] to find the final solution $\hat{Y}_{ML}$.

Depending on the properties of the chosen likelihood function, L, for the ML based compensated imaging framework, a suitable optimization algorithm needs to be used for obtaining the best estimate of the final solution [86]. Non-linear conjugate gradients and limited-memory variable metric methods has been introduced as suitable optimization techniques for solving the inverse problem of Eq. (2.2) using the ML based approach [88, 153].

- **Maximum a Posteriori Estimation**: In the Maximum a Posteriori (MAP) based compensated medical imaging context, the goal is to maximize the probability distribution of the solution (here, compensated true image Y) given the measurement M according to,

$$\hat{Y}_{MAP} = \underset{Y \in \Omega}{arg\,min}\ J_{MAP}(Y) = arg\min_{Y} \left(-logP(Y|M)\right). \tag{2.10}$$

Using the Bayes Rule, there is a relation between the probability of the solution given measurements, $P(Y|M)$ that should be maximized in the MAP framework, and the likelihood term, $P(M|Y)$, in the ML approach,

$$P(Y|M) = \frac{P(Y)P(M|Y)}{P(M)}, \tag{2.11}$$

such that, the solution of MAP based compensated imaging is a modified version of the ML solution. In the relation of Eq. (2.11), the probability of measurements, $P(M)$ can be neglected since it does'nt depend on the solution Y. Therefore, the MAP formulation of Eq. (2.10) can be rewritten as,

$$\hat{Y}_{MAP} = \underset{Y \in \Omega}{arg\,min}\ J_{MAP}(Y) = arg\min_{Y} \left(-log\left(P(M|Y)P(Y)\right)\right), \tag{2.12}$$

where, $P(Y)$ defines some prior terms over the solution Y which act similar to a regularization term which is applied to the solution of ML approach. A wide variety

of prior terms such as gradient based priors [151, 146] as well as filter bank based priors [60, 130, 164] have been proposed for the aim of generating a compensated image with higher image quality [82]. Here, the likelihood term basically enforces the data fidelity over the final solution of the MAP problem. Tunning between the data fidelity term and the amount of prior enforcement is required for obtaining the most optimal solution for the compensated image.

2.3 Blind Compensated Imaging

An important class of compensated medical imaging methods mainly aim to compensate for the image degradations due to the effect of imaging system. In various types of medical imaging techniques, the effect of system related degradations can appear as blurring/aberrations such that reduces the overall quality of acquired image and make difficulties for the easy visualization of the different features and details of the imaged tissue/organ [43, 27, 180, 124, 49, 111]. In general, the effect of system related image degradations on the acquired image can be modeled through a forward problem,

$$M = D_{sys}(Y), \tag{2.13}$$

where, D_{sys} basically models the system characteristic function named as point spread function (PSF). According to this model, compensated medical imaging can be performed through an inverse problem which aims to compensate for the image degradations due to the effect of system characteristic function (PSF).

Variant types of computational methods are proposed to obtain a true estimate of compensated image by removing the effect of system related image degradations when they are mainly classified as non-blind and blind techniques [56, 43, 139]. The non-blind compensated imaging methods need to have a pre-knowledge about the system PSF function to obtain the best estimate of compensated image. According to the literature, the most common prior assumptions for the PSF function are the positiveness constraint [8], PSF function with known distributions, smoothness and symmetry constraints as well as PSF function with finite support [4, 106, 20, 115, 129]. However, the correct characterization and modeling of the imaging system PSF function is a complicated task which needs a good knowledge about the physical design and properties of the imaging system.

Blind compensated imaging techniques are able to calculate a compensated image with no prior knowledge about the imaging system. Within a blind compensated imaging framework, both of the PSF function and the true compensated image are estimated through

solving an optimization problem when the estimation procedure can be performed independently or as a joint optimization problem [43].

One general approach for performing of blind compensated imaging is through a Bayesian framework,

$$J_{BD}(Y) = P(Y, D_{sys}|M) = \frac{P(M|Y, D_{sys})P(Y)P(D_{sys})}{P(M)}, \tag{2.14}$$

where, the aim is to find the best estimate of both PSF function D_{sys} and true compensated image Y using the available degraded measurement M. In formulation of Eq. (2.14), $P(M|Y, D_{sys})$ is the likelihood term and $P(Y)$, $P(D_{sys})$ respectively represent the predefined priors over the true compensated image Y as well as the PSF function D_{sys}. Since $P(M)$ is a constant term, it can be ignored in solving of the optimization problem. Here, a conventional assumption is to assume parametrized prior distributions for the PSF function D_{sys} as well as compensated image Y when the Bayesian formulation can be written as,

$$P(Y, D_{sys}, \varrho\ |M) = \frac{P(M|Y, D_{sys}, \varrho)P(Y|\varrho)P(D_{sys}|\varrho)P(\varrho)}{P(M)}, \tag{2.15}$$

where, ϱ is known as hyperparameter that is modeled using the prior term $P(\varrho)$. In many of proposed blind compensated imaging techniques, the hyperparameters ϱ are calculated through a hierarchical Bayes modeling [99, 38, 180, 109] which includes of two steps. The aim of the first step is to model the prior terms $P(Y|\varrho)$ and $P(D_{sys}|\varrho)$ which are dependent to the hyperparameter ϱ and the second step efforts to define the prior term $P(\varrho)$ for the hyperparameters.

The true compensated image Y can be estimated by minimizing negative log of posterior probability in Eq. (2.15),

$$\hat{Y}_{BD} = arg\ \min_{Y} \left(-log \left(\int_{D_{sys},\varrho} P(Y, D_{sys}, \varrho\ |M) dD_{sys} d\varrho \right) \right) \tag{2.16}$$

which is marginalized over the hidden variables D_{sys} and ϱ. Alternatively, the inference problem can be performed through an evidence analysis [98] which has two steps, when the first step jointly obtains the best estimate of the PSF function D_{sys} and the hyperparameter ϱ,

$$\hat{D_{sys}}, \hat{\varrho} = arg\ \min_{D_{sys},\varrho} \left(-log \left(\int_{Y} P(Y, D_{sys}, \varrho\ |M) dY \right) \right) \tag{2.17}$$

and the second step aims to find the best estimate of compensated image $\hat{Y}_{BD}$ using the estimated PSF function $\hat{D_{sys}}$ and the hyperparameter $\hat{\varrho}$ from the first step,

$$\hat{Y}_{BD} = arg\ \min_{Y} \left(-log \left(P(Y|\hat{\varrho}) P(M|Y, \hat{D_{sys}}, \hat{\varrho}) \right) \right). \tag{2.18}$$

2.4 Super Resolution Compensated Imaging

Super resolution compensated imaging is a recognized computational technique that takes advantage of multiple degraded acquisitions of a scene (a tissue/organ in medical imaging) to generate a compensated image with more resolution and higher overall quality. In the field of medical imaging, super resolution techniques are shown as a useful computational approach that can overcome the resolution limitation of the imaging system when it provides cheaper solution compared to the similar hardware techniques [62, 156, 127, 41].

Given a set of W degraded measurements M_k, the general framework of super resolution compensated imaging can be modeled as a forward problem,

$$M_k = D_{sup}(Y) + \aleph, \quad k = 1, ..., W \tag{2.19}$$

where, D_{sup} is the degradation function and $\aleph$ denotes to the noise of k^{th} measurement. In all super resolution imaging techniques, the degradation function D_{sup} basically models a number of acquisition/reconstruction degradations including (1) the effect of PSF function, (2) data decimation as well as (3) motion artifact. To be able to generate a compensated image using any super resolution compensated imaging method, there should be a subtle difference between the sequence of degraded data measurements. In most medical imaging techniques, this condition can be easily satisfied since there is often a subtle difference between the multiple acquisitions either due to the movement of the tissue/organ (for example in imaging of moving organs such as eye or heart) or due to motion caused by imaging system itself (for example the jitter in time domain optical coherence tomography imaging system).

To obtain a compensated image, Y, using super resolution technique, an inverse problem of,

$$Y = D_{sup}^{-1}(M_k), \quad k = 1, ..., W \tag{2.20}$$

should be solved.

A large number of techniques are proposed to solve the super resolution inverse problem of Eq. (2.20) when the most popular methods can be categorized as: interpolation based

approaches [119, 110], regularization based methods [10, 103, 5], frequency based techniques [170, 163], sparsity based methods [172, 165, 52], wavelet based approaches [53, 92] and learning based methods [12].

A general Bayesian approach for solving of SR inverse problem in Eq. 2.20 can be formulated as,

$$\hat{Y}_{sup} = \underset{Y \in \Omega}{arg\,min}\ J_{SR}(Y) = \underset{Y \in \Omega}{arg\,min}\,(-log(P(Y|M_1, M_2, ..., M_W))). \tag{2.21}$$

A summary of the main framework of all discussed methods for solving of compensated imaging inverse problem along with their main features is provided in Table 2.1.

Table 2.1: Summary of methods for solving of compensated imaging inverse problem.

Regularization Method		**Features**
$\hat{Y} = \underset{Y \in \Omega}{arg\,min}\ J(Y),$ $J(Y) = \digamma(Y) + \varsigma R(Y)$	$R(Y) = \|Y\|_1$	More sparsity and sharp solution.
	$R(Y) = \|\nabla Y\|_1$	Preserving image discontinuities.
	$R(Y) = \sum_{c \in C} V_c(Y)$	Models data interactions, preserve structural information.
Bayesian Method		
ML Estimation	$\hat{Y}_{ML} = \underset{Y \in \Omega}{arg\,min}\ J(Y),$ $J_{ML}(Y) = -log(P(M\|Y))$	Amplifies noise.
MAP Estimation	$\hat{Y}_{MAP} = \underset{Y \in \Omega}{arg\,min}\ J(Y),$ $J_{MAP}(Y) = -log(P(M\|Y)P(Y))$	A regularized version of ML with less noise.
Blind Compensated Imaging (BCI)		
Bayesian based optimization for BCI	$\hat{Y}_{BD} = \underset{Y \in \Omega}{arg\,min}\ J(Y),$ $J_{BD}(Y) = -log\left(P(Y, D_{sys}\|M)\right)$	Jointly estimate the system PSF and compensated image.
Super Resolution (SR) Compensated Imaging		
Bayesian based optimization for SR imaging	$\hat{Y}_{sup} = \underset{Y \in \Omega}{arg\,min}\ J(Y),$ $J_{SR}(Y) = -log(P(Y\|M_1, M_2, ..., M_W))$	Use multiple measurements to perform compensated imaging.

2.5 Random Field Modeling for Compensated Imaging

Any type of medical image contains some sort of contextual information that can be modeled using the interactions that exist among the image pixels. The contextual information basically include different details, features and structures of the imaged tissue/organ that expected to be properly preserved in the acquired medical image. Capturing of a medical image with exactly preserving all the contextual information of the imaged tissue/organ is only possible if both imaging system and imaging procedure be ideal.

Inferring of different types of contextual information provides a source of valuable knowledge about the image such that it is useful for the better image interpretation. In addition, the image contextual knowledge can be also incorporated to many different low level and high level image processing tasks including compensated medical imaging techniques and for the aim of improving the performance of the utilized computational technique.

Random field modeling is a powerful form of image representation that provides the opportunity of modeling different image contexts through a graphical representation framework. Assuming a set of finite measurements as a random field S, defined in the context of graphical model, all the possible interactions among the data measurement, their dependencies to the corresponding labels as well as all the interactions among labels can be modeled thorough defining of proper connections between the graphical model nodes.

Different types of random field models are introduced in the literature with the most popular one known as Gibbs random field (GRF), Gaussian random field (GRF), Markov random field (MRF) [57] as well as conditional random field (CRF) [73]. MRF and CRF modeling has found a big popularity in the field of medical image processing such that they have been incorporated to a variety of image processing algorithms [152, 26, 138, 13, 58]. A brief explanation about the MRF and CRF modeling is provided here.

2.5.1 Conditional Random Field Models

CRF is a well-established form of undirected graphical model which is suitable for encoding of all dependencies that exist among the data observations, the interactions between the inferred labels as well as the relationships between the observations and corresponding labels [73]. Such a structural encoding of the observations provides a useful form of data representation that can be easily incorporated to the various computational imaging methods and algorithms.

CRF model is the discriminative variant of generative MRF model [131] which has a simpler structure as well as less limitations for modeling of the complex data interactions. While Generative models such as MRF attempts to model the joint probability distribution over the inferences (labels) and observations, the goal of discriminative models is to find a conditional probability distribution of inferences given the observations. The general framework of an inference problem using both MRF and CRF models is explained in follows.

2.5.2 Inference in MRF and CRF Modeling

Given a set of observation data, the goal of any inference step in both MRF and CRF modeling is to predict the best estimate of the outcome solution (labels) for the problem. The inference step using both MRF and CRF modeling are formulated here.

- **MRF Model**: Suppose $M = \{m_i\}_{i \in S}$ represents a set of observations in random field space S (Ex: data acquisition in medical imaging), then, using a Bayesian framework, generative MRF models try to find a joint probability distribution $P(M, Y)$ for the set of observations $M = \{m_i\}_{i \in S}$ and corresponding inferences $Y = \{y_i\}_{i \in S}$ in the form of,

$$P(M, Y) \propto P(Y|M) = \frac{P(M|Y)P(Y)}{P(M)}, \tag{2.22}$$

  where, $P(M|Y)$ is the likelihood term and $P(Y)$ represents some predefined prior over the inferences of the problem. Since the probability of the observations, $P(M)$, does'nt change with respect to any solution Y, it can be simply considered as a normalization constant and be removed from the formulation in Eq. (2.22). Also, to simplify the calculation, in most cases, it is assumed that the conditional independence condition satisfies, means each sample of observations M is independent on the other observations samples with respect to the inferences Y and therefore the likelihood term can be factorized as,

$$P(M|Y) = \prod_{i \in S} P(m_i|y_i) \tag{2.23}$$

  where, i denotes to each location of the assumed random field domain S. Here, m_i and y_i correspondingly denote the observation (data acquisition) and related inference at i^{th} site in S.

  In the MRF and CRF literatures, the most common used model for the likelihood term, $P(m_i|y_i)$, is the Gaussian distribution function when the predefined prior over

the interferences, $P(Y)$, is often modeled as a Gibbs distribution of the following form [131],

$$P(Y) = \frac{1}{Z} e^{-E(Y)} = \frac{1}{Z} e^{-\sum_{c \in C} V_c(Y)}, \tag{2.24}$$

in which, C represents a set of cliques (mutually neighboring sites) over the assumed observation graph and $E(.)$ represents the total energy of the inference Y over the clique structures C. Here the energy function $E(.)$ is composed of a set of clique potentials V_c. Based on the different features and characteristics of the in-hand problem, various forms of clique potential function V_c can be used. In the formulation of Eq. (2.24), Z is a normalization term, called as partition function.

For some applications working in the logarithmic domain can simplify the MRF inference. In such a condition, the posterior probability distribution of MRF modeling can be written as,

$$P(Y|M) = \frac{1}{Z} exp \left[\sum_{i \in S} log(P(m_i|y_i)) + \sum_{c \in C} V_c(Y) \right]. \tag{2.25}$$

One restriction issue with using the MRF model arise from the independence condition assumption of Eq. (2.23). Since the conditional independence between the observation/inference samples does'nt satisfy in all sort of problems, the factorized form of Eq.(2.23) is not always applicable. The lack of this assumption leads to the intractable inference problem for MRF model. In such a situation, using CRF model helps to overcome the computational tractability as CRF model does'nt need to model the joint probability distribution $P(M, Y)$. The use of CRF model is also preferred when the dimensionality of the observations is large and for the cases that observations have many unknown dependencies.

- **CRF Model**

  The goal of CRF modeling is to directly find the posterior probability distribution of inferences over the observations, $P(Y|X)$, and without the need to model the joint probability distribution $P(M, Y)$. To be able to use the CRF modeling, the positivity assumption of: $P(Y|X) > 0$ as well as the Markovian condition,

  $$P(y_i|M, y_j, j \neq i) = P(y_i|M, y_j, j \in N_i). \tag{2.26}$$

  should be satisfied [78]. In this relation, y_j, denotes to the set of inferences at all sites of the observation graph except the location, i, and N_i represents a neighborhood for each location, i, in the assumed observation graph. Markovianity basically shows the

existent connections between each inference y_i and the whole set of observations M as well as its dependency to the inferences about other observations that are located in the neighborhood of each location, i, in the observation graph. In other words, a CRF model is globally conditioned on the whole observations, M, and locally conditioned on the observation inferences for a specified neighborhood.

According to the Hammersley-Clifford theorem and with the assumption of only up to the pairwise clique potentials be nonzero [24], the posterior probability distribution $P(Y|M)$ in a CRF model can be represented as,

$$\begin{aligned} P(Y|M,\Theta) &= \tfrac{1}{Z(M)} exp(-E(Y|M)) \\ E(Y|M) &= \tfrac{1}{Z(M)}(\textstyle\sum_{i\in S} \Psi_u(y_i, M, w^u) + \sum_{i\in S}\sum_{j\in N_i} \Psi_p(y_i, y_j, M, w^p)), \end{aligned} \tag{2.27}$$

where, $Z(.)$, denotes the partition function which is a normalizing constant, and $E(.)$ is an energy function defined over the observations random field, S, which includes the unary (association) potential function, $\Psi_u(.)$, and the pairwise potential function, $\Psi_p(.)$. Here, $\Theta = \{w^u, w^p\}$ denotes to a set of model parameters that control the effect of unary and pairwise potential functions on the final solution and N_i represents a specified neighborhood for each location i in the observation graph. In the CRF model of Eq. (2.27), the pairwise potential function, Ψ_p, is equivalent to the potential term, V_c, in the MRF model of Eq. (2.25).

- **MRF Model Versus CRF model**

  According to the Bayes rule in Eq. (2.22), there is a relation between the formulation of CRF and MRF modeling such that each framework can be converted to other by some manipulation. However, the discriminative characteristic of the CRF model makes it a more suitable approach for the aim of different data discrimination tasks such as data segmentation [76, 58, 13], data labeling for the goal of classification [32, 166] as well as object detection [117, 112] when the inference step is more tractable compared to the MRF modeling.

  Comparing of MRF and CRF models as formulated in Eq.(2.25) and Eq.(2.27) shows two main differences that exist for the inference using MRF and CRF modeling:

  1. First, in CRF modeling, the unary potential function, $\Psi_u(.)$, at each location, i, is a function of all other observations, M, and the corresponding inference, y_i, at that specific site. However, in MRF modeling and with the assumption of conditional independence for the observations/inferences, the unary potential function is only dependent on the observation, m_i, and the corresponding inference, y_i, at the same location, i, in the observation graph.

2. Second, in MRF modeling, the pairwise potential function for each pair sites i and j is independent of the observation M, and is only dependent to the inferences y_i and y_j at those sites. However, in CRF framework, it is also a function of all observations, M.

- **CRF Potential Functions**

  The whole art of CRF modeling is in designing suitable unary and pairwise potential functions. In CRF modeling, the goal of unary potential function is to enforce the data fidelity to the final estimate of the problem solution, means constraint the final solution to obey the data observation model. The pairwise potential function is incorporated to enforce some of the inherent characteristics, properties and features of the desired solution to the optimization problem. Choosing proper potential functions for both unary and pairwise terms is of great importance such that directly affects on the final solution of the CRF inference.

  In the literature and with regard to the different applications, various types of functions are suggested for modeling of pairwise potential function in a CRF framework [61, 179, 23, 7, 75] such as the smoothness pairwise potential function [11] and edge preserving pairwise potential[26].

- **CRF Training**

  In CRF modeling, the set of model parameters, $\Theta = \{w^u, w^p\}$, basically controls the effect of unary and potential functions in calculation of the final solution. The training step aims to learn all the parameter of CRF model such that it results to the best fitting between the posterior probability distribution, $P(Y|M)$, and the observed training data. Intuitively, this means that by feeding of the CRF model with all training observations, the CRF model should be trained well such that be able to find a true inference, Y, about a new data observation M^{new}.

  Different methods are proposed for the aim of parameter learning in CRF modeling. The most typical way of CRF training is to find a set of parameters, Θ, such that it maximizes the log-likelihood function of the posterior probability function, $P(Y|M)$ [73]. This is subject to enforce a prior, $P(\Theta)$, over the parameter set, Θ (To avoid the over-fitting problem), yielding an objective function of the form,

$$L(\Theta) = \sum_i log_\Theta P(y^i|m^i) + logP(\Theta). \tag{2.28}$$

  Some of the other most popular methods that are proposed for the aim of CRF training are including the gradient descent method, sum-product belief propagation,

loopy belief propagation as well as mean field method [73]. Some approximation methods such as the pseudo-likelihood are also proposed for learning of parameters in CRF modeling when CRF has a complex structure [147]. These approximation methods are usually more simpler compare to the exact sampling methods when they provide a good consistency with the parameters estimates.

After training of CRF model parameters, Θ, the inference over any new data observation M^{new} can be performed as,

$$Y^* = argmax_Y P(Y|M^{new}, \Theta). \tag{2.29}$$

Different methods are proposed for solving of the inference optimization problem of Eq. (2.29) when the best choice of the algorithm is often chosen based on the structure of CRF model and the complexity of its potential functions [147, 73].

2.6 Fully Connected Conditional Random Field Model

One main limitation with the standard CRF modeling is that, the standard CRF models only account for the sparse, local interactions that exist among the data inferences while they ignore the incorporation of long-range inference interactions in to the CRF model [19]. This limitation comes form the specific design of the pairwise potential function as it only accounts for the inference interactions in a specified spatial neighborhood of typically 4-8 pixels.

For many of the CRF applications, using of the standard CRF modeling that only accounts for the short-range pixel-wise connections is more preferable since it leads to the more tractable inference problem with less amount of computation. However, ignoring of long-range interactions in the design of CRF framework may lead to the over-smoothness of the inference solution and also cause some inconsistency [64, 63, 178]. In addition, only accounting for the short-term local interactions in the designing of CRF modeling may lead to the loss of some useful global contextual information that are useful for obtaining a more true estimate of the final solution. Leveraging of the global contextual information to the CRF model needs to be considered by accounting for the long-range interactions in the design of CRF framework [19].

Incorporation of the long-range observation/inference interactions in to the random field modeling has been accounted using the different approaches. Hierarchical conditional random fields (HCRF) are proposed to feed the CRF models with the contextual information of different scales. A typical form of an energy function for the HCRF model can be

formulated as in [72, 182, 162],

$$E(Y|M,\Theta_h) = \sum_{i\in S}\Psi_u(y_i, M, w^u) + \sum_{i\in S, j\in N_i}\Psi_p(y_i, y_j, M, w^p) + \sum_{i\in S, k\in C}\Psi_h(y_i, y_k, M, w^h) \tag{2.30}$$

where, $\Psi_u(.)$ and $\Psi_p(.)$ respectively denote to the unary and pairwise terms that is typical in CRF modeling and $\Psi_h(.)$ represents a higher order potential function which models the long-range interactions. In this formulation C is a clique structure with arbitrary size defined over random space S such that it accounts for the long-range interactions. Here, $\Theta_h = \{w^u, w^p, w^h\}$, represent a set of model parameters that control the effect of unary, pairwise and higher order potential functions on the inference solution.

CRF models with higher order potentials are proposed for performing of different image processing and computer vision tasks which need to account for the higher order observation/inference dependencies in to the inference framework [133, 114, 91].

Fully Connected CRF models (FC-CRF) are introduced as an extension of standard CRF modeling which assume a connection between each node in the observation graph to the all other graph nodes. Using of the FC-CRF framework allows for modeling of all possible long-range interactions that potentially exist among the observations/inferences and therefore improve the accuracy of the inference step. A general form of energy function for the FC-CRF model can be formulated as,

$$E(Y|M,\Theta) = \sum_{i\in S}\Psi_u(y_i, M, w^u) + \sum_{i\in S, j\in C}\Psi_p(y_i, y_j, M, w^p) \tag{2.31}$$

in which, $\Psi_u(.)$ is the unary term and $\Psi_p(.)$ is an extension of the pairwise term in standard CRF modeling such that models the connection of each site i in the observation graph model to the all other sites $j \in C$ when C defines a clique structure over the random field space S. Ideally, to account for the full connectivity concept in FC-CRF modeling, the clique structure C should encompass the whole random field space of observations. However, accounting for such a large click structure makes the inference problem highly computational and mainly intractable, particularly when the problem size scales up. This computational issue leads to a big challenge in using of FC-CRF modeling. The conventional methods such as belief propagation, graph-cut based methods and mean field approximation are not able to truly solve the inference problem of FC-CRF model for the large-scale data [126, 178]. Hence, the most recently related research of the field are concentrated on finding more tractable computational inference algorithms that are capable of handling the large-scale inference problem in using of FC-CRF model framework.

Different techniques are proposed to reduce the computational burden of the inference problem in FC-CRF model. A filtering based approach using the the mean field approximation for the CRF is proposed in [63] when a combination of Gaussian kernels are used to model the pairwise potential term in the FC-CRF model. An extended version of this filter based inference approach is proposed in [159] which takes advantage of more general Gaussian kernel and in [160] which allows for the incorporation of higher order potential terms to the framework of FC-CRF modeling. An efficient inference approach for the FC-CRF problem is also proposed in [178] by enforcing a stationary constraint on the pairwise edge potential function with arbitrary distribution which is less limiting compared to the work of [63] which models the pairwise term using Gaussian distribution. One method is proposed for the simplification of FC-CRF inference step through modeling of the pairwise term as non-parametric distribution, designed based on a dissimilarity measure. In such a proposed inference framework, the pairwise distribution needs to be learned with taking advantage of the available training observations. This inference method can be used with more general FC-CRF frameworks as it is not limited to the selection of a specific distribution for the pairwise term but with the similar efficiency to the method of [63]. A similar technique to the work in [63] is also proposed to solve the inference problem of FC-CRF model in problems with continuous solution, for example in solving of a regression problem [126]. Despite the great efficiency of all these approaches in terms of reducing the complexity of the FC-CRF inference problem, all these techniques are still limited to the use of specific types of potential functions which basically treat the inference problem as a filtering task. Developing of more general inference methods with the ability of incorporating arbitrary potential functions is still under investigation and needs more research.

Training of FC-CRF model parameters has been performed using various methods such as piecewise training algorithm [63, 159] and learning using a structured support vector machine [107].

A graphical representation for all MRF, CRF and FC-CRF models are provided in Fig. 2.2(a-c) when it shows the differences between these random field models.

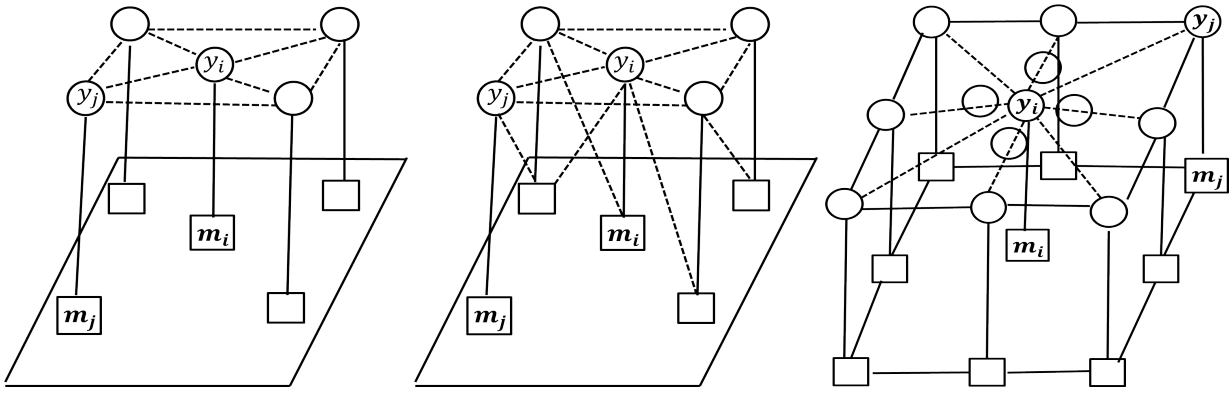

(a) MRF (b) CRF (c) F-CRF

Figure 2.2: Graphical representation of (a) MRF model, (b) CRF model and (c) FC-CRF model.

Chapter 3

Unified Probabilistic Framework for Cross-Domain Compensated Medical Imaging

3.1 Introduction

Designing of a unified probabilistic computational framework for cross-domain compensated medical imaging is the main contribution of this thesis. The goal of using such a framework is to generate a compensated image of higher quality with simultaneously accounting for the different degradations that happen in both acquisition and reconstruction domains and commonly exist in various types of medical imaging. Such a computational compensation framework can provide a more optimized, cheaper as well as easier solution for performing of compensated medical imaging when it compares to the similar hardware approaches. Jointly compensating for the different image degradations in acquisition and reconstruction domains is not possible through any of the hardware approaches since each single type of image degradation needs to be compensated using a separate hardware competent which is specifically designed for that aim.

This chapter describes in detail the general formulation and design of the proposed unified probabilistic computational framework for cross-domain compensated medical imaging. A general diagram of the proposed computational cross-domain compensated medical imaging framework is shown in Fig. 3.1. The main component of the designed framework is the computational compensated imaging block which is generally fed by measurement in acquisition domain, characterization of the degradation in acquisition domain as well as

characterization of the degradation in reconstruction domain. The output of the designed computational cross-domain compensated medical imaging framework is an estimation of the desired compensated medical image.

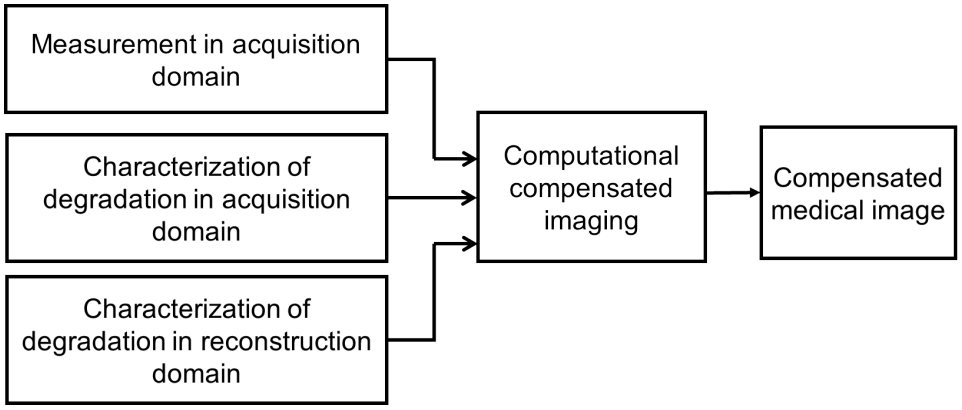

Figure 3.1: A general diagram for the proposed computational cross-domain compensated medical imaging framework.

The novel contributions of the proposed cross-domain compensated medical imaging framework are elaborated here.

1. The proposed compensated imaging approach provides a general computational framework for performing of compensated medical imaging that can be used for the quality enhancement of different types of medical imaging techniques. The proposed compensated imaging framework can be easily modified to account for the different types of degradations in both acquisition and reconstruction domains which typically arise in working with various medical imaging techniques. The general formulation of the proposed cross-domain compensated medical imaging framework is presented in Section 3.3.

2. A novel feature of the proposed computational cross-domain compensated medical imaging approach is to incorporate a newly designed random field model named as stochastically fully connected conditional random field (SFC-CRF) in to the modeling of cross-domain compensated medical imaging framework. The incorporation of SFC-CRF model to the framework of proposed cross-domain compensated medical imaging opens up the possibility of incorporating different types of available structural information about the tissue/organ to the designed compensated imaging framework such that can help in better calculation of the true compensated image.

The general concept and formulation of the utilized SFC-CRF model is explained in Section 3.2 when it is compared to the typical FC-CRF model.

3. One of the main feature of the designed compensated imaging framework is that it provides a cross-domain platform for performing of compensated medical imaging. It means that, the proposed computational compensated imaging framework provides the possibility of incorporating the image degradations from the different domain spaces in a unified compensation model framework (for example accounting for the aberrations in k-space and noise in spatial domain). This is an advantageous feature for performing of computational compensated imaging because many sort of image degradations can be better compensated in one domain as opposed to the other domain. When there is a mixture of image degradations from different domains, such a proposed cross-domain compensated medical imaging framework that is able to jointly handle these image degradations is preferred since it can optimize the performance of compensated imaging.

4. The proposed cross-domain compensated medical imaging model can be extended to a super resolution compensated imaging framework which produces a compensated medical image with taking advantage of multiple data measurements. The general formulation of the developed super resolution compensated imaging framework is presented in Section 3.4. A summary of this chapter is provided in Section 3.5.

3.2 Stochastically Fully Connected Conditional Random Field Model

Stochastically fully connected conditional random field (SFC-CRF) refers to a specific type of fully connected conditional random field in which the data observation interactions are modeled using a stochastic process. Similar to the FC-CRF model that is explained in Section 2.6, in SFC-CRF modeling, the main assumption is that each data observation has a relationship to the all other data observations but through a stochastic clique structures with specific probability distribution. The advantage of incorporating such a stochastic architecture to the SFC-CRF modeling is in reducing the overall number of pairwise cliques such that it helps in having a more tractable FC-CRF model with less required computation time.

Similar to the formulation of FC-CRF model, a general form of an energy function for

a SFC-CRF model can be formulated as,

$$E(Y|M) = \sum_{i \in S} \Psi_u(y_i, M) + \sum_{\varphi \in C} \Psi_p(y_\varphi, M). \tag{3.1}$$

In this formulation, $M = \{m_i\}_{i \in S}$ denotes to the data observations within an assumed random field S and $Y = \{y_i\}_{i \in S}$ represents a set of observations states at all locations i in the defined random space S. Here, $y_\varphi \in Y$ denotes to a subset of inferences (states) for observations in a clique structure defined by C. Similar to the conventional CRF modeling, $\Psi_u(.)$ and $\Psi_p(.)$, are correspondingly denote to the unary and pairwise potential functions with the following expressions,

$$\begin{aligned} \Psi_u(y_i, M) &= \sum_{k=1}^{K} w_k^u f_k^u(y_i, M), \\ \Psi_p(y_\varphi, M) &= \sum_{\{y_i, y_j\} \epsilon y_\varphi, k=1}^{K'} w_k^p f_k^p(y_i, y_j, M), \end{aligned} \tag{3.2}$$

where defines the unary and pairwise potentials as a combination of specific designed feature functions $f^u(.)$ and $f^p(.)$. In this formulation, the parameters w^u and w^p respectively control the effect of unary and pairwise potential feature functions in the training step of SFC-CRF modeling.

The art of SFC-CRF model is in taking advantage of a stochastic design for the clique structure C [137]. Different types of clique structure can be incorporated to the SFC-CRF modeling when one simple approach is to design a pairwise clique structure, in which, C represents a set that contains the clique structures for all pixels,

$$\begin{aligned} C &= \{c_p(i)\}_{i \in S}, \\ c_p(i) &= \{(i, j) | j \epsilon N_i, \iota_{ij} = 1\}. \end{aligned} \tag{3.3}$$

Here, $N_i = \{j | j \in S, j \neq i\}$, represents the whole neighborhood of each site (node), i, in the data observation random space. In the formulation of clique structure in Eq. 3.3, the defined clique structure for each site, i, is determined based on a specific stochastic indicator function, ι_{ij}, which determines the connectivity of each node, i, to the other nodes, j, over the whole defined neighborhood (basically, the neighborhood should contain the whole data observation random space for satisfying the full connectivity condition).

The stochastic indicator function, ι_{ij}, can be constructed using different probability functions when these probability distributions are chosen based on the specific feature/properties of the in-hand problem. One typical design for the stochastic indicator function that can be useful for compensated medical imaging is formulated as,

$$\iota_{ij} = \begin{cases} 1 \;\; P^{SP}_{i,j} P^{D}_{i,j} \geq \Upsilon \\ \\ 0 \;\; otherwise \end{cases} \tag{3.4}$$

in which the stochastic indicator function, ι_{ij}, is determined as a combination of two different probability distributions P^{SP} and P^{D} when they are characterized as follows:

- The probability function, P^{SP}, which aims to account for the spatial relation between each two nodes i and j in the designed SFC-CRF model, meaning that the pair nodes which are spatially closer have assigned a higher probability to be connected in the design of SFC-CRF model.
- The probability function, P^{D}, which aims to account for the relations of the data observations at each two pair nodes i and j using a probability function and enforce it to the SFC-CRF modeling.

In this model, Υ, refers to a threshold that controls the amount of graph sparsity by determining the amount of connections between graph nodes.

A schematic representation of a general SFC-CRF model is shown in Fig. 3.2 using a graph $G(\vartheta, \S)$. In this graphical representation, ϑ, includes all graph nodes which determines the states, $Y = \{y_i\}_{i \in S}$, in SFC-CRF model and $\S$ is the set of all graph edges that shows the connection between each two nodes y_i and y_j. Corresponding to each node, there is an observation $m_i \in M$. In SFC-CRF modeling, the graph G can be assumed as a realization of a random graph [33] and due to the point that the edges of graph are randomly drawn from a predefined distribution. Here, each node of graph is connected to the all other nodes through a specific designed stochastic indicator function, ι_{ij}, which basically defines the probability of connectedness between the nodes.

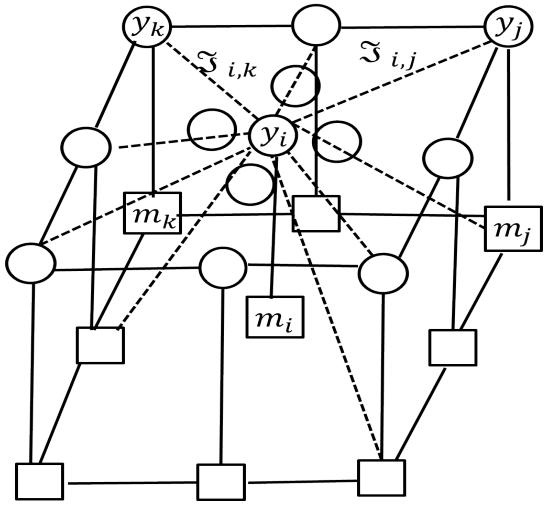

Figure 3.2: A graphical representation of a SFC-CRF model. The connectivity between each pairs of nodes is defined through a specific distribution. Each two pairs of nodes are connected based on the probability drawn form this distribution. The connection between each pairs of nodes y_i, and y_j are determined using an edge $\Im_{ij}$. Corresponding to each node, y_i, there is a observation measurement, m_i.

The main advantages of SFC-CRF model over the typical FC-CRF model are explained here.

1. The incorporation of stochastic clique structures to the modeling of FC-CRF basically leads to a sort of down-sampling of the graph node connections in FC-CRF model such that a considerable number of nodes will likely be disconnected. As a result of these node reduction, the computational complexity of the SFC-CRF model is highly reduced compared to the standard FC-CRF models.

2. Taking advantage of SFC-CRF model is more advantageous and effective compared to the standard FC-CRF model because it makes no limitation for using of approximation algorithms or utilizing of specific potential functions that is often required for handling of the inference problem in typical FC-CRF models.

These features of the SFC-CRF model makes it a better choice as well as more powerful option for being incorporated to the compensated medical imaging framework.

3.3 Unified Probabilistic Cross-Domain Compensated Medical Imaging Framework

A general mathematical framework for the proposed unified cross-domain compensated medical imaging is formulated in this subsection. As mentioned in Chapter 2, any type of compensated medical imaging can be mathematically formulated as a general inverse problem,

$$Y = D^{-1}(M, d_{Aq}, d_{Rec}), \tag{3.5}$$

where, M and Y are the data measurements (medical data acquisition) and compensated medical image. Here, $D(.)$ denotes to the overall degradation function which can model a variety of image degradations in both acquisition and reconstruction domains that commonly happens in different types of medical imaging. In the inverse model of Eq. 3.5, the degradation function D is a joint function of data measurements M, degradations in acquisition domain, d_{Aq}, as well as degradations in reconstruction domain, d_{Rec}, which all need to be fed to the framework of cross-domain compensated medical imaging to calculate a compensated medical image.

The general formulation of Eq. 3.5 can be easily modified to be fitted with different types of medical imaging techniques and to compensate for a variety of various types of image degradations such as noise, artifact, image aberration as well as dispersion.

The acquisition degradations mainly refer to the degradation issues that are caused by the effect of medical imaging system itself and during the data collection. The acquisition degradations mainly sources from some physical limitations of an imaging system such as the imperfect design of different system's components. Some specific properties and features of the tissue/structure also may intervene with the imaging acquisition procedure and therefore lead to the image degradation in the acquisition domain. In addition, image degradations in reconstruction domain can also arise due to the use of a non-optimal image reconstruction or processing methods. The existence of degradations in both acquisition and reconstruction domains negatively impact on the overall quality of medical imaging and hence correcting for that is required for the quality enhancement of all types of medical imaging.

In many of medical imaging techniques, the data acquisition and image reconstruction steps need to be performed in different domains (for example: The data acquisition M is in Fourier/k-space domain and the image reconstruction Y is in spatial domain). In such a case, the acquisition and reconstruction image degradations may also arise in different domains and therefore there is a preference for correcting of each image degradations in the original domain that it occurs.

The proposed cross-domain compensated medical imaging provides a computational framework which ables for correcting of image degradations issues from different domains using a unified compensated imaging model.

To perform compensated medical imaging and find the best estimate of a compensated medical image $\hat{Y}$, the inverse problem of Eq. 3.5 should be solved. To this aim, the proposed cross-domain compensated medical imaging is designed based on the Bayesian model and with taking advantage of a Maximum a Posterior (MAP) framework,

$$\hat{Y}_{MAP} = arg\,\max_{Y} P(Y|M). \tag{3.6}$$

which aims to find the best estimate of compensated medical image $\hat{Y}$ by maximizing the posterior term $P(Y|M)$.

To this aim, the posterior probability of compensated medical imaging in Eq. 3.6 can be reformulated as a general CRF model,

$$P(Y|M) = \frac{1}{Z(M)} exp(-E(Y,M)) \tag{3.7}$$

where, $Z(.)$ is a normalization term (called partition function) and $E(.)$ basically defines a joint energy function over the data acquisition M and compensated medical image Y.

The proposed cross-domain compensated medical imaging incorporates a new designed probabilistic model (SFC-CRF model) in to its framework which leads to a novel probabilistic framework for performing of compensated medical imaging. To this aim, the data acquisition M and compensated medical image Y are assumed to be modeled in a random field space S and with the graphical representation that is shown in Fig. 3.2. The joint energy function $E(.)$ in Eq. 3.7 is defined as,

$$E(Y,M) = \sum_{i \in S} \Psi_u(y_i, M) + \sum_{\varphi \in C} \Psi_p(y_\varphi, M). \tag{3.8}$$

where, $\Psi_u(.)$ and $\Psi_p(.)$ correspondingly model the unary and pairwise potential functions. Here, the pairwise potential function takes advantage of a set of stochastically drawn clique structures C as discussed in Section 3.2.

A general form of potential function for the unary term can be formulated as,

$$\Psi_u(y_i, M) = \digamma_u(m_i, D(y_i, d_{Aq}, d_{Rec})). \tag{3.9}$$

where, $\digamma_u$ is a function that penalizes deviation between data measurements M and compensated image Y. The designed unary potential function basically works in a way that

it enforces the final estimate of compensated medical image to be fitted to the data measurements M (satisfies the data fidelity term). To this aim, the designed unary potential function basically encodes the direct relationships between the data measurements, m_i, and compensated medical image y_i, at each location i in the graph and by accounting for degradations in both acquisition, d_{Aq}, and reconstruction, d_{Rec}, domains in modeling of the degradation function $D(.)$.

The pairwise potential function $\Psi_p(.)$ in the joint energy function of Eq. 3.8 can be formulated as,

$$\Psi_p(y_{\varphi \in C}, M) = \exp\left(\frac{\|N_i - N_j\|_q}{\sigma_p}\right)(y_i - y_j);\ C = \{i, j\}, \tag{3.10}$$

which aims to account for the interaction relationships between each pair nodes y_i and y_j regarding to the whole data measurements M inside the predefined stochastic cliques C, when the goal is to find the best estimate of compensated medical image Y. Here, N_i and N_j correspondingly denote to specified neighborhood coordinates centered around the i^{th} and j^{th} locations in the defined graphs for the data measurements M and compensated image Y. In this formulation, σ_p basically controls the amount of exponential weighting function in the designed pairwise potential term.

In other words, the pairwise potential function is mainly responsible for the incorporation of all available prior information about the imaged structure/tissue to the framework of proposed computational compensated imaging model. Here, the art of a properly designed pairwise potential function is in enforcing of the final solution of compensated medical imaging to correctly represent all features, details and structures of the imaged tissue/structure.

To obtain the best estimate of compensated medical image, the posterior probability $P(Y|M)$ should be maximized by minimizing the joint energy function $E(.)$ in Eq. 3.8. In the proposed cross-domain compensated medical imaging framework, a gradient based optimization can be used to perform the inference step,

$$Y^{t+1} = Y^t - \rho \frac{\nabla E(M, Y)}{\nabla Y}, \tag{3.11}$$

and to find the best estimate of compensated image $\hat{Y}$. Here, ρ is a parameter that controls the learning rate of the gradient based optimization.

3.4 Super Resolution Probabilistic Cross-Domain Compensated Medical Imaging Framework

The main idea behind any super resolution (SR) technique for performing of compensated medical imaging is in using of multiple data acquisitions as opposed to a single data acquisition for generating a compensated medical image with better quality. As previously explained in Section 2.4, the main condition for performing of compensated imaging using any SR techniques is that each of the acquired data measurements (here, medical images) should contain a subtle different information about the imaged tissue/structure, means that there should be at least a small information difference between the utilized multiple data measurements. With such an assumption, SR compensated imaging methods basically benefit from all the partial existent information in multiple data measurements (here, multiple medical images) to calculate a compensated image of higher quality that better shows the different details and features of the imaged tissue/structure.

Here, we design and formulate a novel probabilistic based SR imaging technique that takes advantage of the proposed unified probabilistic computational framework of Section 3.3 for performing of compensated medical imaging. Performing of SR compensated imaging can be formulated as a general inverse problem,

$$Y_{sup} = D_{sup}^{-1}(M_k), \quad k = 1, ..., W, \tag{3.12}$$

where, M_k represents a set of W multiple medical image acquisitions and $D_{sup}(.)$ refers to the overall degradation function that potentially can model different possible degradations in both acquisition and reconstruction domains.

Here, with assuming multiple data acquisitions, $M_k, k = 1, ..., W$ as well as super resolution (SR) image Y_{sup} as random fields, the proposed probabilistic based SR compensated imaging framework aims to find the best estimate of Y_{sup} thorough solving the general inverse problem of Eq. 3.12 using a MAP strategy,

$$\hat{Y}_{sup} = arg\, max_Y\, P(Y_{sup}|M_1, M_2, ..., M_W), \tag{3.13}$$

where, $P(Y_{sup}|M_1, M_2, ..., M_W)$ is the posterior conditional probability of SR image Y_{sup} given a set of degraded acquisitions, $M_k, k = 1, ..., W$. Based on CRF modeling, the the posterior conditional probability of Eq. 3.13 can be modeled as,

$$P(Y_{sup}|M_1, M_2, ..., M_W) = \frac{1}{Z(M_1, M_2, ..., M_W)} exp(-E^{sup}(Y_{sup}, M_1, M_2, ..., M_W)), \tag{3.14}$$

where, $Z(.)$ is a constant normalization term and $E^{sup}(.)$ is a joint energy function defined over the random fields for the SR image, Y_{sup}, and all measurements $M_k, k = 1, ..., W$. Here, the joint energy function $E(.)$ is composed of the unary and pairwise potential functions $\Psi_u^{sup}(.)$ and $\Psi_p^{sup}(.)$,

$$E^{sup}(Y_{sup}, M_1, M_2, ..., M_W) = \sum_{i \in S} \Psi_u^{sup}(y_i, M_1, M_2, ..., M_W) + \sum_{\varphi \in C} \Psi_p^{sup}(y_\varphi, M_1, M_2, ..., M_W), \tag{3.15}$$

where, i denotes to each location in the defined random space S and C refers to a set of stochastic clique structures defined over the random field space S.

In the formulation of Eq. 3.15, The unary potential function is formulated as,

$$\Psi_u^{sup}(y_i, M_1, ..., M_W) = \sum_{k=1}^{W} F_u(m_{i,k}, D(y_i, d_{Aq}, d_{Rec})). \tag{3.16}$$

which aims to enforce data fidelity over the final estimation of the SR image using function F_u and by encoding the relationships that exist between each single medical image measurement, $m_{i,k}$, and SR image, y_i, at each location i and with accounting for the degradation function $D(.)$.

To perform SR compensated imaging, the pairwise potential function, $\Psi_p^{sup}(.)$ in Eq. 3.15 is also formulated as,

$$\Psi_p^{sup}(y_{\varphi \in C}, M_1, ..., M_W) = \sum_{k=1}^{W} exp \frac{\|N_{i,k} - N_{j,k}\|_q}{\sigma_p} (y_i - y_j); \; C = \{i, j\}, \tag{3.17}$$

which models the pairwise interactions between each pair nodes y_i and y_j regarding to the multiple data acquisitions $M_k, k = 1, ..., W$, when the goal is to find the best estimate of SR image Y_{sup}. Here, $N_{i,k}$ and $N_{j,k}$ respectively denote to specified neighborhood coordinates centered around the i^{th} and j^{th} locations in the assumed graphs for the k^{th} medical data acquisition. In this formulation, σ_p is a control factor which sets the power of pairwise potential function $\Psi_p^{sup}(.)$ in the defined clique structures C. Taking advantage of the stochastic clique structures C in the design of pairwise potential function in Eq. 3.17 leads to a SFC-CRF-SR compensated imaging framework which can incorporate the different contextual information about the imaged tissue/structure to the SR imaging framework and therefore reconstruct a compensated image with better overall quality.

The solution of the desired SR image can be found by performing an inference step which aims to maximize the posterior conditional probability of, $P(Y_{sup}|M_1, M_2, ..., M_W)$, in Eq. 3.13. To this aim, the joint energy function $E^{sup}(.)$ in Eq. 3.15 should be minimized thorough a suitable optimization strategy.

3.5 Summary

This chapter has presented the core contribution of this dissertation by proposing a novel probabilistic compensated imaging framework for performing cross-domain compensated medical imaging. The main compartments and the overall design of the proposed compensated medical imaging framework are explained. The general formulation of the proposed compensated imaging framework is presented which takes advantage of a newly designed SFC-CRF model in its framework. The main idea behind the utilized SFC-CRF model is reviewed. The main features and ability of the proposed probabilistic based cross-domain compensated medical imaging are explained. Furthermore, the designed compensated imaging framework is extended to a SR compensated imaging platform that opens up the opportunity of using the proposed compensated imaging approach for performing SR imaging using multiple medical acquisitions.

Chapter 4

Compensated Optical Coherence Tomography Imaging

4.1 Introduction

This chapter describes the development of a compensated optical coherence tomography (C-OCT) imaging that aims to improve the quality of OCT images through a unified computational method. The C-OCT imaging is developed based on the probabilistic cross-domain compensated medical imaging framework that was described in Chapter 3. The proposed C-OCT imaging was designed to compensate for the loss of OCT image resolution and contrast caused by presence of speckle and optical aberrations in OCT images and with the use of a purely computational image compensation approach. This chapter begins with a general description about the principle operation of OCT in Section 4.2. The main factors that cause degradation in the OCT image quality such as dispersion, speckle noise and optical aberrations are explained in Section 4.3. The most current and successful methods for compensation of speckle noise and optical aberrations are reviewed in Section 4.4. The proposed C-OCT is formulated and described in detail in Section 4.5. Results from testing the performance of the proposed C-OCT imaging on OCT images acquired from a standard resolution target, microspheres of known size embedded in weekly scattering gel and a sample of biological tissue that was imaged ex-vivo are presented in Section 4.6. A summary of the chapter is provided in Section 4.7.

4.2 Optical Coherence Tomography: Principle of Operation and Image Formation

Optical coherence tomography (OCT) is a well-known non-invasive optical imaging technique which allows for acquisition of high resolution, depth-resolved cross-sectional images of the structure of the imaged object. A typical OCT system offers non-contact, volumetric imaging of opaque and highly scattering objects such as biological tissue and can provide axial and lateral resolutions in the order of a few micrometers which allows for the visualization of the cellular structure of biological tissue. For these reasons, over the past 25 years OCT has found many different applications in both industry and medicine [30].

The basic principle of OCT imaging is somewhat similar to ultrasound imaging, except that it uses light instead of sound. OCT measures the intensity and echo time delay of backscattered light from different depths within the imaged object (a single axial or depth scan is referred to as an axial scans (A-scan)) [30]. A series of consecutive A-scans located along a line can generate a 2D cross-sectional reflectivity map of the imaged object (so called B-scan).

Due to the high speed of light, the time delays between the back-scattered light from different depths of the imaged object is in the order of femto-seconds. Because the response time of photodetectors is orders of magnitudes slower, it is not possible to measure these time delays directly. To overcome this issue, OCT systems work based on the interferometric principle, which allows for measuring such short time delays by actually measuring the, much lower beat frequency of interfering the optical beam reflecting from the imaged object with a second beam reflecting from a mirror in the reference arm of the interferometer.

A typical configuration of a Time Domain OCT (TD-OCT) system based on a conventional fiber-optic Michelson interferometer is depicted in Fig. 4.1.

The light source of the OCT system generates the required light and send it through an optical coupler to the reference and sample arms. The back-scattered light from the different depths of the imaged object is combined at the fiberoptic beam splitter with the reference beam reflected from the moving mirror and then detected using an optical detector (here, a photodetector). Generally, the intensity of the OCT signal at the detection end of the interferometer is a summation of sample ($E_s(t)$) and reference ($E_r(t)$) electrical fields

$$I = |E_r|^2 + |E_s|^2 + 2E_rE_scos(2k\Delta L), \tag{4.1}$$

where, ΔL denotes the path length difference between the sample and reference arms of the interferometer.

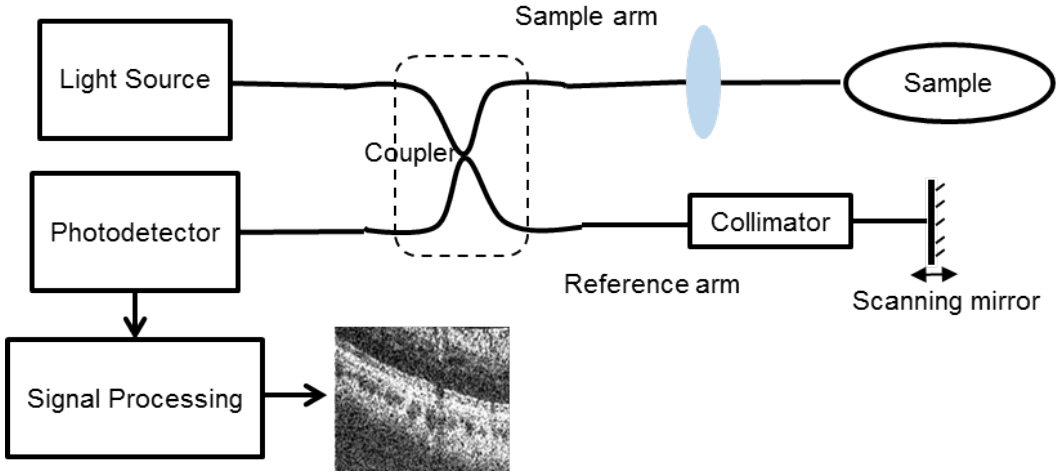

Figure 4.1: Typical configuration of a TD-OCT system.

In a typical OCT imaging procedure, several post-processing steps are required to enhance the detected OCT signal and consequently improve the quality OCT imaging. These post-processing steps mainly include the signal amplification, filtering as well as demodulation [34].

Spectral Domain Optical Coherence Tomography (SD-OCT) is an other type of OCT modality in which the the reference arm doesn't need to move and kept stationary. In SD-OCT imaging the depth information (A-scan) is obtained by applying the Fourier transform to the spectrally resolved interference fringes at the detection arm of the Michelson interferometer. SD-OCT imaging basically provides higher speed and signal to noise ratio (SNR) compare to the TD-OCT imaging.

4.2.1 Resolution in OCT Imaging Technique

Image resolution is an important characteristic of any imaging technique including OCT. Preserving the theoretical resolution for the captured OCT images is highly desired since it helps with better visualization of different features and details of the structure of the imaged object. However, in practice the overall resolution of an OCT image is always less than the theoretical axial and lateral resolutions due to a number of factors that cause degradation of the OCT resolutions, such as dispersion, optical aberrations and speckle noise. Compensating for the OCT resolution degradation is important for improving the overall quality of the OCT images.

In all OCT system configurations, the axial and lateral image resolutions are decoupled from each other. In theory in free space, the axial OCT resolution is only dependent on the central wavelength and spectral bandwidth of the utilized light source, while within the imaged object, the axial resolution at different axial locations is dependent on the absorption, scattering and dispersive properties of the material the imaged object is made of. On the other hand, the lateral resolution in OCT systems in free space theoretically is defined by the OCT imaging optics, while inside the imaged object it can be limited due to the different optical properties of the imaged object [30].

4.3 Factors that Cause Image Degradation in Optical Coherence Tomography

Similar to the all types of medical imaging systems, the overall quality of OCT imaging can be affected by different factors. Each factor negatively impacts the proper visualization of different features and details of the imaged tissue structure and also pose challenges for the correct analyzing and interpretation of the captured OCT images.

Generally, some of the image degradation in OCT images can be attributed to loss of OCT signal power due to light scattering and/or absorption within the imaged object, or improperly compensated dispersion associated with the OCT system design and/or the optical properties of the imaged object [90].

In general, the spatial resolution and contrast of OCT imaging can be affected by both the optical design of the OCT system and the optical properties of the sample. For example, the overall sensitivity (Signal-to-Noise Ratio (SNR)) of a SD-OCT system is theoretically dependent on the camera spectral response, data acquisition rate, as well as the amount of power in the reference and sample arm. However, a SNR roll-off at higher imaging depths occurs due to the limited size and number of camera pixels combined with any chromatic and spherical aberrations in the spectrometer [29].

The effective OCT axial resolution of a SD-OCT system is often lower than the theoretical axial resolution due to several factors. First, even in the case of optimally designed spectrometer, spherical and chromatic aberrations in the spectrometer optics may generate cross-talk between neighboring pixels in the camera array, especially at the second ends of the array. Such cross-talk will affect the OCT axial resolution and the effect is more pronounced for OCT signals measured far away from the zero delay point of the scanning range. Other factors that degrade the OCT axial resolution are the effect of light absorption and scattering that happens inside the imaged specimen (tissue). Both scattering

and absorption can alter the spectrum in the OCT sample arm and therefore degrade the effective axial resolution of the acquired OCT image. These spectral changes are generally depth-dependent and impossible to quantify, as they are related to the morphology and optical properties of the imaged object [34, 29].

As mentioned earlier, the theoretical lateral resolution of a SD-OCT system is primarily determined by the imaging optics and overall optical design of the OCT system. However, in practice, the lateral resolution degrades away from the focal plane due to defocus and optical aberrations issues. In addition, the depth-dependent absorption and scattering properties of the imaged object can change the spectrum and therefore the theoretical OCT lateral resolution [34, 29].

A more detailed analysis of some of the major factors that cause degradation of the OCT image resolution and SNR is presented in the following paragraphs.

4.3.1 Dispersion in OCT imaging

Dispersion is a recognized issue in all interferometry based imaging techniques such as OCT imaging. Dispersion occurs due to the non-constant group velocity of the optical pulse in an imaged specimen (tissue) such that the low frequency pulses travel faster compared to the high frequency pulses. In OCT imaging, the source of dispersion may be due to the OCT hardware components (the effect of fiber optics as well as other utilized dispersive components) or due to the specimen properties.

A dispersion mismatch between the reference and sample arms of the OCT system adds a phase term to the Fourier components of an OCT interferogram and therefore leads to the change of the OCT signal shape and consequently degrades the OCT axial resolution [3, 36]. A conventional hardware based method for the OCT dispersion compensation is to use a dispersive material such as different types of glass plates to compensate in part the lower order dispersion mismatch between the optical components of the sample and reference arms of the OCT interferometer [34]. Dynamic dispersion compensation using of this hardware approach is not possible due to the high speed of OCT image acquisition and the depth-dependent dispersive properties of the imaged object. To overcome this difficulty, various types of computational dispersion compensation methods have been proposed [90, 167, 35, 36, 79, 89].

4.3.2 Optical Aberrations

In OCT imaging, optical aberrations are a well-known issue to cause degradation of the overall quality of the OCT images, especially for out-of-focus regions. In general, optical aberrations can be defined as any deviation from the ideal optical wavefronts which typically occurs when the light is defocused. The deviation of the wavefront from the ideal shape can results in image blur that can obstruct the visualization of small details and features of the images tissue. To compensate for the OCT degradations due to the optical aberrations, the OCT optical wavefronts should be modified to approximate an ideal wavefront shape and thus minimize beam spot size at the foal plane.

Various types of optical aberrations can occur in OCT imaging including the one that caused by the optical design of the OCT imaging system and also tho one that are sourcing from the optical properties of the imaged sample [1]. The most known types of aberrations in OCT imaging are chromatic aberration, spherical aberration, coma and defocus.

Spherical aberration causes due to non-paraxial rays of light hitting the corneal surface at an non-orthogonal axis and therefore is refracted closer than paraxial rays [85]. Chromatic aberration causes by the samples which their refractive index changes with the wavelength. For example, chromatic aberration can be severe in ophthalmic OCT imaging, due to wavelength dependence of refractive index in ocular media [158]. Coma aberration arises due to the difference in distance of the incident light from the optical axis (off-axis light rays) which leads to the change of light magnification with Respect to the location [87]. Defocus aberrations can be seen for the imaging depths farther from the focal plane and due to the limitation of delivery optics in proper focusing of the light at out-of-focal plane.

Overall, all types of optical aberrations can degrade the OCT image contrast and resolution and with more pronounced effects at distances farther from the focal plane. In OCT systems which applies higher Numerical Aperture (NA) to provide better OCT lateral resolution, the effect of optical aberrations are more powerful since the depth of focus is shorter. Using of such a ultrahigh resolution OCT system for imaging of tick specimens has some limitation for the correct visualization of the details and features of the imaged specimen(tissue structures) which are at out of focus length.

Having a compensation strategy to correct for the OCT degradations due to the effect of optical aberrations is important for the quality enhancement of OCT imaging.

4.3.3 Speckle Noise

Speckle noise is a recognized factor that causes image contrast and resolution degradation in all types of coherent imaging systems including the OCT. Speckle noise is the result of multi beam inferences with random phases. The appearance of speckle noise can be observed as a grainy pattern with dark and bright spots on the acquired OCT image. The effect of speckle noise is higher for imaging of highly scattering specimens, for example in imaging of biological tissues. The presence of speckle noise can cause difficulties for the correct visualization, analysis and also interpretation of OCT images.

In OCT imaging, the OCT measurement in spatial domain are resulted from a Fourier space transformation, $M = \mathcal{F}^{-1}(M(\omega))$, where, $\mathcal{F}^{-1}$ denotes the inverse Fourier operation applied on the OCT measurement, $M(\omega)$, in k-space domain. The speckle noise in OCT imaging can be modeled as a multiplicative term $\aleph_{spk}$ [34],

$$M = Y.\aleph_{spk}, \tag{4.2}$$

which affects on the clean OCT image Y and results in noisy OCT measurement, M.

Compensating for the speckle noise in OCT imaging is an importation step of OCT quality enhancement which needs to be considered for improving the overall quality of OCT imaging.

4.4 Compensation Methods for Compensated OCT Imaging

A variety of hardware methods and software approaches have been proposed by other research groups for compensation of the different types of degradation effects in OCT images. While hardware based compensation techniques for OCT image quality enhancement do exists, they tend to be complicated, bulky, expensive and some of them time consuming. Software based compensation methods are preferred as they provide easier and inexpensive alternative for the quality enhancement of OCT images. Furthermore, correcting for multiple types factors that cause of OCT image degradation using the hardware technique is not possible since compensation of each OCT degradations needs a modification of different components in the OCT system. However, there is an opportunity for simultaneous compensation of multiple factors that cause image degradation in OCT by using a unified computational approach.

The main contribution of this Chapter is to propose a compensated OCT (C-OCT) imaging which is able to simultaneously correct for the multiple factors that cause OCT image degradation in a unified optimization framework. To this aim, our proposed C-OCT imaging is designed to jointly compensate for the effects of optical aberrations and speckle noise. However, the proposed C-OCT imaging has the potential to be expanded to account for other factors that cause OCT image degradations such as the dispersion and motion artifacts.

A short review of the existing hardware and software approaches for compensation of OCT image degradation is presented below.

4.4.1 Aberration Correction Methods

Adaptive optics (AO) has emerged as a successful hardware based approach for the aim of aberrations compensation in images acquired with a variety of optical imaging modalities including the OCT [142, 176, 94]. In general, AO technique measures the amount of optical aberrations using a wavefront sensor and takes advantage of this information to correct for the optical aberrations by using a wavefront corrector (for example, a deformable mirror). In the past, adaptive optics has been combined with OCT in a single imaging system, which led to improved in the lateral resolution, reduced the speckle size and increased the SNR in OCT images[1, 96].

I spite of the advantages offered by AO technology for OCT imaging, AO also has several major disadvantages such as complicated, bulky and expensive design. The AO technology also limits the spectral bandwidth transmitted through the AO+OCT system, which degrades the OCT systems axial resolution. In addition, using of AO based aberration compensation can limit the speed of OCT imaging which is important for the real time OCT imaging applications. These issues motivated the development of computational methods adaptive optics (CAO).

Using of CAO approach is beneficial compared to the conventional hardware based AO technology since it is inexpensive and also leads to much more compact OCT system design. Furthermore, due to the interdependence of the CAO approach from the OCT hardware, it can be used in integration with any type of OCT configuration. One main usefulness of integrating an OCT system with CAO is in providing a computational solution to overcome the depth-of-field limitation issue in OCT imaging.

Several of previously proposed CAO methods are designed as an optimization problem which takes advantage of a phase estimation to compensate for the effect of OCT optical aberrations [174, 1, 81]. A previously proposed work takes advantage of sub-aperture

based correlation along with the phase estimation to compensate for the OCT optical aberrations[65]. However, the dependency of these approaches on the phase estimation leads to the greater sensitivity of these methods to motion artifacts in the OCT image that arise from sample motion or OCT system related factors such as optical noise from the OCT light source or jitter in the OCT scanning elements (galvanometric scanners, resonant scanners, etc.) [140].

In addition, most of the existent CAO methods work based on an isotropic optical aberrations which is a correct assumption for the OCT systems with low numerical aperture. Based on this assumption, the overall OCT optical aberrations can be corrected using a spatially invariant phase correction term [65]. However, for the OCT systems with higher numerical aperture, this assumption fails and the performance of these methods is suboptimal. To solve this issue, an expanded version of sub-aperture based CAO is proposed in [66] to account for anisotropic optical aberrations in an OCT imaging with high numerical aperture [66].

As mentioned before, one source of OCT optical aberrations is due to the design of OCT system. Deconvolution based CAO approaches are proposed to correct for these system-related OCT aberrations and through integrating of the OCT system aberration function to the CAO algorithms [123, 80, 169, 49]. Utilizing these optical aberrations compensation methods need a prior knowledge about the OCT point spread function (PSF), which is the characteristic function for each OCT system.

OCT optical aberration correction using interferometric synthetic aperture microscopy (ISAM) [122, 121] was also proposed to generate OCT images with less optical aberrations and therefore preserving the same lateral resolution along whole imaging depth. ISAM takes advantage of the inverse scattering model to perform aberration correction. A combination of ISAM and CAO was also proposed for high-speed OCT imaging with sub-cellular resolution [81].

4.4.2 Speckle Noise Reduction Methods

As mentioned before, speckle is another major issue that negatively impacts on the overall quality of OCT imaging. OCT speckle removal is required for all types of OCT images when it can greatly improve the quality of OCT imaging for providing better visualization of small features and details of the images sample .

In terms of OCT speckle compensation, a variety of hardware and software based techniques were proposed. Frequency compounding and polarization diversity are the most pronounced hardware approaches that are used for the aim of OCT speckle reduction [113,

28]. Different computational techniques are also proposed for the aim of OCT speckle reduction as they mainly categorized as: speckle reduction using filtering methods [37, 108, 39], wavelet and curvelet based methods for the OCT speckle reduction [22, 54, 93], diffusion based speckle reduction techniques [134, 116], frequency domain multiplexing speckle reduction [157] as well as variational methods [40, 31].

4.5 Compensated Optical Coherence Tomography Formulation

In this section, the general formulation for a novel designed C-OCT imaging that takes advantage of the proposed probabilistic cross-domain compensated medical imaging framework of Chapter 3 is described. The proposed C-OCT imaging is specifically designed to jointly compensate for the OCT optical aberrations and speckle noise issues within a unified computational framework. A general diagram of proposed C-OCT imaging is shown in Fig 4.2.

Assuming $M = \mathcal{F}^{-1}(M(\omega))$ is a degraded OCT measurement in spatial domain, where $\mathcal{F}$ denotes the Fourier transform, and $M(\omega)$ represents the degraded OCT data acquisition in k-space domain, the formation of an OCT image can be formulated as a forward problem,

$$M = D(Y, H) \times \aleph_{spk}, \tag{4.3}$$

where, $D(.)$ models the overall OCT degradations which is a function of compensated OCT image Y (here, noise compensated, aberration corrected OCT image) and the OCT optical aberrations, H. In this formulation, $\aleph_{spk}$ refers to the multiplicative speckle noise that inherently exist in all types of OCT imaging. Since, the OCT degradation function, $D(.)$, in Eq. 4.3 is dependent on the optical aberrations H, it needs to be initially characterized for performing of C-OCT imaging. Here, as the general diagram of Fig. 4.2 display, the proposed C-OCT imaging takes advantage of a calibration procedure to obtain the optical aberrations H, and then leverages this information into the designed C-OCT imaging framework which aims to generate a compensated OCT (C-OCT) image from a degraded OCT image. To this aim and based on the related literature, the OCT optical aberrations H is initially modeled using a general Gaussian function which needs to be experimentally characterized using a proper calibration procedure and for each utilized OCT configuration.

The forward modeling of Eq. 4.3 provides a cross-domain platform for performing of C-OCT imaging which is one novel contribution of the proposed compensated imaging

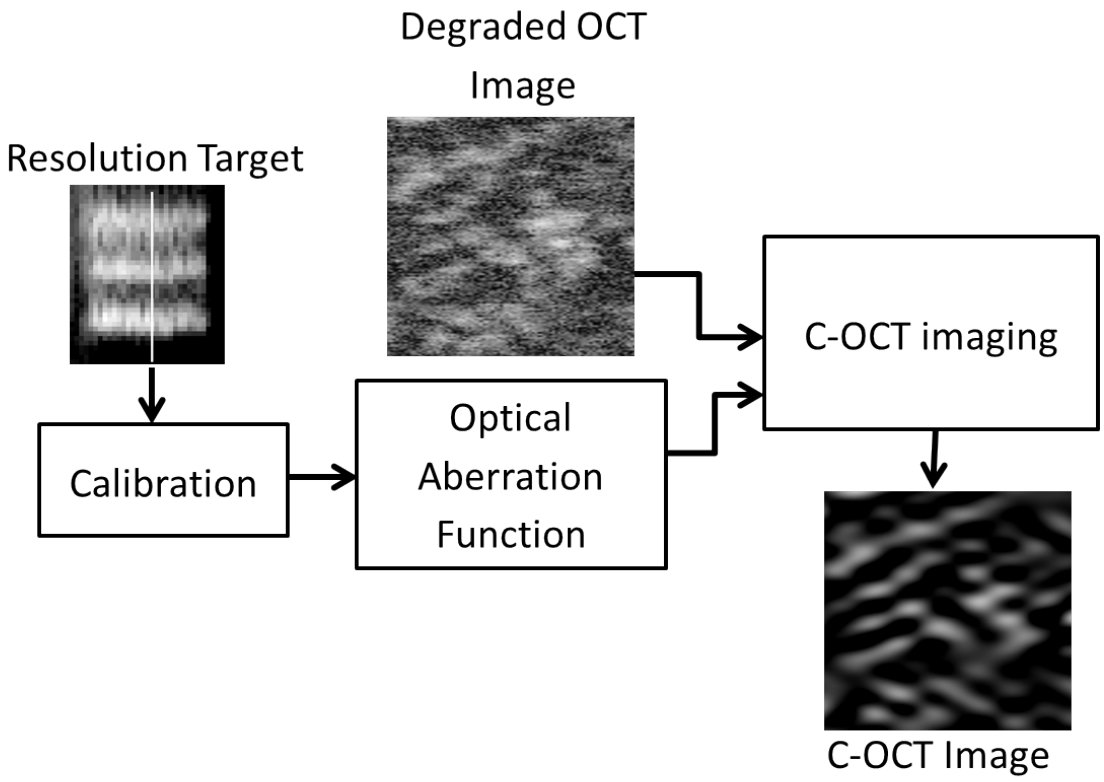

Figure 4.2: A general framework for proposed C-OCT imaging.

framework. Such a cross-domain compensated imaging framework can be used for compensation of different factors that cause OCT image degradation that occurs in different domains (for example, compensation of optical aberrations in K-space and speckle noise in spatial domain) and without the need to perform additional and time consuming domain transformation.

Based on the forward modeling of Eq. 4.3, the proposed cross-domain C-OCT imaging is modeled as an inverse problem,

$$\hat{Y} = D^{-1}(M, H). \tag{4.4}$$

which aims to find the best estimate of noise compensated, aberration corrected OCT image Y through performing of C-OCT imaging.

Similar to the proposed probabilistic cross-domain compensated medical imaging framework of Chapter 3, the designed C-OCT imaging employs a maximum a posteriori (MAP) strategy to solve the inverse problem of Eq. (4.4) and to find a true estimation of noise compensated, aberration corrected OCT image Y,

$$\hat{Y} = \underset{Y'}{argmax} P(Y|M), \tag{4.5}$$

where, $P(Y|M)$ denotes to the posterior probability for the noise compensated, aberration corrected OCT image, Y, given a degraded OCT measurement M.

The designed C-OCT imaging platform takes advantage of a new form of CRF modeling as explained in Section 3.2 of Chapter 3, named as SFC-CRF model, to perform C-OCT imaging in a random space domain. To this aim, both noise compensated, aberration corrected OCT image, Y, and OCT measurements, M, are assumed as graphical models defined in a random field space, S, and with the graph nodes referring to the different locations in both compensated OCT image Y and OCT measurements M.

Within the CRF modeling framework, the posterior probability, $P(Y|M)$, for the noise compensated, aberration corrected OCT image, Y, given a degraded OCT measurement M, can be formulated as,

$$P(Y|M) = \frac{1}{Z(M)} \exp(-E(M, Y)), \tag{4.6}$$

where, Z is a normalization term, known as the partition function in the CRF literature [73]. In this formulation, $E(.)$, represents a joint energy function of the following form,

$$E(M, Y) = \sum_{i \in S} \Psi_u(y_i, M) + \sum_{\varphi \in C} \Psi_p(y_\varphi, M), \tag{4.7}$$

which is defined over the assumed random fields for the noise compensated, aberration corrected OCT image, Y, and OCT measurements M. According to the formulation of Eq. 4.7, the joint energy function, $E(.)$, is a combination of the unary potential function $\Psi_u(.)$ and the pairwise potential function $\Psi_p(.)$ which are standard terms in formulation of any types of CRF modeling. Here, i, refers to the each single location of the defined graphs (random fields) for both compensated OCT image Y and OCT measurements M.

To perform C-OCT imaging, a distance based unary potential function is incorporated to the formulation of Eq. 4.7,

$$\Psi_u(y_i, M) = \frac{1}{\sigma\sqrt{2\pi}} exp\left(\frac{(log(m_i) - log(D(y_i, H))^2}{2\tau^2}\right). \tag{4.8}$$

which aims to encode the direct relationships that exist between the OCT measurements, m_i, and noise compensated, aberration corrected OCT image, y_i, at each location i in the graph. In this formulation, τ, is a control term which controls the impact of the designed distance based weighting function in the unary term. In the formulation of Eq. 4.8, a logarithmic transform is applied to change the multiplicative form of speckle noise to an additive noise term that is common in forward modeling formulation.

Based on the formulation of Eq. 4.8, the designed unary potential function efforts to enforce the data fidelity to the final solution of C-OCT imaging. It means that, the designed optimization problem aims to find the best estimate of the aberration corrected OCT image y_i at each single node i and with respect to the whole OCT data measurement M as it compensates for the degradations due to the effect of OCT system on captured OCT image.

The joint energy function in Eq. 4.7 is also dependent on the pairwise potential function $\Psi_p(.)$ which is defined over the set of clique structures C,

$$\Psi_p(y_{\varphi \in C}, M) = \exp\left(\frac{\|N_i - N_j\|_2}{\sigma_p}\right)(y_i - y_j);\ C = \{i, j\}, \tag{4.9}$$

and efforts to account for the interaction relationships between each pair of nodes y_i and y_j regarding to the whole OCT measurements M, when the goal is to suppress the effect of speckle noise in final estimate of C-OCT image. In the formulation of pairwise potential function, N_i and N_j respectively denote to specified neighborhood coordinates centered around the i^{th} and j^{th} locations in the compensated OCT image/OCT measurements graphs. A weighting exponential function is used to assess the similarity of two nodes y_i and y_j in those defined neighborhoods. Here, σ_p is the standard deviation that

controls the effect of pairwise potential function $\Psi_p(.)$ within a predefined clique structure C.

The designed pairwise potential function of Eq. 4.9 has the following features as such improves the performance of proposed C-OCT imaging in calculation of a noise compensated, aberration corrected OCT image.

1. The incorporated pairwise potential function, $\Psi_p(.)$ employs a set of nodes to evaluate the nodes similarity which results in better robustness of the proposed C-OCT imaging framework in the presence of speckle noise and artifacts

2. The designed pairwise potential of Eq. (4.9) takes advantage of a stochastic clique structure within a fully-connected random field modeling (SFC-CRF as explained in Section 3.2 of Chapter 3) [137]. Employing of SFC-CRF modeling basically enforces higher probability on the graph pair nodes which are closer compared to the pair nodes which are farther such that it leads to the better preservation of image boundaries and edges in the final solution of compensated OCT image.

To perform the inference step and calculate the best estimate of noise compensated, aberration corrected OCT image Y the proposed C-OCT imaging framework employs an approximation of graph cuts optimization method [173],

$$Y^{t+1} = Y^t - \rho \frac{\nabla E(M, Y)}{\nabla Y}, \tag{4.10}$$

which iteratively solves the MAP problem of Eq. 4.5 by minimizing the energy function $E(.)$ in Eq. 4.7. In this formulation, Y^t and Y^{t+1} are the calculated solutions at iterations t and $t+1$ and $\frac{\nabla E(Y,M)}{\nabla Y}$ represents the energy gradient, with ρ denoting the learning rate.

4.6 Experimental Results

The ability of the proposed C-OCT imaging to generate noise compensated, aberration corrected OCT images was evaluated using three different experiments that focused on imaging a standard USAF resolution target, a phantom composed of $1\mu m$ diameter polystyrene microspheres embedded in weakly scattering agar gel, as well as a sample of biological tissue. All OCT images used for testing the C-OCT algorithm were acquired with a research grade SD-OCT system that was designed and built by our research groups at the University of Waterloo (see Subsection 4.6.1 for system description).

4.6.1 OCT Experimental Setup

The SD-OCT has a compact fiberoptic design and is powered by a super-continuum light source (SUPER K, NKT Photonics) that generates a spectrum centered at $\lambda_c = 780nm$, and with the spectral bandwidth of $\triangle\lambda = 250nm$. A high resolution commercial spectrometer (Wasatch Photonics) interface with a NIR enhanced CCD camera (Piranha HS8K, Teledyne DALSA) was used at the detection end of the SD-OCT system. The linear array camera with 8192 pixels was used to minimize optical aberrations in the spectrometer. The light source spectrum was imaged only over ~ 4500 pixels of the camera array, thus resulting in an OCT scanning range of $\sim 2mm$ in free space. The camera captures the OCT interference fringes at $34kHz$ OCT acquisition rate. The OCT imaging probe is comprised of an achromat collimator lens ($f = 10mm$), a pair of galvanometric scanners (Cambridge Technologies), a beam expander (2 ahromat doublets with $f = 40mm$ and $f = 80mm$) and a microscope objective (Nikon NIR APO 40X/0.8).

This optical design of the OCT system provides $1.3\mu m$ axial resolution in free space which is equivalent to $0.95\mu m$ in biological tissues, assuming an average refractive index of 1.38 for the imaged tissue. Because the entrance aperture of the Nikon was under filled by $\sim 50\%$, the theoretical lateral resolution in free space was estimated to be $1\mu m$, which is larger than the theoretical resolution for the employed objective.

For all experiments, the optical power incident on the imaged object was limited to $750\mu W$. The OCT system's SNR measured near the zero delay $98dB$, while the SNR roll-off was $12dB$ over a scanning range of $1.2mm$.

4.6.2 Experimental Results

The results of all three C-OCT imaging experiments using (1) a standard USAF resolution target, (2) a microspheres phantom image and (3) a sample of porcine corneal stroma tissue are presented. The performance of proposed C-OCT imaging was compared to a regularized version of maximum likelihood based compensated imaging (RML-COCT) method which is the state of the art. The tested RML-COCT is a modified version of the proposed method in [49] which takes advantage of the standard Tikhonov regularization [154] to control the effect of speckle in calculation of compensated OCT images. The implementation of both the C-OCT and the RML-COCT algorithms was done using an embedded C++ code in MATLAB (The MathWorks, Inc.) and tested on an AMD Athlon II X3 3.10 GHz machine with 12 GB of RAM.

4.6.3 Experiment 1: Standard USAF Resolution Target

One pre-requirement for performing of C-OCT imaging using the proposed framework of Section 4.5 is to characterize the aberration function, H, for the utilized OCT configuration. To this aim, the aberration function of the utilized OCT system was experimentally characterized using imaging of a standard resolution target with the same OCT system. A chosen zoomed-in region of enface USAF resolution target OCT image which includes three horizontal bars of group 6 from element 2 is shown in Fig. 4.3(A).

The proposed C-COT imaging was used to reconstruct a compensated resolution target OCT image with incorporating the characterized aberration function, H, to the proposed C-OCT framework. The resulted noise compensated, aberration corrected resolution target OCT image is shown in Fig. 4.3(C). For the aim of comparison, the RML-COCT method was also applied to the same resolution target OCT image of Fig. 4.3(A) where the resulted compensated image is displayed in Fig. 4.3(C).

To find the best estimate of noise compensated, aberration corrected resolution target OCT image, the proposed C-COT imaging algorithm was run using different number of iterations where the optimal result was achieved using 30 iterations. To have a fair comparison between the result of the proposed C-OCT imaging and tested RML-COCT, the same number of iterations was also performed to calculate the compensated OCT image using RML-COCT imaging.

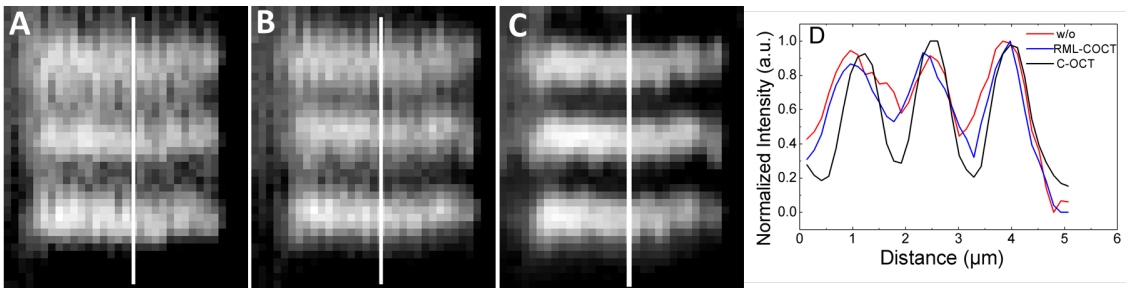

Figure 4.3: (A) Enface OCT image of USAF resolution target, group 6, element 2. (B) Same image reconstructed with RML-COCT imaging and (c) with C-OCT imaging. (D) Intensity plots obtained from the images at the locations marked with the white lines.

Considering the results of Fig. 4.3, it is obvious that the proposed C-OCT imaging is more successful in reconstruction of a noise compensated, aberration corrected OCT image and compared to the tested RML-COCT imaging. As shown in result of Fig. 4.3(C), due

to the better optical aberrations correction, the width of all horizontal bars are the same and they are within the same distance from each other compared to the original OCT image in Fig. 4.3(A) as well as compensated resolution target OCT in Fig. 4.3(B) which is generated using RML-COCT imaging.

In addition, the resulted compensated resolution target OCT images using both RML-COCT imaging in Fig. 4.3(B) and proposed C-OCT imaging in Fig. 4.3(C) show the effectiveness of both methods in terms of speckle reduction such that the amount of speckle noise greatly reduced compared to the original OCT image in Fig. 4.3(A).

To better assess the results of this experiment, the image intensity profiles for one line of resolution target OCT image, chosen across the bars at a location marked with the white lines in Figs. 4.3(A-C), is also displayed in Fig. 4.3(D). According to these intensity profiles, using of both tested RML-COCT as well as proposed C-OCT was resulted in a smoother and also narrower profiles (blue and black plots) compared to the intensity profile obtained for the original resolution target OCT image (red plot). However, from these intensity profiles, it is clear that the proposed C-OCT imaging was more successful in terms of optical aberrations correction since it was resulted in a much more narrower intensity profile (black plot) compared to the tested RML-COCT imaging (blue plot) as it is expected for an OCT imaging with less amount of aberrations.

The quantitative assessment of the results for this C-OCT imaging experiment was performed using the calculation of image SNR values for all images in Fig. 4.3(A-C) and using the following formulation,

$$SNR = 20log(\frac{\mu_R}{\sigma_R}) \tag{4.11}$$

where, μ_R and σ_R respectively denote to the mean and standard deviation of a selected homogeneous region on the OCT image.

SNR values for all images were calculated using Eq. 4.11 where the SNR value for the original resolution target OCT image measured to be $14.7dB$ and the SNR values for the compensated images using the RML-COCT imaging and C-OCT imaging measured to be respectively $15.3dB$ and $18.6dB$. This result show a significant SNR improvement using the proposed C-OCT imaging and compared to the tested RML-COCT imaging.

4.6.4 Experiment 2: Phantom Imaging

The second C-OCT imaging experiment was performed with taking advantage of a physical phantom. To this aim, a physical phantom was prepared by mixing of polystyrene

microspheres of size $1\mu m$ with the agar gel. The prepared microspheres phantom was then imaged using the same ultrahigh resolution spectral domain OCT configuration as explained in Section 4.6.1. A volumetric (512×512) OCT image was acquired from the microspheres phantom and the degradation due to the dispersion was corrected numerically up to the 9^{th} order.

The proposed C-OCT approach was used to reconstruct noise compensated, aberration corrected microspheres phantom images and with incorporation of the characterized aberration function, H, in to the framework of proposed C-OCT imaging. The proposed C-OCT imaging was tested using different number of iterations while the best optimal result was obtained using 25 number of iterations. For comparison, the tested RML-COCT was also applied to generate noise compensated, aberration corrected microspheres phantom image and with the same number of 25 iterations to have a fair comparison between the results.

A cross-sectional OCT image of the microspheres phantom is shown in Fig. 4.4 (A). The resulted compensated OCT images using tested RML-COCT and proposed C-OCT are correspondingly shown in Figs. 4.4 (B,C). To have a better representation of these results, three selected regions of interest (ROI) containing a few number of microspheres were selected for locations $110\mu m$ above, approximately at and $120\mu m$ below the focal plane in each image as such marked with the white line rectangles in Figs. 4.4(A-C). A magnified version of these ROI regions are displayed in Figs. 4.4(D-F) for locations above the focal plane, in Figs. 4.4(G-I) at the focal plane and in 4.4(J-L) for locations bellow the focal plane.

Visual assessment of the results in Fig. 4.4 clearly demonstrate the usefulness of both tested RML-COCT imaging as well as proposed C-OCT imaging in terms of speckle noise reduction which is required in all types of OCT imaging. As can be seen from these results, the produced compensated images using both RML-COCT imaging as well as C-OCT imaging show very less amount of speckle noise compared to the original microspheres phantom images in Figs. 4.4(D,G,J). However, considering the displayed ROI images in Fig. 4.4 (D-L) show that the individual microspheres from ROIs above and below the focal plane appear blurred in the original microspheres phantom images of Figs. 4.4(D,J), while the microspheres appear of smaller size, with sharp boundaries, almost round shape and of significantly higher contrast in the compensated ROI images using the proposed C-OCT imaging as shown in Figs. 4.4(F,L).

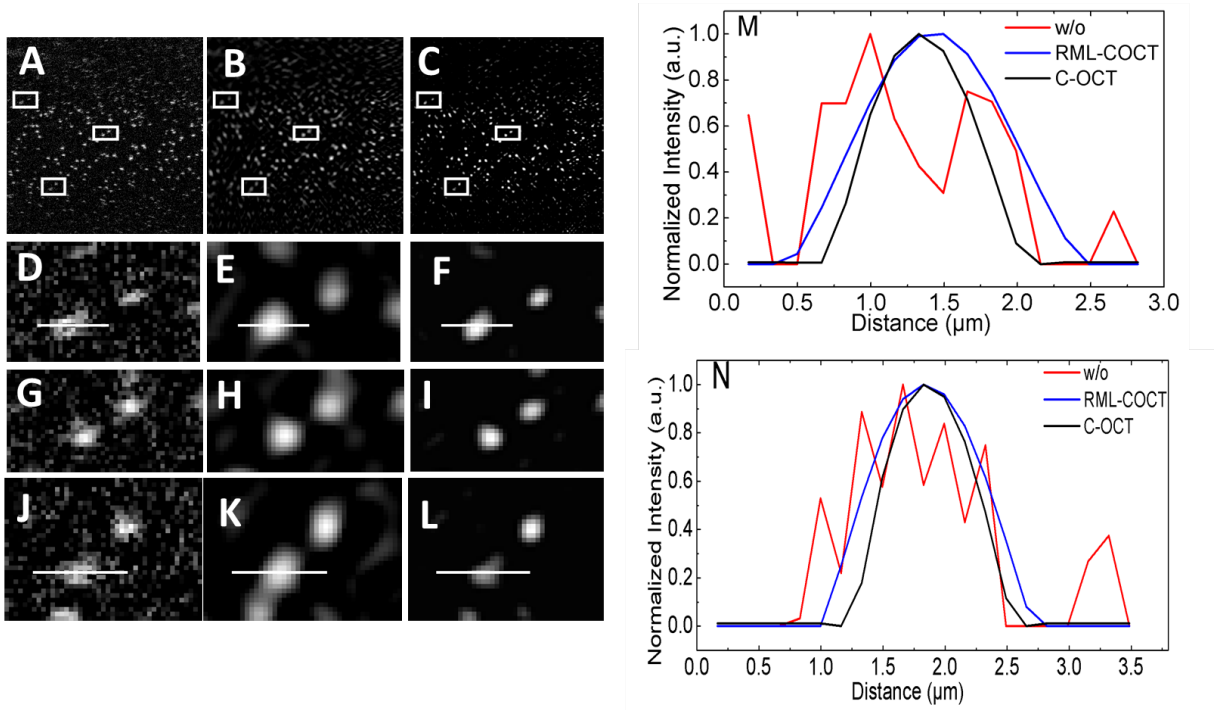

Figure 4.4: (A) Cross-sectional OCT image of a gel phantom with embedded $1\mu m$ polystyrene microspheres. (B) Same image produced with the RML-COCT and (C) C-OCT. White rectangles mark regions of interest (ROI above, at and below the focal plane). (D,G,J) Magnified copies of the marked ROIs in the original image, (E,H,K) RML-COCT image and (F,I,L) C-OCT image. (M) Intensity profiles measured along the white lines in images (D,E,F) acquired from a location above the focal plane. (N) Intensity profiles measured along the white lines in images (J,K,L) acquired from a location below the focal plane.

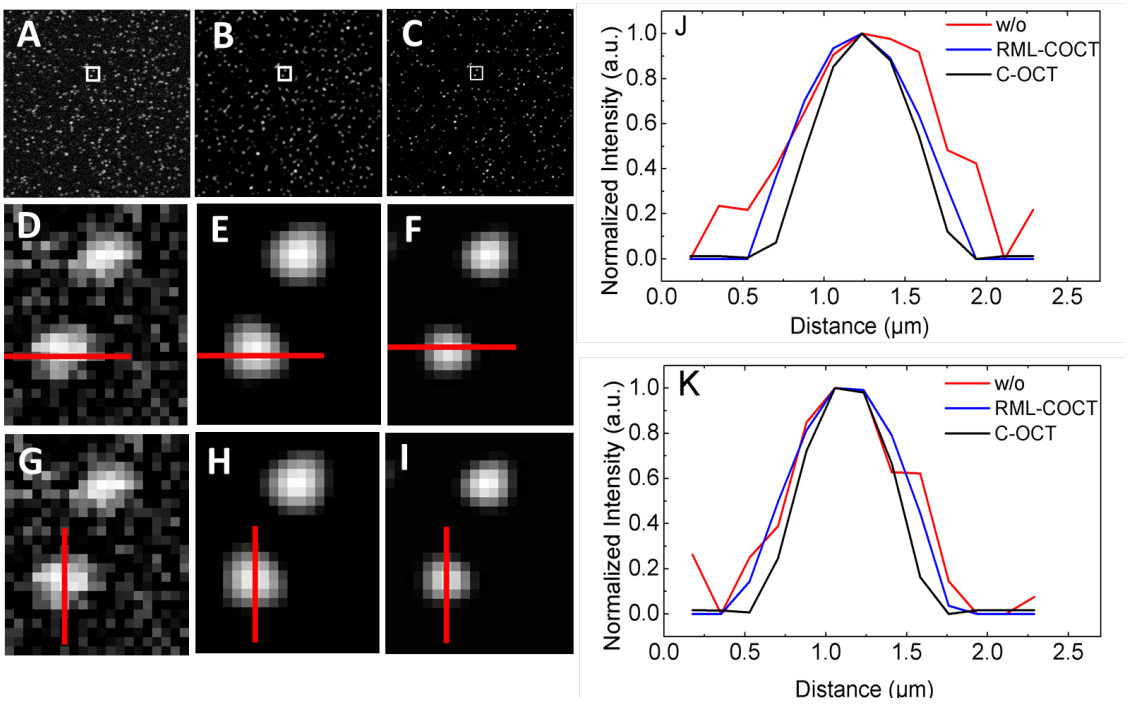

Figure 4.5: (A) Enface OCT image of microspheres acquired at the focal plane. Same region produced with the (B) RML-COCT method and (C) C-OCT framework with white rectangles marking ROIs. (D-I) Magnified images of the ROIs at the focal plane. (J,K) Lateral and axial data intensity profiles for marked lines in (D-I).

As can be seen from the results in Fig. 4.4, while RML-COCT compensates for the OCT optical aberrations to a certain degree, as observed by the shape of the microspheres in the resulting images in Fig. 4.4(E,K), the microspheres still appear blurred and of bigger size compared to the sharp, aberration corrected microspheres in the compensated images produced using the proposed C-OCT imaging in Figs. 4.4(F,L). This shows the better performance of proposed C-OCT imaging in terms of optical aberrations correction compared to the tested RML-COCT imaging.

To evaluate the efficacy of the proposed C-OCT imaging in terms of OCT lateral resolution improvement, the data intensity profiles are presented in Figs. 4.4 (M,N) and for the locations across a chosen microsphere, shown by white horizontal lines in images of Figs. 4.4(D-F and J-L). In these data intensity plots, the red color profiles is related to the original OCT image and the blue and black color intensity profiles are respectively

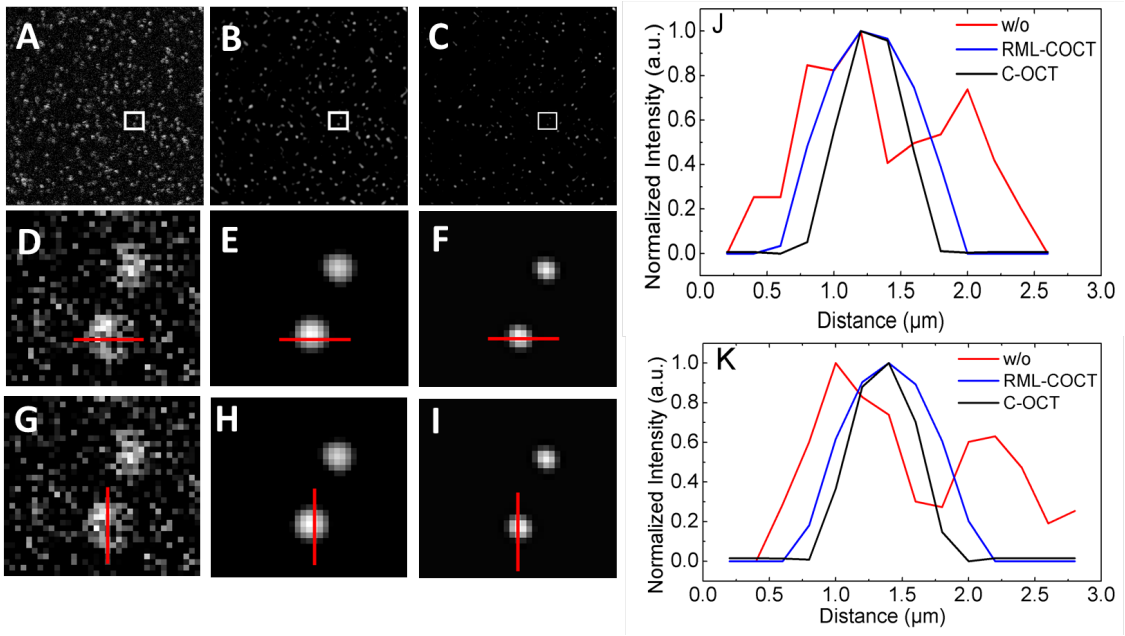

Figure 4.6: (A) Enface OCT image of microspheres acquired at $100\mu m$ bellow the focal plane. Same region produced with the (B) RML-COCT method and (C) C-OCT framework with white rectangles marking ROIs. (D-I) Magnified images of the ROIs at $100\mu m$ bellow the focal plane. (J,K) Lateral and axial data intensity profiles for marked lines in (D-I).

related to the compensated images using RML-COCT imaging and C-OCT imaging.

Evaluating both the intensity profiles in Fig. 4.4(M, N) clearly show the better correction of out-of-focus optical aberrations using the proposed C-OCT imaging. In both intensity profiles of Figs. 4.4 (M,N), the width of black color intensity profiles which is related to the compensated OCT images obtained using C-OCT imaging is less than the width of both blue and red color profiles which respectively are related to the compensated images using the RML-COCT imaging and the original OCT image. Less intensity profile width is expected when the amount of optical aberrations is better compensated.

In this experiment, to better demonstrate the performance of proposed C-OCT imaging, the enface images acquired from the microspheres phantom are also shown in Fig. 4.5(A) for the focal plane and in Fig. 4.6(A) and Fig. 4.7(A) at $100\mu m$ and $300\mu m$ below the focal plane. The compensated enface phantom images with both RML-COCT imaging and C-OCT imaging are respectively displayed in Figs. 4.5(B,C) at focal plane and Figs. 4.6(B,C) and Fig. 4.7(B,C) at $100\mu m$ and $300\mu m$ below the focal plane.

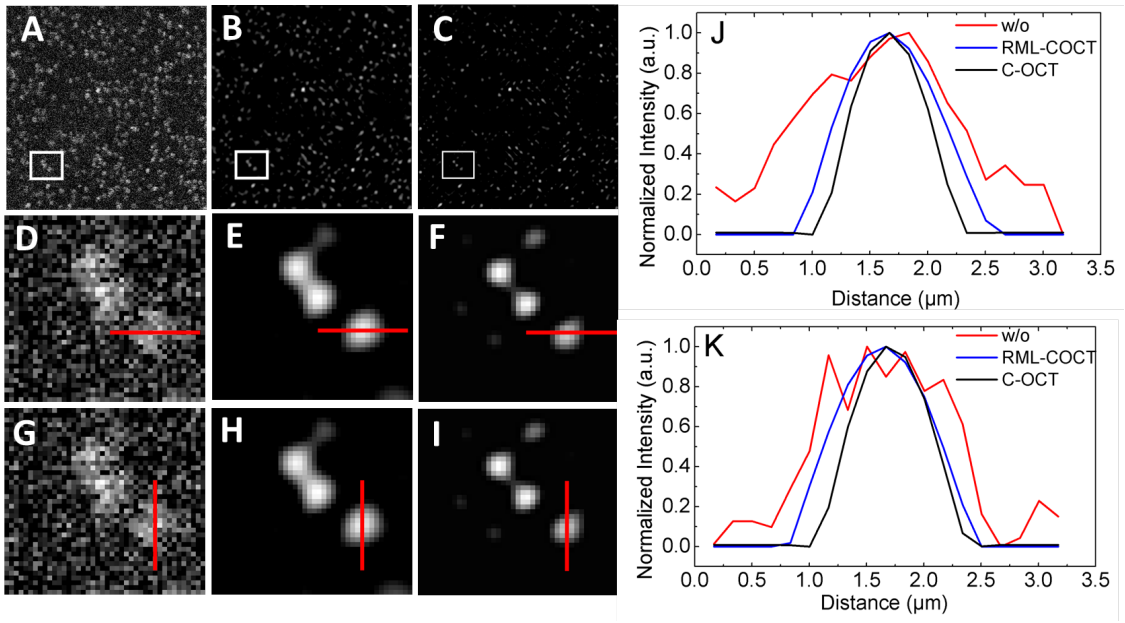

Figure 4.7: (A) Enface OCT image of microspheres acquired at $300\mu m$ bellow the focal plane. Same region produced with the (B) RML-COCT method and (C) C-OCT framework with white rectangles marking ROIs. (D-I) Magnified images of the ROIs at $300\mu m$ bellow the focal plane. (J,K) Lateral and axial data intensity profiles for marked lines in (D-I).

To better emphasize these results, ROIs containing a few microspheres were selected (locations marked with the white line rectangles) from images in Fig. 4.5(A-C), Fig. 6.5(A-C) and Fig. 4.7(A-C) and magnified versions of them are displayed in these figures. As can be observed in these zoomed in regions, the microspheres which are closer to the focal plane are exhibited as high reflective spots with less distortion in Fig. 4.5(D) while the microspheres at farther away from the the focal plane in Fig. 4.6(D) and Fig. 4.7(D) are appeared as low reflective spots with distorted shape and also with a size larger than the physical size of the microspheres. Assessing the zoomed-in results clearly show a better compensation of OCT optical aberrations using the proposed C-OCT imaging such that the compensated images in Fig. 4.5(F), Fig. 4.6(F) and Fig. 4.7(F) show better improvement in the shape and contrast for the microsphere images acquired at both near the focal plane and also at the farther depths of $100\mu m$ and $300\mu m$ from the focal plane and compared to the images in Fig. 4.5(E), Fig. 4.6(E) and Fig. 4.7(E) produced with tested RML-COCT. For example, the distinguishing between the two top shown microspheres in Fig. 4.7 (D,E) is impossible due to the existence of optical aberrations, however these two microspheres

can be easily seen in compensated image of Fig. 4.7(F) due to the perfect aberrations correction using the proposed C-OCT imaging.

To have a better intuition about the efficacy of proposed C-OCT imaging in terms of optical aberrations correction, the data intensity profiles for one line of data is also shown in Fig. 4.5(J,K), Fig. 4.6(J,K) and Fig. 4.7(J,K). The displayed data profiles are generated for both lateral and axial directions and for the locations marked with the red color lateral and axial lines around a sample microsphere in these images. The displayed data intensity profiles can generally prove the better performance of proposed C-OCT imaging in terms of optical aberrations correction such that the C-OCT data profiles (black profiles) show less width compared to the data profiles generated using the RML-COCT image (blue profiles) as well as the original OCT image (red profiles).

Again, considering the results of Fig. 4.5(E,F), Fig. 4.6(E,F) and Fig. 4.7(E,F) show the efficacy of both RML-COCT and C-OCT imaging in terms of speckle noise reduction such that the amount of speckle noise is greatly reduced in the zoomed-in images displayed in these figures.

4.6.5 Experiment 3: *ex-vivo* Imaging

In the third experiment, the performance of proposed C-OCT imaging for the aim of jointly OCT optical aberrations correction and speckle reduction in biological tissues is tested using imaging of a corneal stroma tissue. Ex-vivo OCT images were acquired from a sample of fresh porcine corneal stroma tissue preserved in buffer solution and with the same ultra high resolution spectral domain OCT configuration explained in Section 4.6.1. The OCT imaging procedures was carried out in accordance with the University of Waterloo's ethics regulations for imaging of biological tissue. As a post-processing step, the OCT dispersion was corrected numerically up to the 9^{th} order.

To calculate noise compensated, aberration corrected OCT images, the proposed C-OCT imaging was applied using the incorporation of the optimized aberration function, H in to the framework of C-OCT imaging. The proposed C-OCT imaging was tested using different number of iterations where the optimal results were acquired using 35 iterations. The results were compared to the produced image using the RML-COCT imaging and with the same number of iterations to have a fair comparison between the results.

An intensity projection OCT image of the cornea that shows part of the Descemet's membrane and the underlying corneal stroma is presented in Fig. 4.8(A). In this image, the thin white, straight lines are representing the collagen strands of the Desceme's membrane, which are appeared in focus on the original OCT image in Fig.4.8(A). The low reflective,

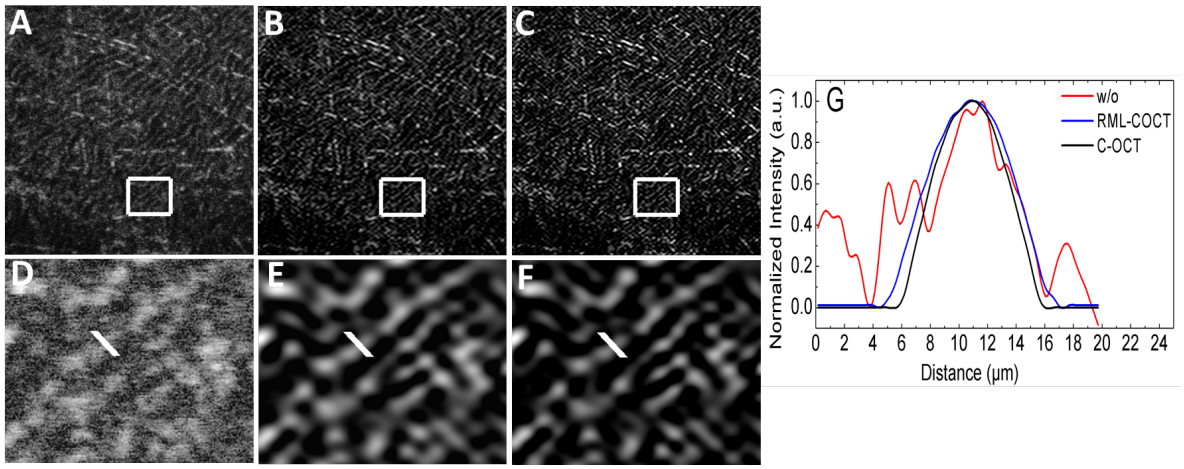

Figure 4.8: (A) OCT intensity projection images of the interface between the Descemet's membrane and the stroma of a porcine cornea, acquired *ex-vivo*. White rectangle marks ROI. Same image produced with (B) RML-COCT and with (C) C-OCT imaging. (D-F) Magnified views of the ROIs marked in images A-C. (G) Intensity profiles measured from the locations in images D-F, marked with the white lines in D-F.

wavy lines are the collagen lamellae of the stroma tissue. Since the stromal collagen lamellae in this image are located away from the focal plane, they are appeared blurred in the original OCT image of Fig. 4.8(A).

The compensated corneal OCT image produced with RML-COCT and C-OCT are respectively shown in Figs. 4.8(B,C). To have a better visualization of these results, magnified views of the ROIs selected from the images in Figs. 4.8(A-C) (white line rectangles) are also shown in Figs. 4.8(D-F) respectively.

The produced images using both tested RML-COCT as well as proposed C-OCT imaging was resulted in the significant reduction of speckle noise as can be observed in the images of Figs. 4.8(E,F). The out-of-focus collagen lamellae of the stroma appear blurred in the original OCT image as shown in Fig. 4.8(D) and more sharper in the compensated images produced with C-OCT imaging in Fig. 4.8(F) and compared to the compensated corneal OCT image using tested RML-COCT in Fig. 4.8(E). This results confirms the better performance of proposed C-OCT imaging for the aim of jointly optical aberrations correction as well as speckle reduction in OCT imaging.

To further evaluate the results of this experiment, the intensity profiles acquired across a single fiber at locations marked with the white lines in Figs. 4.8(D-F), are also shown in

Fig. 4.8(G). The intensity profiles show that both RML-COCT and C-OCT imaging are able to compensate the out-of-focus optical aberrations as resulted in a smoother, narrower intensity profiles and with less side-lobes. However, from the plotted intensity profiles of Fig. 4.8(G), it can be said that, the proposed C-OCT imaging can compensate better for the out-of-focus optical aberrations as the related intensity profile (black intensity profile) is more narrow compared to the intensity profile of RML-COCT imaging (blue intensity profile).

For quantitative assessment and comparison of the experimental results, the SNR values for all OCT images in Figs. 4.8(A-C) are also calculated using Eq. 4.11. The image SNR for the cornea image was measured to be $21.8dB$, while the SNR for the RML-COCT and C-OCT images were measured to be $24dB$ and $27.9dB$ respectively. This show the SNR improvement of $\sim 6dB$ using the proposed C-OCT imaging.

4.6.6 Time Analysis

For all experiments described above, a computation time analysis was performed to assess the computational efficiency of the proposed C-OCT imaging compared to the tested RML-COCT imaging, when the acquired time shows that the tested RML-COCT is in average 1.2 times faster than the proposed C-OCT imaging.

4.7 Summary

A novel unified random based computational compensated OCT (C-OCT) imaging was proposed for the aim of generating compensated OCT images of better quality. The designed C-OCT imaging framework was set to jointly compensate for the OCT degradations due to the optical aberrations and speckle noise. Experimental results using different OCT data showed that the proposed C-OCT imaging is a promising computational approach for the quality enhancement of OCT imaging. The overall SNR and contrast of OCT imaging increased with the use of proposed C-OCT imaging and compared to the tested state-of-the-art RML-COCT imaging. The proposed C-OCT imaging framework can be modified in the future works to account for other types of OCT degradations and to better improve the quality of OCT imaging through a purely computational approach. This could be beneficial for the quality enhancement of different types of OCT with no need to do any hardware modifications on the OCT system and therefore can be a good replacement for the hardware-based OCT compensation techniques.

Chapter 5

Compensated Super Resolution Optical Coherence Tomography

In this chapter, a compensated super resolution OCT (C-SR-OCT) framework is proposed for enhancement of the OCT image quality and particularly the OCT spatial resolution. The C-SR-OCT is designed within the same probabilistic compensated medical imaging framework that was discussed in Chapter 3. The proposed C-SR-OCT aims to jointly correct for the different factors that can degrade the OCT image resolution and SNR by utilizing a SR-based compensation approach. The general idea of SR-OCT is described in Section 5.1 with a brief review of publications related to the proposed novel SR-OCT imaging approach. The main formulation and design of the proposed C-SR-OCT method is presented in Section 5.2. Validation test results for the C-SR-OCT framework are presented and discussed in Section 5.3. A summary of the chapter is provided in Section 5.4.

5.1 Super Resolution OCT

SR-OCT is a promising computational strategy that can be used for the aim of quality enhancement in OCT imaging. To perform SR-OCT, multiple low resolution OCT images need to be acquired from the same location of the imaged sample and combined together to form a higher-quality OCT (SR-OCT) image. The main idea of SR-OCT is supported by work in the field f general image super-resolution, which has become popular in different fields and applications [95].

In a typical OCT imaging procedure, individual OCT data acquisitions are often subject to a sample or beam motion plus noise which overall leads to capturing of OCT images

with subtle different and unique information of the imaged tissue. Therefore, by combining multiple such images, a new OCT image of higher spatial resolution can be obtained.

A number of computational methods can be used to generate SR-OCT images. One simple approach would be to perform an averaging on a set of degraded OCT images to increase the SNR of resulted SR-OCT image [136, 148]. The averaging based SR OCT assumes a stationary condition for both imaged tissue and scanning beam during the OCT image acquisition. However, this assumption is generally incorrect due to the motion of sample beam (for example: in case of jitter and non-linearity of the galvanometric scanners) or due to the motion of sample itself (for example: biological noise such as breathing and heart rate, saccades in the eye). To solve this issue, in a previous study, a regularized dynamic programming algorithm was first applied to compensate for the motion between multiple OCT images following by an averaging step to generate SR-OCT image with higher SNR and more contrast [55]. A Kernel Based Interpolation (KBI) approach was proposed to produce a SR-OCT image from a set of aligned Low Resolution OCT images (LR-OCT) [127]. A Multi Penalty Conditional Random Field (MPCRF) approach for performing of SR-OCT was proposed to produce SR-OCT images with better resolution using a set of LR-OCT acquisitions [14]. This method takes advantage of multiple defined prior terms added to a general CRF framework to enforce the final solution of SR OCT imaging to be of higher spatial resolution. A multi frame SR-OCT technique was proposed for the OCT lateral resolution enhancement [141]. A SR-OCT approach using modified back projection method was developed to enhance the quality of OCT images [155].

5.2 Compensated Super Resolution OCT Formulation

Here, we propose a novel C-SR-OCT computational approach which takes advantage the probabilistic compensated medical imaging framework of Chapter 3 to generate a SR-OCT image using multiple degraded OCT measurements. The developed C-SR-OCT framework is designed to jointly correct for several OCT degradations factors including the 1) blurring due to the effect of OCT PSF function, (2) speckle noise as well as (3) motion artifact in a unified computational framework.

Assuming $M = \mathcal{F}^{-1}(M(\omega))$ is a degraded OCT measurement in spatial domain, where $\mathcal{F}$ denotes the Fourier transform, and $M(\omega)$ represents the degraded OCT data acquisition in k-space domain, a C-SR-OCT framework using a set of degraded OCT measurements, $M_k, k = 1, 2, ..., W$, can be formulated as a general forward problem,

$$log(M_k) = log(D_k(Y)) + log(\aleph_{spk}) \tag{5.1}$$

where, $D_k(.)$ models the overall OCT degradation function (observation function in SR imaging literature) which models the OCT degradations due to the (1) effect of OCT PSF and also (2) motion artifact and with $\aleph_{spk}$ denoting to the speckle noise for each single OCT measurement. Here, a logarithmic transform is used to change the multiplicative form of speckle noise to an additive noise term that is common in forward modeling formulation.

According to the formulation of Eq. 5.1 and with assuming both OCT measurements, $M_k, k = 1, ..., W$ as well as C-SR-OCT image, Y, as random fields, the proposed C-SR-OCT framework aims to find the best estimate of C-SR-OCT image, Y, trough solving an inverse problem,

$$\hat{Y} = arg\,max\, P(Y|M_1, M_2, ..., M_W) \tag{5.2}$$

which is designed in a Maximum A Posteriori (MAP) framework. Here, $P(Y|M_1, M_2, ..., M_W)$, is the posterior conditional probability of C-SR-OCT image, Y, given a set of degraded OCT measurements, $M_k, k = 1, 2, ..., W$, which can be modeled as,

$$P(Y|M_1, M_2, ..., M_W) = \frac{1}{Z(M_1, M_2, ..., M_W)} exp(-E(Y, M_1, M_2, ..., M_W)) \tag{5.3}$$

where, Z is a normalization term, and $E(.)$ is a joint energy function defined over multiple OCT measurements, $M_k, k = 1, ..., W$ and the C-SR-OCT image Y. The joint energy function can be formulated as,

$$E(Y, M_1, M_2, ..., M_W) = \sum_{i \epsilon S} \Psi_u^{sup}(y_i, M_1, M_2, ..., M_W) + \sum_{\varphi \epsilon C} \Psi_p^{sup}(y_\varphi, M_1, M_2, ..., M_W) \tag{5.4}$$

which is a combination of the unary and pairwise potential functions, $\Psi_u^{sup}(.)$ and $\Psi_p^{sup}(.)$. Similar to the proposed C-OCT imaging in Chapter 4, a distance based unary potential function is used,

$$\Psi_u^{sup}(y_i, M_1, ..., M_W) = \frac{1}{\sqrt{2\pi}} exp\left(\frac{\sum_{k=1}^{W}(log(m_{i,k}) - log(D_k(y_i))^2}{2\tau_{sr}}\right). \tag{5.5}$$

which aims to encode the direct relationships that exist between each OCT measurement, $m_{i,k}$, and C-SR-OCT image, y_i, at each location i in the assumed graph while accounts for the OCT degradations due to the effect of (1) OCT PSF as well as (2) motion artifact among multiple OCT images using the degradation function, $D(.)$, and with respect to the multiple OCT measurements, $M_k, k = 1, ..., W$. Here, τ_{sr} is a constant factor which controls the impact of the designed distance based unary term in the final solution of C-SR-OCT imaging. In the formulation of Eq. 5.4, the pairwise potential function, $\Psi_p^{sup}(.)$,

is modeled as,

$$\Psi_p^{sup}(y_{\varphi\in C}, M_1, ..., M_W) = \sum_{k=1}^{W} \exp\left(\frac{\|N_{i,k} - N_{j,k}\|_2}{\sigma_{sr}}\right)(y_i - y_j);\ C = \{i, j\}, \tag{5.6}$$

which models the pairwise interactions between each pair nodes y_i and y_j regarding to the multiple OCT measurements $M_k, k = 1, ..., N$, when the goal is to find the best estimate of C-SR-OCT image, Y. Here, $N_{i,k}$ and $N_{j,k}$ respectively denote to specified neighborhood coordinates centered around the i^{th} and j^{th} locations in the assumed graphs for the k^{th} OCT data acquisition. The designed pairwise potential function takes advantage of a weighting exponential function to assess the similarity of two nodes y_i and y_j in the defined neighborhoods. In this formulation, σ_{sr} is the standard deviation that controls the effect of pairwise potential function $\Psi_p^{sup}(.)$ within a specific clique structure C. Using the designed pairwise potential function basically compensates for the speckle noise in final solution of C-SR-OCT image.

To find the final solution of C-SR-OCT imaging, an approximation of graph cuts optimization method is applied [173],

$$Y^{t+1} = Y^t - \rho\frac{\nabla E(M, Y_1, ..., Y_W)}{\nabla Y}, \tag{5.7}$$

which iteratively solves the MAP problem of Eq. 5.2 by minimizing the joint energy function, $E(.)$. In this formulation, Y^t and Y^{t+1} denoting to the final estimate of C-SR-OCT image at iterations t and $t+1$ and $\frac{\nabla E(M,Y_1,...,Y_W)}{\nabla Y}$ represents the energy gradient, with ρ denoting the learning rate.

5.3 Experimental Results

To evaluate the effectiveness of the proposed C-SR-OCT framework in terms of reconstructing a C-SR-OCT image of higher quality by using a set of low quality OCT images, the proposed C-SR-OCT was applied to a set of simulated OCT data as well as a real OCT data acquired from two different experiments.

OCT images were acquired in-vivo from the human and the rat retina. All OCT images were acquired with a high speed, ultrahigh resolution SD-OCT configuration system operating in the $1060nm$ spectral range, which provided $\sim 3\mu m$ axial and $\sim 5\mu m$ lateral resolutions in the rat retina and $\sim 5\mu m$ axial and $\sim 15\mu m$ lateral resolutions in the human retina. All imaging procedures received full ethics clearance from the University of Waterloo Human and Animal Research Ethics Committees.

5.3.1 Experiment 1: C-SR-OCT Using Simulated OCT Data

To generate simulated degraded OCT data, a volumetric set of OCT images of size 512 × 512 × 1000 was acquired in-vivo from the human retina optic nerve head of a healthy subject. Degraded OCT images of size 128 × 128 pixels were then generated from the original retinal OCT images by enforcing a sub-pixel translational shifts of up to 4 pixels in both horizontal and vertical directions that simulates a motion artifact between the multiple OCT acquisitions followed by a decimation factor of 4 pixels with respect to the original retina image. A sample of original retinal OCT image of size 512 × 512 pixel is shown in Fig. 5.1(A) with the corresponding degraded simulated OCT image of size 128 × 128 pixels in Fig. 5.1(B).

To perform C-SR-OCT, the simulated motion was incorporated to the degradation function $D(.)$ in Eq. 5.1. The OCT PSF was modeled using a Gaussian blurring function and was incorporated to the degradation function, $D(.)$ in Eq. 5.1 while it was characterized using a set of degraded simulated OCT measurements and through an iterative blind optimization approach. Three degraded simulated retinal OCT images were used to generate a C-SR-OCT image using of the proposed C-SR-OCT.

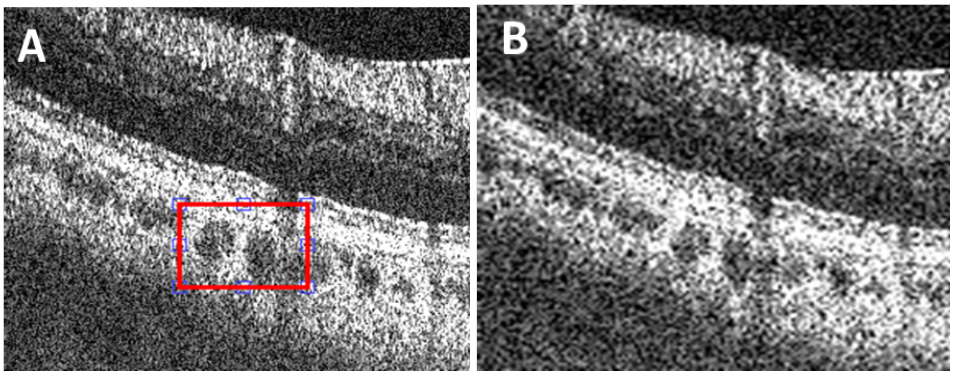

(a) (b)

Figure 5.1: (A) original human retina OCT image of size 512x512 pixels, (B) a sample of degraded simulated human retina OCT image of size 128x128 pixels.

The proposed C-SR-OCT was compared to the (1) simple SR OCT imaging using averaging method as well as (2) the previously published MPCRF SR-OCT which is the state of the art. All SR-OCT methods were implemented using MATLAB software and were tested on an AMD Athlon II X3 3.10 GHz machine with 12GB of RAM. The parameters of

tested MPCRF SR-OCT imaging were set to the best resulted value listed in the previously published paper [14]. To have a fair and consistent comparison between the results of all tested methods, the same number of degraded OCT images were utilized for generating of a SR-OCT images using all methods.

Identification and characterization of different morphological structures of the human retina such as retinal layers, as well as blood vessels (dark circular regions in the image) is challenging using the degraded simulated OCT image of Fig. 5.1(A) due to the low image resolution, blurring effects and also the presence of speckle noise. Retinal images generated using the SR-OCT methods are shown in Fig. 5.2.

A visual comparison of the SR-OCT image results for all tested methods as shown in Fig. 5.2 shows the outperforming of proposed C-SR-OCT for the aim of OCT quality enhancement. Using the proposed C-SR-OCT framework is resulted in better and clearer visualization of the different retinal layers as well as retinal blood vessels in reconstructed C-SR-OCT image using the simulated retinal OCT image (compare Figs. 5.2(B and E)). The blood vessel boundaries as well as the boundaries between the individual retinal layers are sharper and can be distinguished better from the surrounding tissue in the reconstructed C-SR-OCT image using the proposed C-SR-OCT, shown in Fig. 5.2(E) and compared to the state of the art MPCRF SR-OCT imaging results, shown in Fig. 5.2(D) as well as averaging based SR-OCT imaging result as shown in Fig. 5.2(C).

The results presented in Fig. 5.2 also show the efficacy of the proposed C-SR-OCT for speckle noise suppression which in turn lead to improved image contrast and better visualization of fine morphological structures in the retinal tissue. This interpretation of results can be better appreciated by comparing the zoomed in regions shown in Fig. 5.2(F-J). These zoomed-in regions show an example of retina blood vessels intersection that could be better observed in the produced C-SR-OCT image of Fig. 5.2(J) using proposed C-SR-OCT.

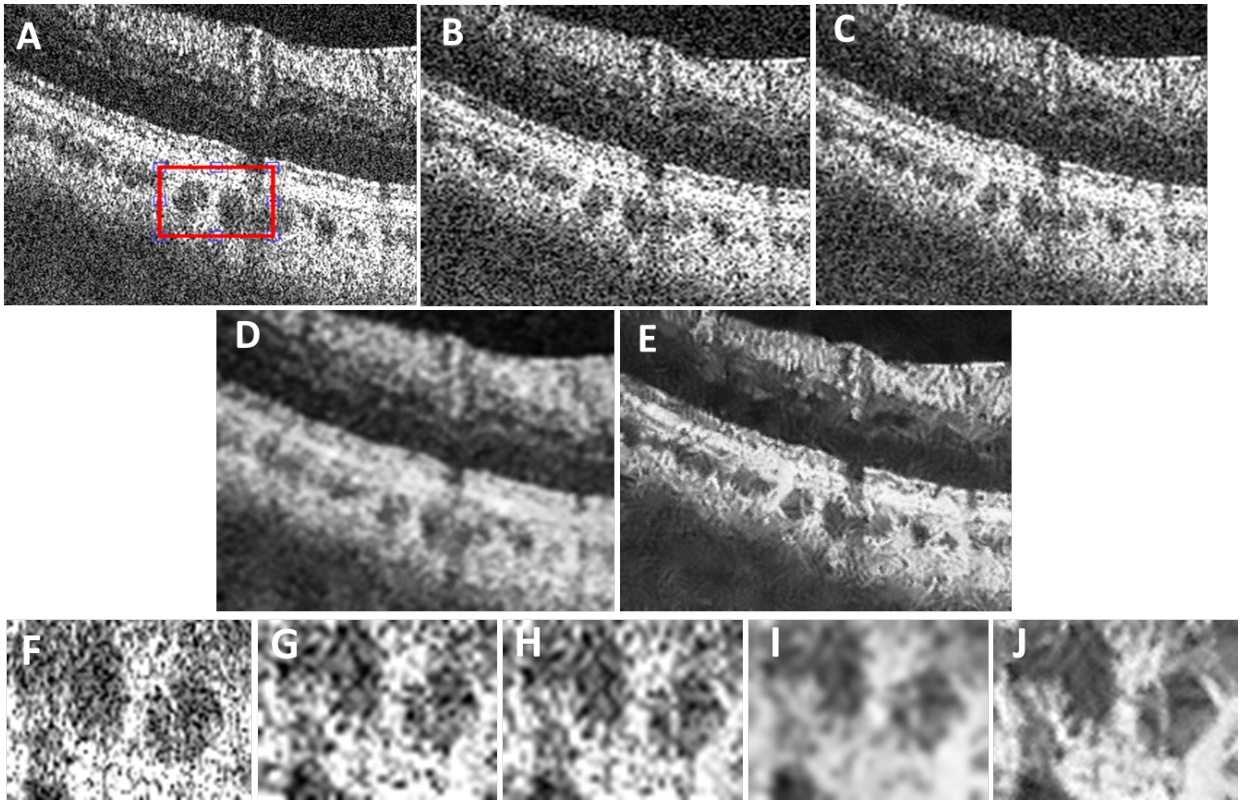

(a)

Figure 5.2: (A) Original human retina OCT image of size 512x512 pixels, (B) a sample of degraded simulated human retina OCT image of size 128x128 pixels. Reconstructed images using (C) averaging method, (D) MPCRF method and (E) proposed C-SR-OCT imaging. (F-J) zoomed regions of the blood vessel area in images (A-E) marked with the red box in the original OCT image in (A).

5.3.2 Experiment 2: C-SR-OCT Using Real OCT Data

To better evaluate the performance of proposed C-SR-OCT in case of real OCT data, the proposed C-SR-OCT framework was also tested on a set of 3 consecutive OCT images acquired in-vivo from the same location of the rat retina tissue. Fig. 5.3 shows a representative cross-sectional OCT image acquired in-vivo from the rat retina. Visualization of the major retinal layers as well as small size morphological features such as reflections from individual retinal blood cells is difficult using the degraded OCT retinal image in Fig. 5.3.

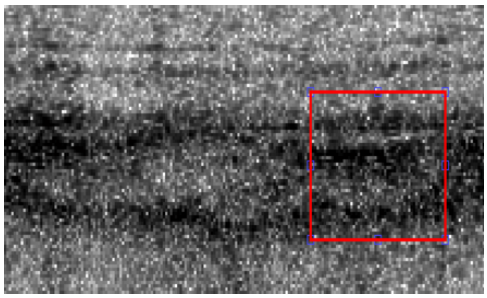

Figure 5.3: A cross-sectional OCT image acquired in-vivo from the rat retina.

To generate a C-SR-OCT image using the rat retinal OCT data, the proposed C-SR-OCT imaging was performed by accounting for a resolution enhancement factor of 2 pixels in each dimension. The motion between the three rat retina OCT images resulting from the eye motion was estimated using a cross-correlation method [42]. The estimated motion artifact was incorporated to the degradation function, $D(.)$ in Eg. 5.1. The same OCT PSF function, estimated using the experimented simulated OCT data was used for reconstruction of a SR-OCT image using the real rat data when it is incorporated to the modeling of degradation function, $D(.)$, in Eq. 5.1.

To evaluate the performance of proposed C-SR-OCT in working with the rat retinal OCT image, the proposed C-SR-OCT was also compared to the SR-OCT imaging using (1) averaging method as well as (2) MPCRF SR-OCT imaging method. All SR-OCT imaging methods were implemented using MATLAB software and were tested on an AMD Athlon II X3 3.10 GHz machine with 12GB of RAM. To satisfy the consistency of the results comparison, the same number of rat retinal OCT images was utilized to perform all tested SR-OCT imaging methods.

The results of all tested SR-OCT methods for generating a C-SR-OCT image using three degraded rat retinal OCT measurements is shown in Fig. 5.4. Similar to the results of the previous experiment, applying of the proposed C-SR-OCT was resulted in better

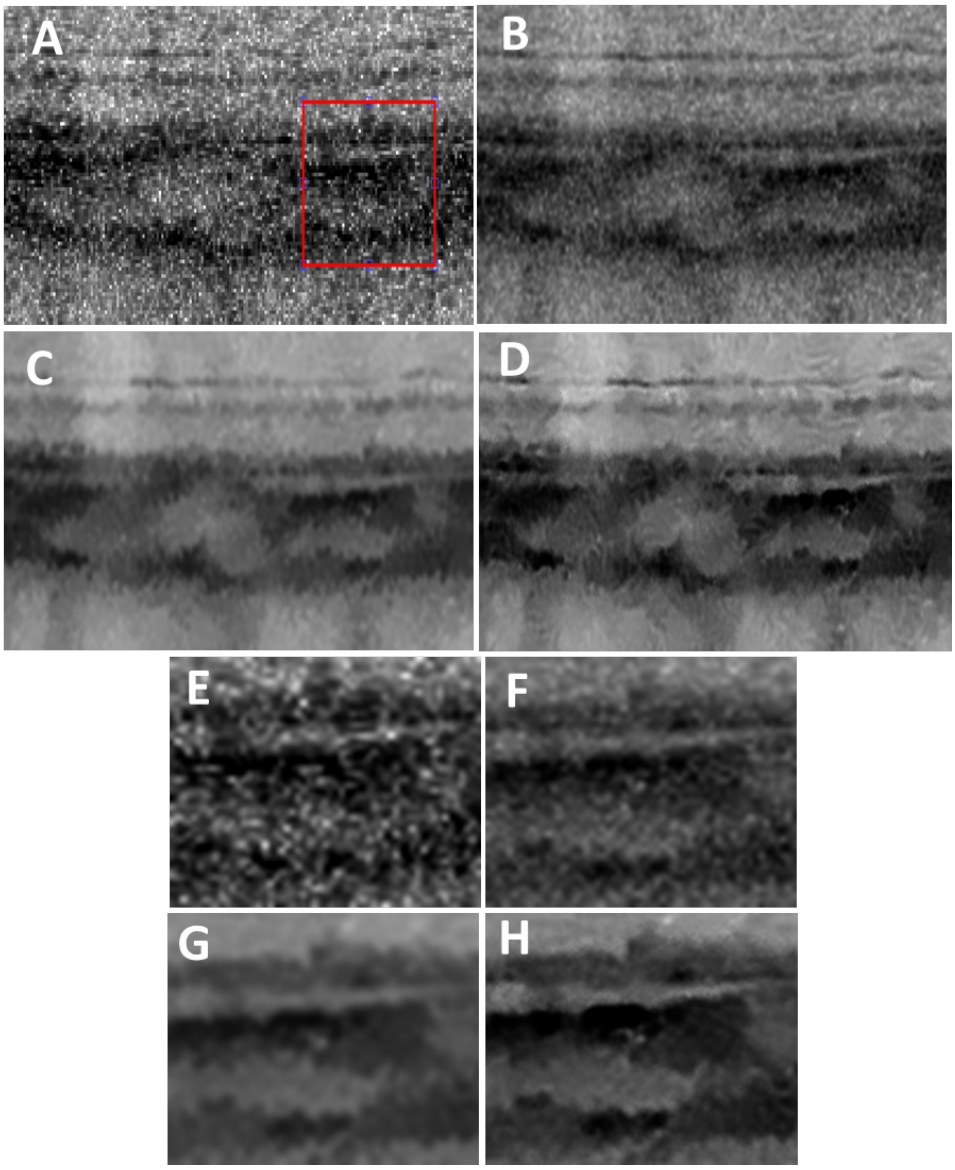

(a)

Figure 5.4: (A) Original in-vivo rat retinal OCT image, reconstructed C-SR-OCT images using (B) averaging based SR-OCT, (C) MPCRF SR-OCT and (D) proposed C-SR-OCT methods. (E-H) Zoomed-in regions of the area marked with the red box in original rat retina OCT image in (A).

preservation and visualization of different morphological features and structures of the rat retina such as the individual retinal layers and blood vessels as can be seen by comparing of the reconstructed SR-OCT images shown in Figs. 5.4(A,D).

For a closer comparison of the results, a region of interest (ROI) as marked with red box in Fig. 5.4(A) is chosen and a magnified view of that ROI is displayed in Fig. 5.4(E-H) for all tested methods. The zoomed-in regions show that although the state-of-the-art MPCRF SR-OCT imaging greatly reduced the effect of speckle noise, it leads to the blurring of some image regions which is undesired. As it can be seen from these results, the blood vessel boundaries and retinal layers are sharper and therefore better visualized in the produced C-SR-OCT image of Fig. 5.4(H) and compared to the resulted SR-OCT image using the tested MPCRF-SR-OCT imaging as shown in Fig. 5.4(G). These results demonstrate the superior performance of proposed C-SR-OCT for jointly correcting for the degradations due to the OCT PSF and speckle noise.

5.3.3 Quantitative Analysis of Results

To quantitatively assess the performance of the proposed C-SR-OCT, Contrast-to-Noise Ratio (CNR) and Equivalent Number of Looks (ENL) are calculated,

$$CNR = \frac{1}{R}\left[\sum_{r=1}^{R} \frac{(\mu_{r1} - \mu_{r2})}{(\sigma_{r1}^2 + \sigma_{r2}^2)}\right] \tag{5.8}$$

$$ENL = \frac{1}{H}\left[\sum_{h=1}^{H} \frac{\mu_h^2}{\sigma_h^2}\right] \tag{5.9}$$

In formulation of CNR, μ_{r1} and μ_{r1} are the mean values for the two defined regions on the OCT image and σ_{r1} and σ_{r2} respectively denote to the standard deviations for those arbitrary ROIs. ENL metric measures the smoothness of an image in specified homogeneous areas, where a greater value depicts a smoother area. In formulation of ENL, μ_h and σ_h respectively refer to the mean and the variance of a chosen homogeneous ROI on OCT image. The calculated CNR and ENL values for all tested SR-OCT imaging methods and for both experiments using the simulated human retina as well as real rat retina OCT images are respectively reported in Table 5.1 and Table 5.2. As the reported CNR values in both Table 5.1 and Table 5.2 show, the proposed C-SR-OCT achieved the highest CNR values compared to that of other tested SR-OCT methods, with an improvement of $\sim 10dB$ over the original OCT image and for both experiments using the simulated and real OCT

Table 5.1: Image quality metrics evaluated for the different tested SR-OCT methods calculated using the SR-OCT images reconstructed from simulated human retina image.

Method	CNR (dB)	ENL
original	2.68	6.95
Averaging	5.03	12.47
MPCRF	8.99	69.24
C-SR-OCT	**12.18**	**78.56**

Table 5.2: Image quality metrics evaluated for the different tested SR-OCT methods calculated using the SR-OCT images reconstructed from rat retinal image.

Method	CNR (dB)	ENL
original	3.64	62.07
Averaging	9.18	224.52
MPCRF	11.09	**500.63**
C-SR-OCT	**12.27**	495.23

data. This quantitative assessment also confirms our previous interpretation of the results as it shows better discrimination of the blood vessels from the surrounding tissue due to the image contrast improvement as it is visible in the results of both Fig. 5.2 and Fig. 5.4.

Furthermore, assessing of the reported values for the ENL metric in both Table 5.1 and Table 5.2 shows a considerable improvement of ENL values (higher ENL values) for the both proposed C-SR-OCT method and tested MPCRF-SR-OCT when it compares to the original OCT image as well as the produced SR-OCT image using averaging based SR-OCT. This quantitative results also confirms our previous visual interpretation of results for both reported experiments using the simulated and real OCT data. Based on all the qualitative and quantitative results, both of the proposed C-SR-OCT and tested MPCR-SR-OCT methods resulted in obtaining smoother images from homogeneous areas of sample such as the nerve fiber layer tissue surrounding the blood vessels in both the hu-

man retina and the rat retina images while the proposed C-SR-OCT could better preserve the fine structures of the tissue compared to the tested MPCRF-SR-OCT method.

5.4 Summary

A C-SR-OCT was proposed for the quality enhancement in OCT imaging and using a set of degraded OCT images. The designed C-SR-OCT was set to simultaneously correct for the multiple OCT degradations due to the (1) OCT PSF, (2) motion artifact as well as (3) speckle noise within a probabilistic based SR imaging framework. Testing of the designed C-SR-OCT using both simulated and real multiple OCT measurements demonstrate the power of proposed computational framework for generating a high quality OCT image from multiple low quality OCT images. The proposed C-SR-OCT can be used for the quality enhancement of different OCT data using various OCT configurations and without the need for any hardware modification of the OCT system configuration.

Chapter 6

Compensated Magnetic Resonance Imaging

In this chapter, a compensated magnetic resonance (CMR) imaging is developed and designed for the aim of quality enhancement in MR imaging. The developed CMR imaging is designed within the framework of proposed probabilistic compensated medical imaging that is explained in Chapter 3. The proposed CMR imaging is developed to jointly correct for several MR degradation issues including (1) MR aberrations due to intrinsic properties of MR scanner, (2) bias field inhomogeneity, as well as (3) inherent MR noise in a unified computational framework. This chapter begins with introducing MR imaging and different MR modalities in Section 6.1 following by explaining about MR image degradation factors in Section 6.2. A brief review of the most popular proposed methods for correction of each explained MR degradation issue is also provided in Section 6.2. The proposed CMR imaging framework is designed and formulated in Section 6.3. Experimental results using the developed CMR imaging are presented and discussed in Section 6.4. A short summary of this chapter is provided in Section 6.5.

6.1 Magnetic Resonance Imaging

Magnetic resonance imaging (MRI) is a standard and well-known imaging technique that has found various applications in both diagnosis and medical research. MR scanners basically takes advantage of a strong magnetic field, radio frequency signals and field gradients to generate MR images from different organs and soft tissues such as brain, breast tissue, lung and prostate [68].

MR imaging works based on the magnetization property of water molecules which contain hydrogen nuclei (protons). To perform an MR imaging, one MR scanner applies a strong magnetic field (B_0) to the target organ/tissue such that the proton spins of the tissue/organ are getting aligned with the magnetic field direction. Applying of an electromagnetic radio frequency (RF) pulse at the resonance frequency of protons leads to the generation of a varying magnetic field (B_1) which causes that the aligned proton spins flip (90^0 or 180^0). The resonance frequency of protons depend on the strength of the applied magnetic field. The excited protons gradually precess to the normal spin position by turning of the RF field and as they lose the absorbed RF energy such that generate an MR signal. A gradient coil is also used to change the strength of magnetic field at different positions and therefore change the precession frequency of the proton spins along the direction of the field gradients which allows for the spatial encoding of the acquired MR signal. Finally, an MR image can be calculated using the 2-D Fourier transform of the recorded spatial frequencies MR signal [68].

In MR imaging technique, the number of radio frequency pulses and gradients determine an MR sequence. Different MRI modalities are developed with the use of various types of MR sequences while each measure specific tissue properties and therefore is suitable for displaying of different details and structures of the imaged tissue [17]. One typical type of MR modalities is the T2-weighted MRI which generates MR images with relying on the differences in the T2 relaxation time of the tissue. T1-wighted MRI is another modality that takes advantage of calculating the differences in T1 relaxation times of the tissue to generate MR images. PD-weighted MRI is another MR modality which translates the difference of proton density between the various tissues to an MR image such that tissues/regions with more proton density appear brighter in the resulted MR image. Diffusion-weighted MR (DW-MR) imaging is another type of MR modality which produces MR images by measuring of the random Brownian motion of water molecules that happens inside the tissue. Defining the exact relation between the tissue histology and the diffusion is always complicated, however, in general, denser tissues (for example cancerous tissue) typically show lower diffusion such that it can be observed in the acquired DW-MR images. In DW-MR modality, the sensitivity of MR imaging to the amount of diffusion can be controlled using a specific parameter, called as b-value. Performing of DW-MR imaging with higher b-values basically increases the possibility of delineation between the healthy and cancerous tissues which is desired for having a correct diagnosis.

A combination of different MR modalities such as T1-weighted, T2-weighted, PD-weighted and DW-MR leads to a multi parametric MRI technique (MP-MRI) which can improve the performance of MR imaging by emphasizing on a combination of different features and details of the tissue [69]. This technique has found great applications for te

aim of tumor detection and localization.

6.2 Magnetic Resonance Imaging Degradations

The overall quality of all different types of MR imaging modalities can be limited due to effect of several image degradation factors such as various types of MR artifacts and noise. Using of MR images with low quality can generally affect on the correct visualization and analysis of MR images as it makes challenges for both radiologist and computer-aided methods to have a reliable interpretation of the radiology results and therefore may lead to the mis-diagnosis.

In MR imaging, different types of artifacts can be caused by a variety of factors [47]. MR imaging artifacts mainly can be classified to the different categories including the patient related artifacts (for example: motion artifact or the artifact due to the metallic implants), system related artifacts (for example: bias field artifact and shading artifact) and also those artifacts which are related to the specific properties of the imaged tissue (for example: magnetic susceptibility artifact, chemical shift artifact and dielectric effect artifact).

Compensating for each of the above mentioned MR degradations is solely important for the quality enhancement of MR imaging and can reduce further challenges for the correct analyzing and interpretation of MR images from different modalities.

In this chapter, we have designed and developed a CMR imaging framework which aims to jointly correct for the several MR degradation issues including (1) MR aberrations due to intrinsic properties of MR scanner (MRI PSF), (2) bias field inhomogeneity, as well as (3) inherent MR noise. All these MR degradation factors typically can be seen in different types of MR imaging modalities and generally reduce the overall quality of the MR imaging. A short explanation of these MR image degradation issues is provided here following by a brief review of the previous proposed methods for compensating of each MR degradation factor.

6.2.1 MR Bias Field Inhomogeneity

Bias field inhomogeneity is a recognized image degradation issue in all various types of MRI modalities. In MR imaging, Bias field inhomogeneity can arise either due to the effect of MR scanner or due to the impact of tissue/organ anatomy (for example: in EPI

imaging, the susceptibility differences at tissue/air and tissue/bone interfaces). The bias field inhomogeneity can be seen as a smooth spatially varying intensity in homogeneous areas of the imaged tissue. The effect of bias field inhomogeneity typically increases with the use of more strong magnetic fields, for example in using of $3T$ and $7T$ MRI systems. The presence of Bias field inhomogeneity makes challenges for the correct visualization of different small details and features in a captured MR image and can have a significant negative impact on the overall accuracy of the different image analyzing tasks and therefore may lead to the increased inter- and intra-observer variability for MR image interpretation. Therefore, correcting for the bias field inhomogeneity is a required step in the pipeline of MR imaging quality enhancement.

To deal with bias field inhomogeneity in MR imaging, different prospective and retrospective methods are employed with various types of MRI modalities and for the case of imaging different tissue/organs [161]. In general, prospective approaches mainly focus on correcting for the scanner-related bias fields while they take advantage of a MR phantom, multi-coil MR imaging, or specific designed MRI sequences to compensate for the effect of bias field inhomogeneity. Using of prospective bias field inhomogeneity correction methods can be complicated, more expensive and also time consuming as there is a need for adding of an extra hardware component to the MRI system or modifying MR imaging protocol.

On the other hand, retrospective approaches propose an easier, cheaper and more efficient solution for the bias field inhomogeneity correction in MR imaging. The retrospective methods basically effort to compensate for both scanner-related and anatomy-related bias field inhomogeneities and with relying on the retrieved information from the acquired MR image or some primary informations about the bias corrected MR image.

According to the literature, the most popular retrospective methods for the bias field inhomogeneity correction are the filtering based approaches, surface fitting methods, jointly bias correction and segmentation as well as histogram-based methods [161]. In general, filter-based bias correction methods assume that MR bias field inhomogeneities are largely characterized at the low frequencies and therefore can be suppressed using a low-pass filter. Bias correction using filter-based methods is generally fast and easy, but may lead to the lose of some useful low frequency image context. Surface fitting methods basically model the bias field inhomogeneities as a parametric function, for example, a polynomial or spline functions, while the overall performance of this approach is highly depends on the selection of true initial points and also choosing a correct model for the bias field inhomogeneities. Bias correction using segmentation-based approaches are designed in a way to perform an alternating bias field inhomogeneity correction and segmentation task. Here, the accuracy of the results of each step can highly affect on the other step. In addition, these methods are often time consuming, particularly if the main goal is to perform the

bias field inhomogeneity correction. Bias field inhomogeneity correction using histogram-based methods mainly rely on the image intensity histogram or image entropy to perform the bias correction task. These methods often assume a prior distribution for modeling of each specific tissue such that it may limit the effectiveness of the bias correction approach in using with other tissue types.

6.2.2 MR Noise

MR noise is one of the important image degradation factor that exist in all types of MR imaging modalities. The presence of MR noise hinders the correct visualization of different details and structures of the imaged tissue/organ and therefore makes some challenges for the further image processing tasks such as segmentation, registration and other types of required MR analyzing procedures.

In MR imaging, the main source of noise is a thermal noise which arises due to the combination of different factors such as the effect of body (tissue/organ), the MR coil as well as the electronics [25]. With assuming that the real and imaginary parts of the acquired MR data contain independent noise, the overall noise for the magnitude of an MR image is modeled using a Rician distribution [25]. With this assumption, for MR data with high SNR, the noise model can be approximated as a Gaussian probability distribution and for the regions with low SNR, the noise can be modeled using a Rayleigh distribution [100].

Due to the obvious degrading effect of MR noise on all types of MR imaging, a significant portion of MR imaging enhancement studies are assigned to develop MR noise reduction methods. One main strategy for MR denoising is to compensate for the MR noise during the data acquisition. This approach often adds to the time of data collection or reduce the spatial resolution of the acquired MR image which are undesired.

Another main strategy for MR noise correction is to take advantage of a variety of post acquisition methods which aim to perform MR denoising while preserve the image spatial resolution. A main classification of these methods divides them to the filtering approaches, transform approaches and statistical approaches [97]. Different linear and non-linear filters are designed for the aim of MR noise correction using filtering based methods. Transform based methods aim to improve the efficiency of MRI denoising by performing of noise correction in a transform domain such as the wavelet or curvelet domains. The most popular statistical based MR denoising methods take advantage of the maximum likelihood approach, linear minimum mean square error estimation, Markov random process and Bayes estimation for the aim of MR noise compensation.

6.2.3 MR Scanner Characteristics Function

Similar to all imaging systems, the effect of MR scanner characteristic function (MR point spread function) is another major source of image degradation in all types of MR imaging modalities. The effect of MR point spread function (PSF) basically appears as some inhomogeneity aberrations in a captured MR image such that degrades the spatial resolution of the acquired MR image.

Compensating for the aberration that happens due to the effect of MR scanner intrinsic properties is an important step in the pipeline of MR imaging quality enhancement.

A few studies has been done to improve the quality of MR imaging by accounting for the effect of MR scanner intrinsic properties (PSF). Regarding to this issue, an optimization of MRI scanners was performed to reconstruct MR images with higher quality [149]. Point spread function mapping technique with taking of phase gradient encoding was proposed to measure MR PSF with high spatial resolution at each single pixel [128, 177]. Super resolution reconstruction approach was also proposed as a useful image processing technique for reconstruction of a high-resolution MR image and by accounting for MR degradations due to the effect of MR scanner [21, 156]. Blind deconvolution compensation (BDC) technique was also proposed as a useful approach for the correction of MR aberrations due to the effect of MR scanner such that can produce an MR image of better quality [27].

6.3 Compensated Magnetic Resonance Imaging

In this section, we develop and design a novel compensated MR imaging (CMR) framework with taking advantage of the proposed probabilistic cross-domain compensated medical imaging framework of Chapter 3. The proposed CMR imaging is specifically designed and formulated to jointly correct for several MR degradation issues including (1) MR aberrations due to intrinsic properties of MR scanner, (2) bias field inhomogeneity, and (3) inherent MR noise in a unified computational framework. A general diagram of proposed CMR imaging is shown in Fig. 6.1.

As the general diagram of Fig. 6.1 display, the proposed CMR imaging takes advantage of a calibration procedure to obtain MR compensation function, and then leverages this information into the designed CMR imaging framework which aims to reconstruct an MR image with higher overall quality. Such a CMR imaging can be used with the different MR imaging modalities and to increase the quality of MR imaging that aids radiologists for an easier interpretation and better diagnosis of the different diseases.

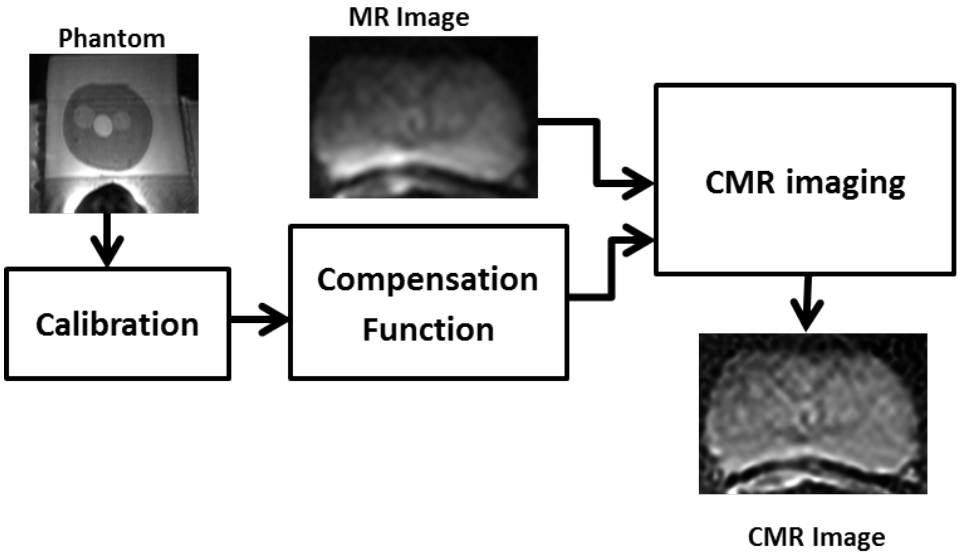

Figure 6.1: A general framework for proposed CMR imaging.

6.3.1 Problem Formulation

MR data acquisition, $M(\omega)$, from MR scanner is in k-space domain which can be transformed to the spatial domain MR data, $M = F^{-1}(M(\omega))$, with applying an inverse Fourier transform $\mathcal{F}^{-1}$. An MR image corrupted by (1) MR aberrations due to intrinsic properties of MR scanner, (2) bias field inhomogeneity, as well as (3) inherent MR noise can be expressed using a general forward model,

$$M = D(Y, b, h_{MR}) + \aleph_{MR}, \tag{6.1}$$

where, $D(.)$ represents the overall MR degradation function which jointly models the effect of MR aberrations due to intrinsic properties of MR scanner, h_{MR}, as well as MR inhomogeneities due to the existence of bias field, b. Here, $\aleph_{MR}$ denotes the inherent MR noise with Rician distribution [25].

Based on the forward problem of Eq. 6.1, CMR imaging can be modeled as an inverse problem,

$$Y = D^{-1}(M, b, h_{MR}), \tag{6.2}$$

where the goal is find the best estimate of compensated MR image, Y, through solving of the inverse problem and with taking advantage of a learned compensation function $\mathbb{C}(.) =\sim D^{-1}(.)$.

To solve the inverse problem of CMR imaging, let assume S be a random field containing set of pixels in a discrete lattice $\mathcal{L}$ upon which an MR image is defined and $i \in S$ be a pixel in $\mathcal{L}$ such that $M = \{m_i\}_{i \in S}$ and $Y = \{y_i\}_{i \in S}$ denote to the random fields for MR data acquisition M and compensated MR image, Y. To solve the inverse problem of Eq. 6.2 within the defined random field space, the proposed CMR imaging takes advantage of a general maximum a posterior (MAP) strategy,

$$\hat{Y} = \underset{Y}{argmax} P(Y|M). \tag{6.3}$$

where, $P(Y|M)$ is the posterior conditional probability of compensated image Y given MR data acquisition M which can be modeled as,

$$P(Y|M) = \frac{1}{Z(M)} exp(-E(Y, M)), \tag{6.4}$$

where, $E(.)$ is a joint energy defined defined over MR data acquisition M and compensated MR image Y. Here, $Z(.)$ determines a normalization term.

With assuming both MR data acquisition, M and compensated MR image Y as random fields, the proposed CMR imaging takes advantage of the SFC-CRF modeling [137] to define the joint energy function $E(.)$,

$$E(Y, M) = \sum_{i \in S} \Psi_u(y_i, M) + \sum_{\varphi \in C} \Psi_p(y_\varphi, M), \tag{6.5}$$

where, the joint energy function $E(.)$ is a combination of unary potential function $\Psi_u(.)$ and pairwise potential function $\Psi_p(.)$ which are standard terms in the framework of CRF modeling. Here, i, refers to the each single location in a defined graphs (random fields) for the MR acquisition/compensated MR image with C encoding a set of clique structures defined over the assumed graphical model.

In the designed CMR imaging framework, the unary potential function is defined as,

$$\Psi_u(y_i, M) = \|m_i - D(y_i, b, h_{MR})\|_2 \tag{6.6}$$

where, the goal of incorporated unary function is to enforce the data fidelity with respect to the MR data acquisition M and by jointly compensating for the MR degradations due to the intrinsic properties of MR scanner as well as bias field inhomogeneity.

To this aim, a priory knowledge about the MR PSF function h_{MR} is required. In the proposed CMR imaging, a calibration procedure with taking advantage of a standard MR phantom image is used to estimate the initial model for the intrinsic properties of the MR scanner (MR PSF) while this prior information is leveraged to the designed optimization problem of the CMR imaging that needs to be solved to find a true estimate of compensated MR image.

The joint energy function of Eq. 6.5 also takes advantage of a pairwise potential function,

$$\Psi_p(y_{\varphi \in C}, M) = exp(\frac{\|N_i - N_j\|}{\sigma_p})(y_i - y_j);\ C = \{i, j\}, \tag{6.7}$$

which attempts to account for the interaction relationships between each pair of nodes y_i and y_j regarding to the whole MR data acquisition, M, when the goal is to find the best estimate of a compensated MR image Y. To this aim, a standard exponential weighting function is employed to assess the similarity of each two nodes y_i and y_j in the specific neighborhoods N_i and N_j which are centered at the i^{th} and j^{th} locations in the assumed random field. In Eq. 6.7, σ_p is a standard deviation for the pairwise potential penalty term, defined over the clique structure C and controls the impact of pairwise term in the final estimate of compensated MR image. Employing of the designed pairwise function of Eq. 6.7 leads to the better preservation of the different details and structures of the imaged tissue/organ in the final estimate of compensated MR image Y as it controls for the effect of MR noise.

Here, employing of the SFC-CRF model is beneficial since it accounts for the long-range image pixel interactions as opposed to only using a small 4/8 pixels neighborhood for estimation of compensated MR images such that it helps for the better controlling of the noise effect in the final estimate of compensated MR images.

6.3.2 Inference

To find the best estimate of compensated MR image Y using the proposed CMR framework, the posterior conditional probability $P(Y|M)$ in Eq. 6.3 needs to be maximized through minimization of the joint energy function in Eq. 6.5. To this aim, a gradient descent algorithm is applied to solve the optimization problem of Eq. 6.3 using the following formulations,

$$Y^{t+1} = Y^t - \rho_1 \frac{\nabla E(Y, M)}{\nabla Y} \quad s.t.\ \ b \text{ is fixed} \tag{6.8}$$

$$b^{t+1} = b^t - \rho_2 \frac{\nabla E(Y, M)}{\nabla b} \quad s.t.\ \ Y \text{ is fixed} \tag{6.9}$$

where ρ_1 and ρ_2 are the defined learning rates, $\frac{\nabla E(\cdot)}{\nabla b}$ and $\frac{\nabla E(\cdot)}{\nabla Y}$ are the gradient of energy regarding the bias field b and compensated MR image Y. According to the formulation in Eq. 6.8 and Eq. 6.9, the bias field b and compensated MR image M are estimated in an interchanging fashion. Here, Y^{t+1} and Y^{t+1} correspondingly denote the solutions of the optimization problem at t^{th} and $(t+1)^{th}$ iterations.

6.4 Experimental Results

The performance of the designed CMR imaging is evaluated using two different studies. The first study aims to use the proposed CMR imaging to jointly correct for the (1) bias field inhomogeneity and (2) MR noise using the diffusion weighted MR (DW-MR) imaging modality. The second study adds to the first experimnt by taking advantage of the designed CMR imaging to simultaneously compensate for the (1) MR aberrations due to intrinsic properties of the MR scanner, (2) bias field inhomogeneity, as well as (3) MR noise. The performed experiments for each part is explained here with a comprehensive qualitative and quantitative evaluation on the results of each experiment.

6.4.1 First Study: Noise Compensated, Bias-Corrected DW-MR Imaging

In this part, the aim is to use the proposed CMR imaging framework to generate noise compensated, bias-corrected (NCBC) MR images using of endorectal DW-MR images of prostate gland. As explained in Section 6.1, DW-MR imaging is a specific MRI modality which is useful for the aim of tumor detection. Due to this, DW-MR imaging has been established as a promising MR modality for the aim of prostate cancer (PCa) detection. Regarding to the physical properties of DW-MR imaging, using of higher b-values improves the chance of earlier PCa detection as it provides higher image contrast. However, using of higher b-values leads to a significant image SNR reduction which is not desired.

In prostate DW-MR imaging, to overcome the image SNR limitation issue, one typical solution is to use of a specific endorectal MR coil that is placed in the patients rectum. While using of the endorectal coil can significantly boost SNR in DW-MR imaging, one of the drawbacks is that it also introduces significant bias field inhomogeneity in the prostate gland region, especially at the zones closer to the coil. Therefore, there is a need to correct for the bias field inhomogeneity in endorectal DW-MR imaging.

A common challenge faced in bias field inhomogeneity correction methods, particularly when dealing with the significant intensity inhomogeneities exhibited in endorectal DW-MR imaging, is the undesired noise amplification which can have significant negative effects on not only interpretation but also tasks such as segmentation and registration.

Therefore, having a unified computational framework to jointly account for and compensate bias field inhomogeneity and MR noise is highly desired. To this aim, here, the proposed CMR imaging is used to generate noise compensated, bias-corrected (NCBC) MR images from endorectal DW-MR datasets.

6.4.2 DW-MR Imaging Setup

All DW-MR imaging was performed with a 1.5 T MR scanner at Sunnybrook Health Sciences Center, Toronto, ON, Canada and using a typical endorectal receiver coil. All data were obtained under the local institutional research ethics board. All imaging experiments were performed according to a predefined standard imaging protocol with the imaging parameters shown in Table 6.1.

Table 6.1: Endorectal MR imaging protocol

Parameter	Setting
Coil	Medrad®eCoils
TR	10,000 ms
TE	73.6 ms
Resolution	$0.55 \times 0.55 \times 3\ mm^3$
Field Of View(FOV)	14×14cm
b-value	100, 1000 s/mm^2

The performance of the designed CMR imaging in all experiment was compared to the following bias field inhomogeneity correction algorithms which are the state-of-the art methods.

- Level set method (LS) [77]
- Low entropy minimization with a bicubic spline (LEMS) [135]
- Surface coil intensity correction (SCIC) [6]

- Spatial gradient distribution (SGD) [181]
- Bias corrected fuzzy C-means (BCFCM) [2]
- Monte Carlo bias correction (MCBC) [83]

The implementation of all tested methods was performed in MATLAB and tested on an AMD Athlon II X3 3.10 GHz machine with 12 GB of RAM. The implementation code for all tested methods are provided by the author of the corresponding papers. The required parameters of each tested method was set to the best optimal reported values in corresponding papers.

Three different experiments were deigned to evaluate the performance of proposed CMR imaging in producing of NCBC MR images using different endorectal DW-MR images. The designed experiments take advantage of (1) a synthetic endorectal DW-MR phantom (Experiment 1), (2) a physical endorectal DW-MR phantom (Experiment 2), and (3) real patient DW-MR data with endorectal coil at different b-values (Experiment 3). Various quantitative metrics were used to evaluate the results of each performed experiment.

6.4.3 Experiment 1: Synthetic Phantom

A synthetic DW-MR phantom as shown in Fig 6.2(b) was generated with using the explained procedure in [83], where an artificial bias field with a Gaussian intensity decay is introduced into a non-endorectal DW-MR data sample of Fig. 6.2(a).

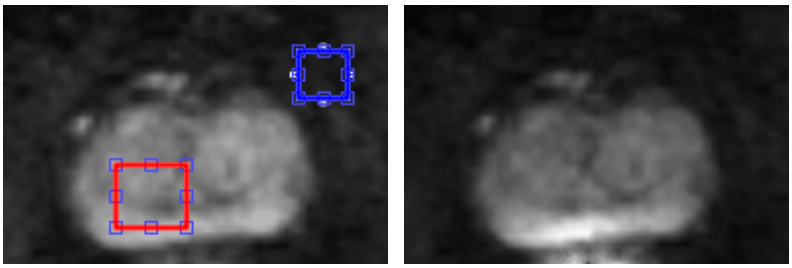

(a) (b)

Figure 6.2: (a) Non-endorectal DW-MR image used to generate the synthetic phantom image in (b) . The red box represents a chosen ROI on the prostate gland and the blue box represents a chosen ROI on the background region. The ROI in red box is used for the SNR calculation. The CNR value is calculated between the red and blue ROIs.

- **Visual Assessment**

  The proposed CMR imaging was used to produce a NCBC MR image using the synthetic phantom of Fig. 6.2(b). For the aim of comparison, a number of state-of-the art bias correction methods were also used to generate bias corrected image from the synthetic phantom of Fig. 6.2(b). The resulted compensated images using all tested methods are shown in Fig. 6.3(c-i). The visual assessment of these images show that employing of the MCBC, LEMS as well as the proposed CMR imaging methods was resulted in the best level of bias field inhomogeneity correction compared to the other tested methods. This is particularly apparent in the peripheral zone (PZ) of the prostate gland as highlighted with the red contours in Fig. 6.3(a-i). Visual comparison of these results show that the intensity inhomogeneities are still present to a significant degree in the produced images using the LS, SCIC, SGD and BCFCM methods, while strong inhomogeneity correction performance is achieved using MCBC, LEMS, and the proposed CMRI imaging.

  To better present the performance of proposed CMR imaging in producing a NCBC synthetic phantom image, the data intensity profiles corresponding to the drawn blue line in Fig. 6.4(a) are shown in Fig. 6.4(b) for the uncorrected MR image (red color plot) versus ground truth image (black color plot) and in Fig. 6.4(c-i) for compensated images using different tested methods (red color plots) versus ground truth image (black color plots). According to the plots of Fig. 6.4, the proposed CMR imaging was resulted in an intensity profile with the most flatness and less amount of variation compared to the intensity profiles related to the compensated images with other tested methods. These results confirm the better performance of proposed CMR imaging in terms of jointly bias field inhomogeneity and MR noise correction using synthetic DW-MR imaging.

- **Quantitative Analysis**

  In order to perform a quantitative analysis of the results using synthetic phantom DW-MR image, a number of metrics including correlation coefficient (r), signal-to-noise ratio (SNR), as well as contrast-to-noise ratio (CNR) were used.

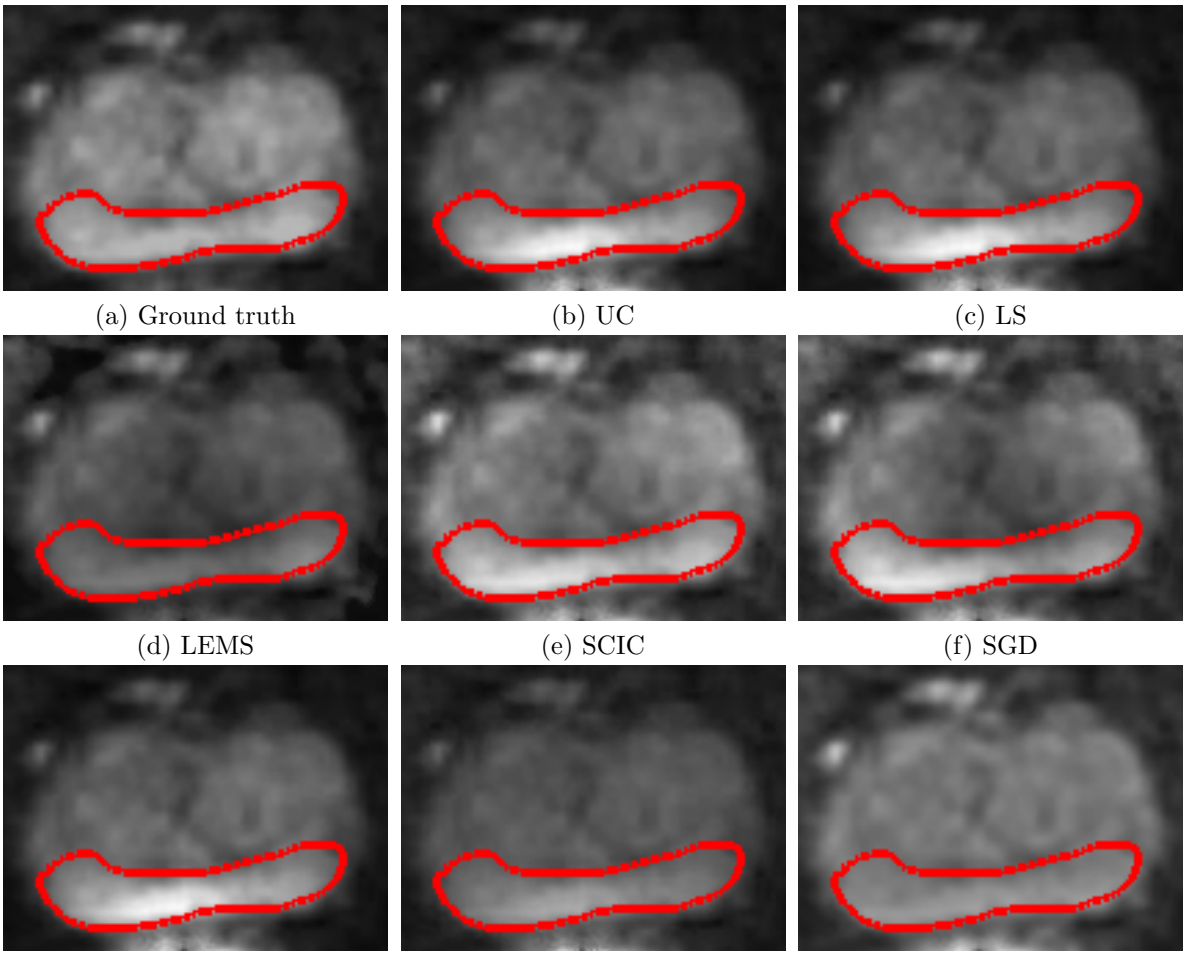

(a) Ground truth (b) UC (c) LS

(d) LEMS (e) SCIC (f) SGD

(g) BCFCM (h) MCBC (i) CMR

Figure 6.3: (a) Non-endorectal DW-MR data (ground truth). (b-i) Compensated synthetic phantom DW-MR images using different tested methods. CMR imaging shows better bias correction compared to the UC-phantom as well as all other tested methods. The red contours show a region of peripheral zone (PZ) of the prostate gland that bias field present to a significant degree in compensated images using LS, SCIC, SGD and BCFCM methods, while strong inhomogeneity correction performance is achieved using MCBC, LEMS, as well as CMR imaging.

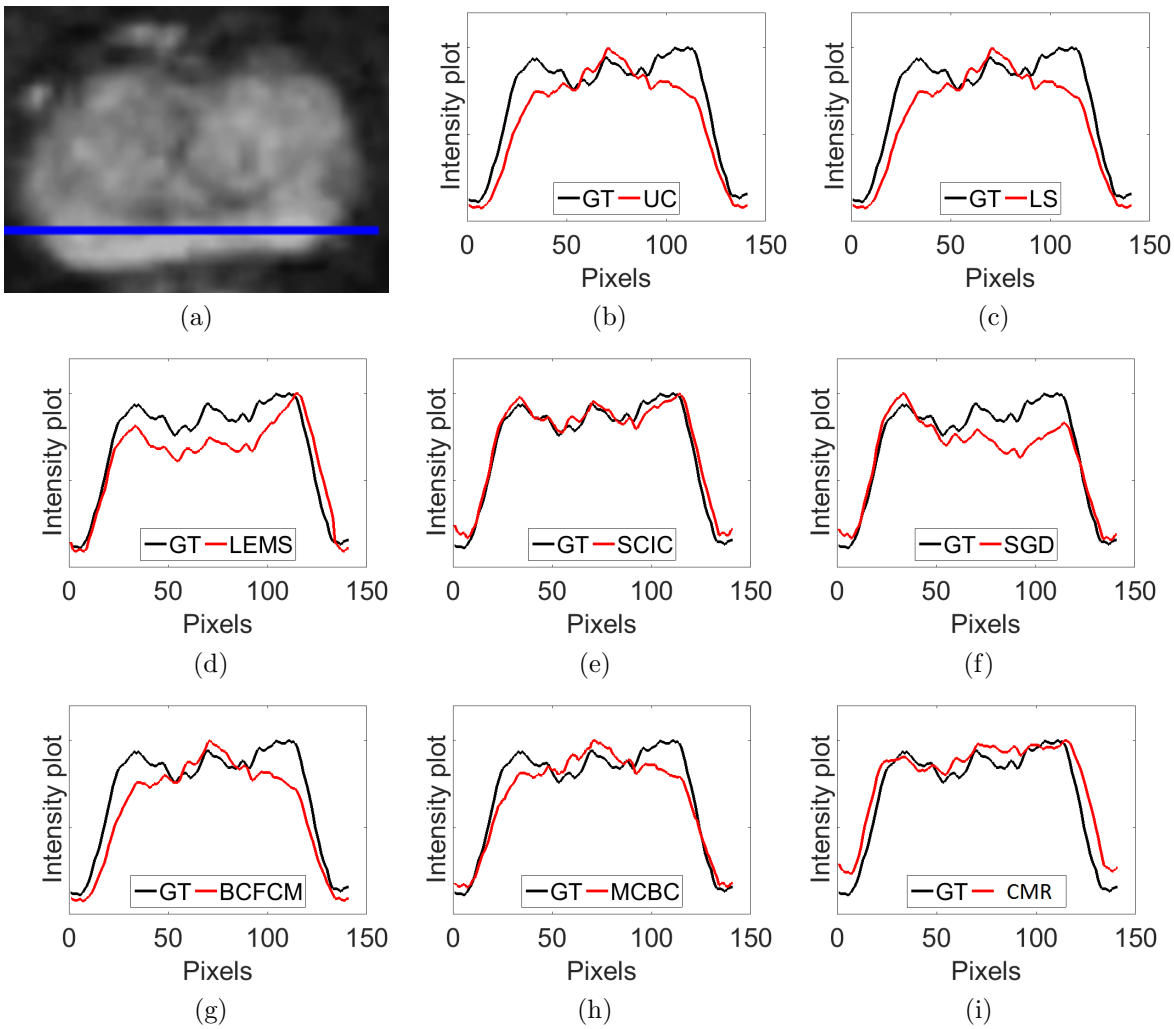

Figure 6.4: (a) Nonendorectal DW-MR image (ground truth). The data intensity profiles corresponding to the blue line in (a) are shown in (b) for uncorrected image (red color plot) versus the ground truth (GT) image (black color plot) and in (c-i) for the compensated images using different methods (red color plots) versus the ground truth image (black color plots). CMR imaging shows the most flat intensity profile with the minimal intensity variation compared to the other tested methods.

The correlation coefficient, r, measures the similarity of two images using the following formulation,

$$r = \frac{\sum_i \sum_j (\gamma_{ij} - \mu_\gamma)(Y_{ij} - \mu_Y)}{\sqrt{(\sum_i \sum_j (\gamma_{ij} - \mu_\gamma)^2)(\sum_i \sum_j (Y_{ij} - \mu_Y)^2)}} \tag{6.10}$$

where μ_γ and μ_Y correspondingly denote the mean values of the true (uncorrupted ground truth) phantom image γ as shown in Fig. 6.2(a) and compensated phantom image Y as shown in Fig. 6.3(c-i). Higher correlation coefficient value ($r = +1$) means better spatial similarity between the ground-truth image and the the compensated image.

Table 6.2: Correlation coefficient, CNR (dB) and SNR (dB) for synthetic phantom experiment. Boldface indicates highest performance.

Method	**Correlation Coefficient (r)**	**CNR (dB)**	**SNR (dB)**
UC	0.8291	20.26	20.15
SCIC	0.8632	20.68	20.76
SGD	0.8620	17.77	19.46
LS	0.8907	20.26	20.25
LEMS	0.8698	21.05	22.90
BCFCM	0.8521	20.32	20.25
MCBC	0.9484	22.49	23.28
CMR	**0.9815**	**23.48**	**25.17**

To quantitatively evaluate the performance of proposed CMR imaging in terms of noise suppression, SNR and CNR metrics were also calculated,

$$SNR = 20 \log \frac{\mu_r}{\sigma_r} \tag{6.11}$$

$$CNR = 20\, log \frac{|\mu_b - \mu_r|}{\sigma_b} \tag{6.12}$$

In the formulation of SNR, μ_r, denotes to the mean of a region of interest (ROI) chosen from the homogeneous regions of prostate gland and σ_r is the standard deviation of that ROI. In CNR formulation, μ_b and μ_r respectively refer to the mean values of chosen ROIs on the background and prostate regions while σ_b represents the standard deviation of

the background region. Better noise suppression should result in higher SNR and CNR values.

The ROI regions that are used for the calculation of SNR and CNR values are shown in Fig. 6.2(a). Here, the red box represents a chosen ROI on the prostate gland and the blue box is a chosen ROI on the background region. The SNR value is calculated for the red ROI in Fig. 6.2(a). The CNR value is calculated between the chosen red and blue ROIs as shown in Fig. 6.2(a).

In this experiment, all calculated correlation coefficient (r), SNR and CNR values are reported in Table 6.2 and for all tested methods. According to the quantitative results of Table 6.2, the proposed CMR imaging achieved the highest correlation coefficient, CNR as well as SNR values compared to the all other tested methods.

6.4.4 Experiment 2: Physical Phantom

In this experiment, a tissue equivalent ultrasound prostate training phantom from Computerized Imaging Reference Systems Inc. (CIRCS Model 053) was used to evaluate the performance of proposed CMR imaging in terms of producing a NCBC DW-MR image with the use of physical phantom DW-MR image. To this aim, DW-MR images were acquired using an MR scanner with the specifications reported in Table 6.1 and with using an endorectal coil. A sample of physical phantom DW-MR image is shown in Fig. 6.5(a).

- **Visual Assessment**

  The proposed CMR imaging was used to produce a NCBC DW-MR image using the physical phantom image that is shown in Fig. 6.5(a). For the aim of comparison, compensated images were also calculated using all other tested methods that are mentioned in the previous experiment. The produced compensated physical phantom DW-MR images using all tested methods are displayed in Fig. 6.5(b-h).

  Similar to the results of the synthetic phantom experiment, it can be observed that the produced NCBC phantom image using the proposed CMR imaging, as shown in Fig. 6.5(h), exhibits the minimal intensity inhomogeneities comparing to the uncorrected phantom image in Fig. 6.5(a) as well as compensated images produced using all other tested methods as shown in Fig. 6.5(b-g). The effect of intensity inhomogeneities correction is particularly noticeable in the regions surrounding the endorectal coil. In addition, it can be observed that the produced NCBC physical phantom image using the CMR imaging approach also exhibit less noise when compared to the compensated images using all other tested methods.

Overall, the visual assessments of the results of this experiment clearly shows the better successfulness of proposed CMR imaging for jointly compensation of DW-MR image degradations due to the bias field inhomogeneity and MR noise. Regarding to this, the proposed CMR imaging is shown useful for the quality enhancement of DW-MR images.

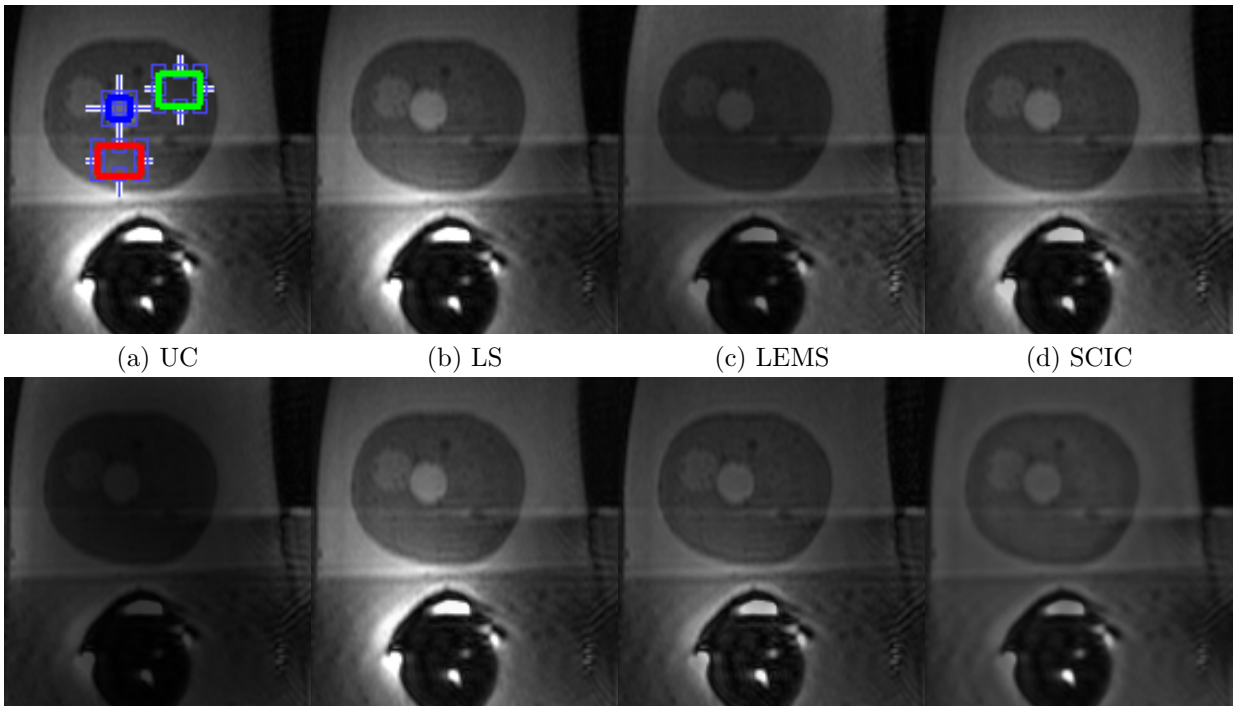

(a) UC (b) LS (c) LEMS (d) SCIC

(e) SGD (f) BCFCM (g) MCBC (h) CMR

Figure 6.5: Proposed CMR imaging shows strong bias field inhomogeneity correction compared to the UC physical phantom image as well as compensated images using other tested methods. Red, blue and green boxes represent different selected ROIs on the prostate gland. The SNR calculation is performed for the ROI inside of the red box. The CNR value is calculated between the ROIs represented by the red box and blue box. Green box represents a selected homogeneous area of physical phantom that is used for CV calculation.

- **Quantitative Analysis**

  In order to perform a quantitative analysis of the results in this experiment, a number of metrics including the coefficient of variation (CV), SNR and CNR were calculated.

The CV was calculated using the following formulation,

$$CV = \frac{\sigma_r}{\mu_r}, \tag{6.13}$$

where, μ_r, represents the mean of a chosen ROI on the homogeneous region of prostate gland and σ_r denotes the standard deviation of that ROI. Better bias field inhomogeneity correction typically should result in lower CV values (less amount of intensity variation) in homogeneous areas, especially at regions closer to the endorectal coil.

To assess the performance of the proposed CMR imaging in terms of MR noise reduction, SNR and CNR values were also calculated using the formulation in Eq. 6.11 and Eq. 6.12, while better noise suppression should result in higher SNR and CNR values.

For the aim of SNR, CNR and CV calculations, several ROIs are chosen as shown on Fig. 6.5(a). Here, the red, blue and green boxes correspondingly represent the selected ROIs on the different areas of prostate gland. The ROI represented by the red box is used for the aim of SNR calculation. The CNR value is calculated between the ROIs represented by the red box and blue box. The green box represents a homogeneous area on the physical phantom that is used for the aim of CV calculation.

Table 6.3: SNR (dB), CNR (dB), and CV values for physical phantom experiment. Boldface indicates highest performance (lower is better for cv).

Method	**SNR (dB)**	**CNR (dB)**	**CV**
UC	22.596	5.910	0.182
SCIC	25.131	13.961	0.108
SGD	22.133	11.183	0.123
LS	22.596	5.910	0.154
LEMS	25.158	10.717	0.085
BCFCM	23.418	8.391	0.136
MCBC	25.508	12.891	0.106
CMR	**32.899**	**15.768**	**0.039**

The calculated SNR, CNR, and CV values for all tested methods in the physical phantom experiment are reported in Table 6.3. As seen using the results of Table 6.3, the proposed CMR imaging achieved the highest SNR and CNR values, and the lowest CV value (lower

indicates better bias correction performance), when compared to that of other tested methods.

6.4.5 Experiment 3: Real DW-MR Data

For this experiment, DW-MR data acquisitions of seven patient cases (four with prostate tumors and three without tumors) were obtained at $b = 100s/mm^2$ and $b = 1000s/mm^2$, totaling to 14 cases. DW-MR scans were collected using a $1.5T$ MR scanner with the DW-MR imaging protocol according to the defined specifications in Table 6.1. All patients underwent MRI as part of clinical indications related to detection or staging of prostate cancer.

- **Visual Assessment**

  Sample slices of produced compensated images using all different tested methods are shown in Fig. 6.6(b-h) and Fig. 6.7(b-h), with images in Fig. 6.6 acquired at b-value=100 s/mm^2 and images in Fig. 6.7 acquired at b-value=1000 s/mm^2.

  From the results of both Fig. 6.6 and Fig. 6.7, it can be observed that while all tested methods could suppress the effect of strong bias field inhomogeneity near the endorectal coil to a certain degree, there remains noticeable residual bias field inhomogeneity in the compensated images produced by all methods except the proposed CMR imaging. In addition, the visual assessment of these results indicates that the proposed CMR imaging was able to provide improved bias field inhomogeneity correction compared to the all other tested methods for both low b-value and high b-value acquisitions, while it suppresses MR noise at the same time. This interpretation is more evident by the improved intensity homogeneity in the prostate region for the NCBC DW-MR image using the proposed CMR imaging. As such, using the proposed CMR imaging could help to improve the overall visualization of different prostate structures compared to the uncorrected DW-MR image in Fig. 6.6(a) and Fig. 6.7(a) as the effective bias field associated with the endorectal coil is greatly suppressed.

  To see the effect of proposed CMR imaging for the aim of tumor visualization, all methods are also tested on the generated apparent diffusion coefficient (ADC) maps for the two patients with prostate tumor. The produced compensated images using ADC maps are shown in Fig. 6.8(b-h) and Fig. 6.9(b-h) for a sample slice from ADC images of two different patients with tumor. From the compensated ADC maps images in these two figures, it can be observed that using the proposed CMR imaging improves the image

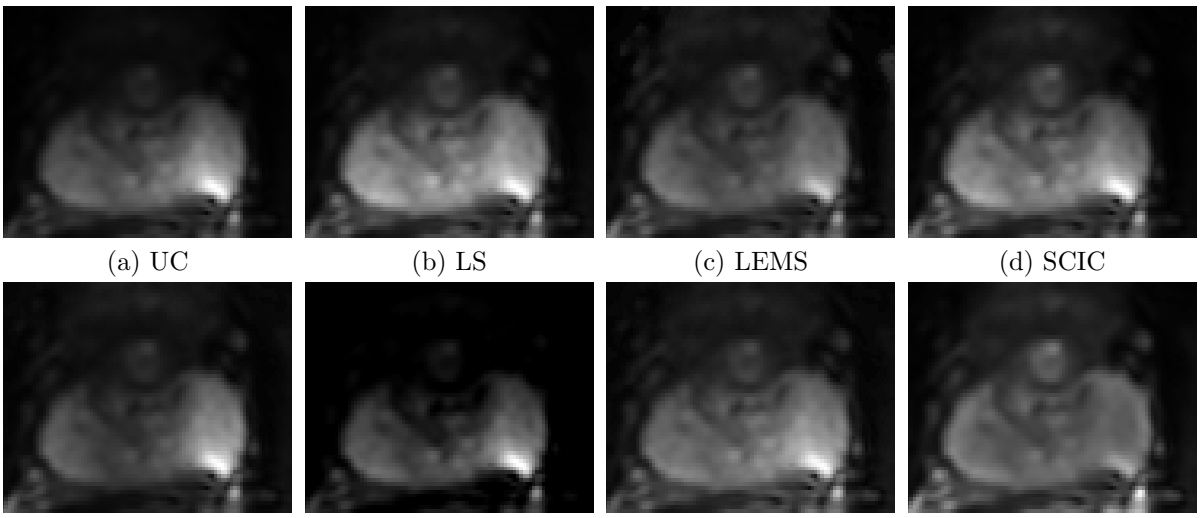

(a) UC (b) LS (c) LEMS (d) SCIC

(e) SGD (f) BCFCM (g) MCBC (h) CMR

Figure 6.6: Case 1 with b=100 s/mm^2. Proposed CMR imaging reduces the bias field and noise in prostate DWI.

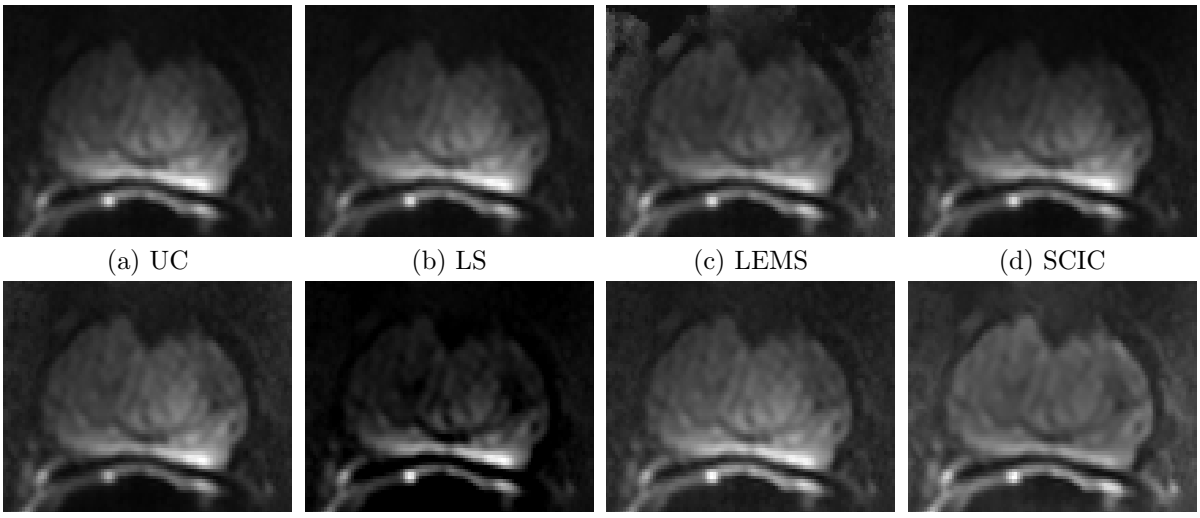

(a) UC (b) LS (c) LEMS (d) SCIC

(e) SGD (f) BCFCM (g) MCBC (h) CMR

Figure 6.7: Case 2 with b=1000 s/mm^2. Proposed CMR imaging reduces the bias field and noise in prostate DWI.

contrast such that facilitates the distinguishing of tumor region from normal tissues. This is helpful for the aim of tumor localization by radiologist or using automatic softwares that are exist for the aim of tumor detection.

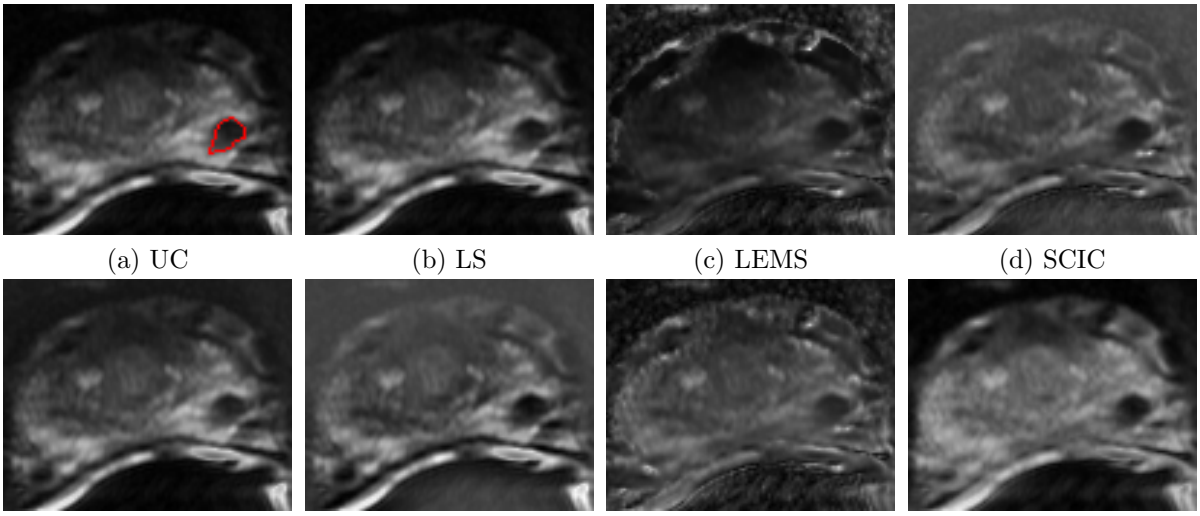

(a) UC (b) LS (c) LEMS (d) SCIC

(e) SGD (f) BCFCM (g) MCBC (h) CMR

Figure 6.8: ADC images for a patient with tumor produced using different tested methods. The tumor location is marked using red contour in (a). Proposed CMR imaging reduces the bias field and noise in prostate DWI such that provides better representation of prostate tumor.

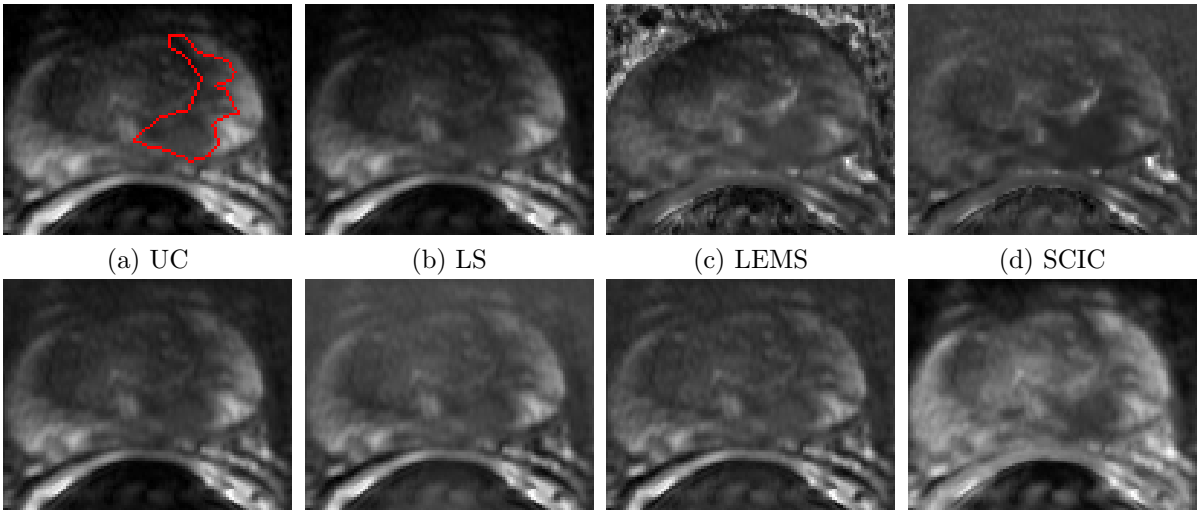

(a) UC (b) LS (c) LEMS (d) SCIC

(e) SGD (f) BCFCM (g) MCBC (h) CMR

Figure 6.9: ADC images for a patient with tumor produced using different tested methods. The tumor location is marked using red contour in (a). Proposed CMR imaging reduces the bias field and noise in prostate DWI such that provides better representation of prostate tumor.

- **Quantitative Analysis**

  In order to quantitatively evaluate the performance of proposed CMR imaging for the case of patient DW-MR imaging, the Fisher Criterion (FC) analysis was performed on all real patient DW-MR data, and using the following formulation,

$$J_{FC} = \frac{|\mu_b - \mu_{ps}|^2}{\sigma_b^2 + \sigma_{ps}^2} \tag{6.14}$$

  where J_{FC} is the FC value, μ_b and μ_{ps} are the mean of background and prostate classes and σ_b and σ_{ps} refer to the variance of background and prostate classes. FC is a valuable metric that is useful for evaluating the power of proposed CMR imaging in improving the delineation of prostate gland and surrounding tissue in compensated DW-MR patient images. Higher FC values means better separation between the prostate gland and surrounding tissue which leads to the easier and more accurate prostate segmentation and tumor localization.

  Another metric that is useful for evaluating the performance of proposed CMR imaging in better delineation of prostate gland and surrounding tissue is the probability of error,

$$P(e) = \int min\left[P(\mathsf{C}_{ps}|m), P(\mathsf{C}_b|m)\right] P(m)dm, \tag{6.15}$$

  which can be calculated by learning a Bayes classifier [125] such that it classifies the DW-MR image, M, to the prostate (C_{ps}) and background (C_b) classes and by assuming a normal distribution for each class of prostate and background. Here, m denotes to the DW-MR data at each pixel. The classifier parameters were learned within a Maximum Likelihood framework. Lower probability of error indicates less overlap between the distribution of prostate and background classes which results in better delineation of prostate gland from surrounding tissue in produced compensated image.

  In Addition, to assess the effectiveness of proposed CMR imaging in noise reduction, SNR (Eq. 6.11) and CNR (Eq. 6.12) values were also calculated for all patient cases. To determine the statistical significance of the results, p-value analysis was also performed for all probability of error, FC, SNR and CNR metrics.

1. **SNR and CNR Analysis**

   The calculated SNR values for all tested methods and for both b-value acquisitions in the real DW-MR data experiment are reported in Table 6.4. As seen in Table 6.4, the proposed CMR imaging achieved the highest SNR values for all acquisitions except one

Table 6.4: SNR (dB) values for real DW-MR data experiment. Boldface indicates highest performance.

Case	UC	SCIC	SGD	LS	LEMS	BCFCM	MCBC	CMR
1	14.7	17.0	19.3	15.3	16.0	13.6	21.0	**22.0**
2	16.7	17.1	16.6	16.6	18.2	15.4	17.5	**21.1**
3	16.2	17.7	14.9	16.8	18.8	13.8	20.6	**21.8**
4	16.3	16.5	15.9	16.4	16.6	15.4	17.6	**17.8**
5	11.7	12.0	12.3	12.0	12.1	9.9	14.1	**17.6**
6	8.9	8.7	8.3	8.7	9.3	5.0	11.1	**13.6**
7	13.6	16.7	18.0	14.2	16.1	12.5	19.8	**20.8**
8	11.1	14.1	13.7	11.6	15.1	10.2	16.9	**17.9**
9	12.4	14.1	13.4	12.4	15.3	11.0	17.0	**19.9**
10	17.1	18.6	18.9	17.5	20.3	15.5	**21.9**	21.3
11	12.5	14.4	12.9	12.9	15.8	6.9	16.3	**18.7**
12	7.6	8.0	7.8	7.7	8.2	3.8	9.8	**13.8**
13	15.1	19.4	15.9	15.1	20.8	11.1	19.1	**25.8**
14	13.4	15.0	15.2	13.7	15.3	8.5	18.4	**19.0**
Ave.	13.4	15.0	14.5	13.6	15.6	10.9	17.2	**19.4**

case and when compared to that of other tested methods, with an average improvement of $6dB$ over the uncorrected DW-MR data.

Likewise, the calculated CNR values for all tested methods and for both b-value acquisitions in the real DW-MR data experiment are reported in Table 6.5. As seen from the results of Table 6.5, the proposed CMR imaging also achieved the highest CNR values in most cases when compared to that of other tested methods, with an average improvement of $5.1dB$. over the uncorrected DW-MR data.

To analyze the statistical significance of the SNR and CNR values, p-values were calculated and reported in Table 6.7. In the p-value analysis, the null assumption was that a given compensation method had no improvement over the SNR or CNR values as compared to the uncorrected DW-MR data. All p-values are computed using a two-tailed normal distribution with a statistical significance level of 0.05.

Table 6.5: CNR (dB) values for real DW-MR data experiment. Boldface indicates highest performance.

Case	UC	SCIC	LS	LEMS	SGD	BCFCM	MCBC	CMR
1	11.5	12.5	13.1	11.8	11.2	11.0	15.0	**15.8**
2	12.1	12.3	12.1	12.2	10.9	11.9	12.5	**17.3**
3	15.8	16.9	11.1	16.1	4.5	15.3	18.5	**20.7**
4	21.0	21.6	21.1	21.4	21.2	21.1	21.2	**24.3**
5	11.7	13.2	11.5	11.9	5.0	11.3	14.1	**20.6**
6	13.0	13.4	11.7	13.1	12.6	11.5	11.8	**16.1**
7	13.2	13.9	14.9	13.4	12.9	12.6	17.5	**17.9**
8	17.2	**21.0**	19.7	17.6	16.7	17.9	18.3	18.2
9	15.9	18.9	16.9	15.9	19.9	16.5	16.0	**24.7**
10	23.5	25.3	24.8	23.6	26.9	22.8	**26.1**	24.4
11	14.0	16.1	13.3	14.4	17.2	10.4	17.0	**19.9**
12	12.1	12.5	11.6	12.1	12.2	10.4	14.5	**23.8**
13	12.2	13.2	12.0	12.4	13.0	9.2	15.3	**16.7**
14	15.7	17.3	17.6	15.8	16.8	13.0	19.1	**19.3**
Ave.	14.9	16.3	15.1	15.1	14.4	13.9	16.9	**20.0**

The p-values for the SNR analysis demonstrate the statistical significance of all methods in SNR improvement, with the lowest p-value obtained for the proposed CMR imaging. Furthermore, the calculated p-values based on the CNR analysis shows that the proposed CMR imaging had the lowest p-value among all tested methods and is demonstrated to be statistically significant. The CNR p-value results also show the statistical significance of all tested methods except SGD and LS methods which resulted in p-values more than 0.05.

To evaluate the effectiveness of proposed CMR imaging in terms of improving the visualization of prostate tumor, CNR values between the tumor and normal tissue is also calculated using ADC map images for the 2 patients with prostate tumor. Calculated CNR values are reported in Table 6.6 when the proposed CMR imaging achieved the highest CNR values for both patient cases and compared to that of other tested methods

as well as UC image.

Table 6.6: CNR (dB) between tumor and normal tissue calculated using ADC images. Boldface indicates highest performance.

Case	UC	SCIC	LS	LEMS	SGD	BCFCM	MCBC	CMR
1	22.5	18.2	21.8	12.8	22.7	20.1	18.2	**24.8**
2	19.6	22.2	19.6	10.4	18.7	22.0	19.2	**27.3**

Table 6.7: Calculated p-values for the probability of error, SNR, CNR, and FC analysis using different tested methods.

P-Value	Probability of Error	SNR	CNR	FC
SCIC	8.81E − 013	5.07E − 04	2.48E − 04	1.6E − 02
SGD	1.3E − 07	1.76E − 04	6.10E − 01	1.45E − 01
LS	4.90E − 14	3.1E − 02	7.17E − 01	2.18E − 02
LEMS	2.95E − 010	5.12E − 03	1.15E − 04	8.56E − 03
BCFCM	4.1E − 017	2.18E − 06	5.04E − 04	4.36E − 04
MCBC	1.77E − 012	7.3E − 05	1.43E − 02	4.2E − 02
CMR	**6.15E − 019**	**7.85E − 08**	**3.02E − 05**	**1.41E − 04**

2. **Fisher Criterion**

   To assess the performance of proposed CMR imaging in terms of achieving separability of the prostate gland from the surrounding tissue, FC analysis (Eq. 6.14) was performed on all 14 acquisitions and for all different tested methods. The FC results are reported in Table 6.8 showed that the proposed CMR imaging achieved the highest overall FC results for the most cases, followed by MCBC and SCIC. All other tested methods except BCFCM also demonstrated improvements in FC when compared to the uncorrected DW-MR data, but to a much lesser degree than the proposed CMR imaging. The p-value analysis was also performed to evaluate the statistical significance of acquired FC values. The calculated p-values are reported in Table 6.7, with the smallest p-value achieved using the proposed CMR imaging.

Table 6.8: Fisher criterion (FC) values for real DW-MR data experiment. Boldface indicates highest performance.

Case	UC	SCIC	SGD	LS	LEMS	BCFCM	MCBC	CMR
1	0.94	1.29	1.68	1.00	0.66	0.98	4.25	**7.86**
2	1.08	**1.23**	0.95	1.10	0.94	0.79	1.03	1.05
3	0.72	1.27	0.66	0.83	1.48	0.71	3.55	**5.31**
4	2.29	7.80	4.18	2.76	3.22	2.20	8.36	**10.76**
5	1.63	1.89	2.02	1.77	1.87	1.37	2.55	**3.89**
6	1.74	4.46	1.59	2.21	2.36	1.62	3.55	**7.35**
7	0.81	1.07	1.32	0.86	0.91	0.78	2.74	**5.59**
8	1.02	1.64	1.61	1.10	1.56	1.02	1.71	**3.77**
9	0.81	1.11	1.00	0.81	2.11	0.88	1.50	**3.29**
10	5.65	8.06	8.47	5.65	12.20	5.90	6.64	**16.39**
11	1.80	2.89	2.01	1.96	4.42	0.92	6.49	**9.87**
12	1.00	1.14	1.05	1.02	1.16	0.55	**5.37**	2.48
13	1.02	1.29	1.13	1.08	0.99	0.50	**4.65**	3.82
14	2.53	3.45	3.56	2.67	0.41	1.14	3.13	**4.02**
Ave.	1.64	2.76	2.23	1.77	2.45	1.38	3.96	**6.10**

3. **Probability of Error**

   A Bayes classifier was trained to classify all datasets to prostate and background classes, and the probability of error classification was calculated and reported in Table 6.9. According to the probability of error results, the proposed CMR imaging results in the best separation between the prostate gland from surrounding tissue as the calculated probability of error was considerably lower compared to the other tested methods. These results also demonstrate that the MCBC and SCIC methods were the next two successful methods in terms of prostate classification, while the other tested approaches except BCFCM could also decrease the probability of error classification but to a much lesser extent. In general, these results agree well with the conclusions drawn from the FC analysis.

Table 6.9: Probability of error for real DW-MR data experiment. Boldface indicates highest performance.

Case	UC	SCIC	SGD	LS	LEMS	BCFCM	MCBC	CMR
1	0.090	0.049	0.065	0.079	0.065	0.146	0.024	**0.011**
2	0.089	0.049	0.066	0.079	0.066	0.146	0.025	**0.011**
3	0.103	0.058	0.072	0.090	0.071	0.140	0.031	**0.013**
4	0.089	0.048	0.063	0.077	0.063	0.141	0.025	**0.012**
5	0.092	0.053	0.069	0.083	0.067	0.148	0.027	**0.012**
6	0.099	0.057	0.076	0.087	0.072	0.157	0.029	**0.013**
7	0.091	0.052	0.070	0.080	0.072	0.149	0.027	**0.012**
8	0.093	0.039	0.071	0.086	0.043	0.164	0.020	**0.009**
9	0.093	0.038	0.071	0.086	0.043	0.156	0.019	**0.007**
10	0.092	0.040	0.067	0.084	0.041	0.147	0.019	**0.010**
11	0.093	0.041	0.068	0.087	0.042	0.158	0.020	**0.010**
12	0.096	0.042	0.073	0.088	0.043	0.157	0.020	**0.010**
13	0.093	0.044	0.072	0.085	0.040	0.162	0.020	**0.011**
14	0.097	0.045	0.075	0.088	0.044	0.168	0.022	**0.010**
Ave.	0.094	0.047	0.070	0.084	0.055	0.153	0.023	**0.011**

4. **Computational Performance Analysis**

   All tested methods were implemented using MATLAB and C++ code and tested on an AMD Athlon II X3 3.10 GHz machine with 12GB of RAM. The computation time of each method was calculated and reported in Table 6.10. As the timing process results show, the SCIC method had the lowest average computation time of 0.142 seconds, with the LEMS method having the highest average computation time of 76.448 seconds. The proposed CMR imaging, where one should note that the underlying implementation has not been optimized, has an average computation time of 14.424 seconds.

Table 6.10: Computation times for all tested methods.

Case	SCIC	SGD	LS	LEMS	BCFCM	MCBC	CMR
1	**0.123**	1.023	11.640	75.261	56.171	4.231	14.651
2	**0.156**	1.058	10.230	72.112	50.231	3.651	14.681
3	**0.114**	1.121	11.030	74.112	53.987	2.311	15.312
4	**0.132**	1.103	10.280	70.123	50.123	4.711	14.985
5	**0.113**	1.210	11.220	80.123	60.101	4.231	15.231
6	**0.145**	1.350	11.050	82.123	55.411	4.511	14.007
7	**0.192**	1.010	10.390	79.235	53.112	4.326	13.987
8	**0.125**	1.192	12.350	78.123	52.114	4.789	14.055
9	**0.112**	1.230	11.087	52.311	45.321	3.965	13.256
10	**0.113**	1.021	10.982	85.123	51.111	5.311	14.521
11	**0.156**	1.052	11.140	89.156	50.123	4.120	14.008
12	**0.204**	1.032	11.380	69.235	52.123	4.155	13.251
13	**0.182**	1.024	12.010	93.112	57.564	4.369	15.011
14	**0.127**	1.056	10.235	70.120	60.231	4.659	14.978
Ave.	**0.142**	1.106	11.073	76.448	53.409	4.239	14.424

6.4.6 Second Study: Full Compensated Magnetic Resonance Imaging

In this part, the aim is to present the results of the proposed CMR imaging framework for jointly compensating for the effect of (1) MR aberrations due to intrinsic properties of MR scanner, (2) bias field inhomogeneity, as well as (3) inherent MR noise within a unified computational framework.

In order to perform CMR imaging in this experiment, the intrinsic properties of the utilized MR scanner (MR PSF) should be characterized. To this aim, a calibration procedure [128] was performed on a standard prostate training phantom (CIRCS Model 053) that is shown in Fig. 6.10(a). The calibration procedure takes advantage of some prior knowledge on the phantom (e.g., edges and homogeneous regions) and leverage that to learn the intrinsic properties of the MR scanner. With incorporating of the learned MR PSF to the modeling of MR compensation function, $\mathbb{C}$, the proposed CMR imaging was performed to calculate compensated MR images using different MR modalities.

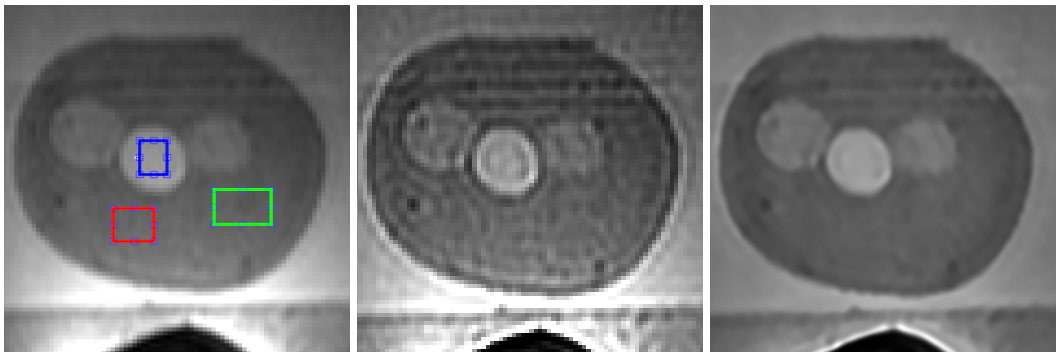

(a) UC (b) BDC (c) CMR

Figure 6.10: CMR imaging results using training MR phantom. (a) A slice of uncorrected (UC) prostate training phantom from Computerized Imaging Reference Systems Inc. Compensated MR phantom images using (b) BDC method, (c) CMR imaging.

To test the efficacy of proposed CMR imaging in producing compensated images with less aberrations, bias field inhomogeneity and noise, several experiments were performed using: (1) MR images acquired from a prostate training phantom (CIRCSMODEL 053), (2) T2 weighted (T2w) MR images of prostate gland, and (3) DW-MR images of prostate gland. All Human MR imaging was performed using a 1.5 T MR scanner at Sunnybrook Health Sciences Center Toronto, Canada and according to the institutional research ethics board while all imaging parameters were set according to the information of Table 6.11.

Table 6.11: Imaging parameters for T2w and DW-MR imaging.

Modality	DFOV (cm^2)	Resolution (mm^3)	TE (ms)	TR (ms)
T2W	22×22	$0.49 \times 0.49 \times 3$	110	4,687
DWI	20×20	$1.56 \times 1.56 \times 3$	61	6,178

- **Qualitative Analysis**

  In the first experiment, the proposed CMR Imaging was utilized to generate a compensated MR image using a standard MR prostate phantom as shown in Fig. 6.10(a) while the compensated phantom image produced using the proposed CMR imaging is shown in Fig. 6.10(c). For aim of comparison, compensated phantom image using the conventional blind deconvolution compensation (BDC) method [27] is also calculated as the state-of-the-art and shown in Fig. 6.10(b).

  Visual comparison of these results shows less bias intensity variation for the compensated phantom image generated by the proposed CMR Imaging and compared to the both uncorrected (UC) phantom image as well as compensated phantom image using tested BDC method. This visual assessment demonstrate the successfulness of the proposed CMR Imaging for the bias field inhomogeneity correction. Furthermore, employing the proposed CMR imaging could improve the sharpness of the phantom image compared to the tested BDC method and due to the effective compensation of MR aberrations that blur the MR image. In addition, this result shows the effectiveness of the proposed CMR Imaging for MR noise suppression such that the homogeneous regions of the MR phantom image are shown smoother in compensated phantom image produced with proposed CMR imaging while the noise is amplified in the compensated image produced using the tested BDC method.

  In the second and third experiments, the proposed CMR imaging and BDC method were used to generate compensated MR images from different samples of DW-MR prostate images as well as samples of T2w prostate images. The produced compensated MR images using each method are respectively shown in Fig. 6.11 and Fig. 6.12 for two different sample slices of DW-MR images and T2w MR images.

  As the results of Fig. 6.11(c,i) and Fig. 6.12(c,i) show, bias field inhomogeneities reduced in compensated MR images of both modalities such that the delineation between prostate gland and surrounding tissue improved. To better visualize the bias correction results, highly bias inhomogeneity affected areas of each image were chosen as marked

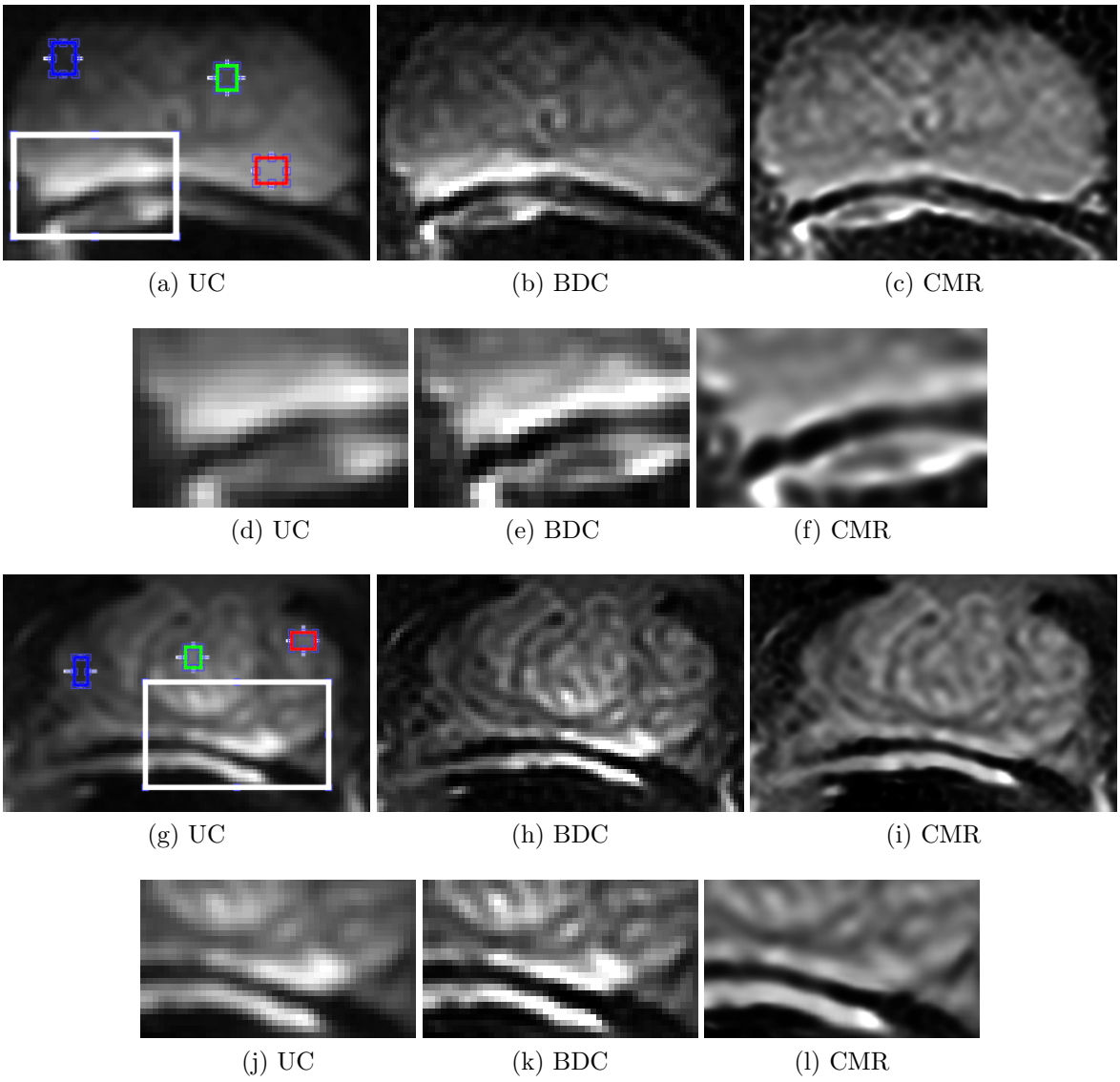

(a) UC (b) BDC (c) CMR

(d) UC (e) BDC (f) CMR

(g) UC (h) BDC (i) CMR

(j) UC (k) BDC (l) CMR

Figure 6.11: DW-MR slices of prostate gland (a,g). Compensated DW-MR images using (b,h) BDC method and (c,i) proposed CMR imaging. (d-f) and (j-l) are zoomed regions marked with white boxes on uncorrected (UC) DW-MR images of (a) and (g).

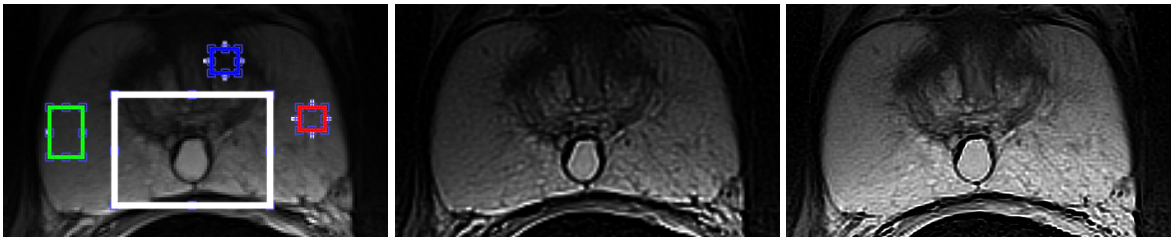

(a) UC (b) BDC (c) CMR

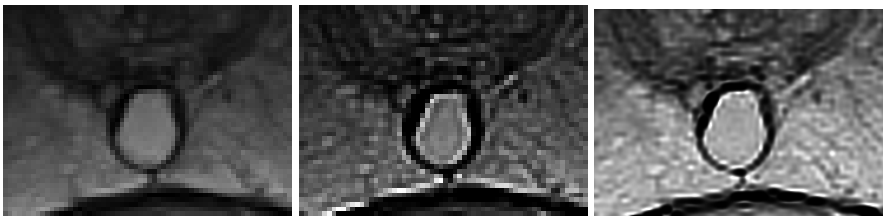

(d) UC (e) BDC (f) CMR

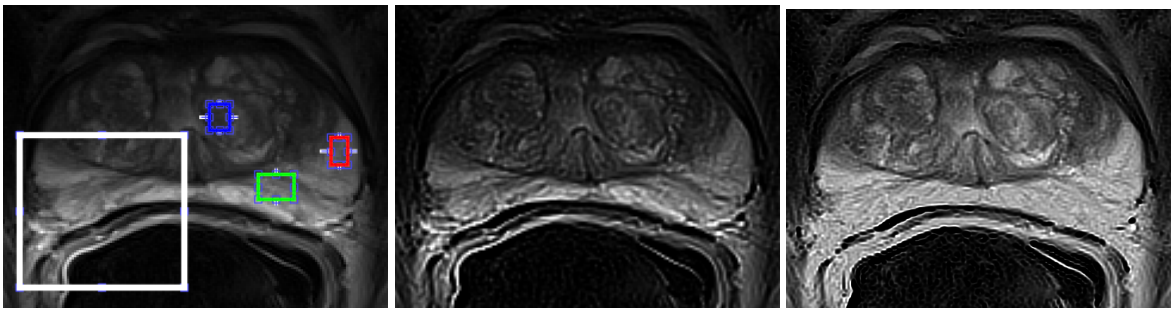

(g) UC (h) BDC (i) CMR

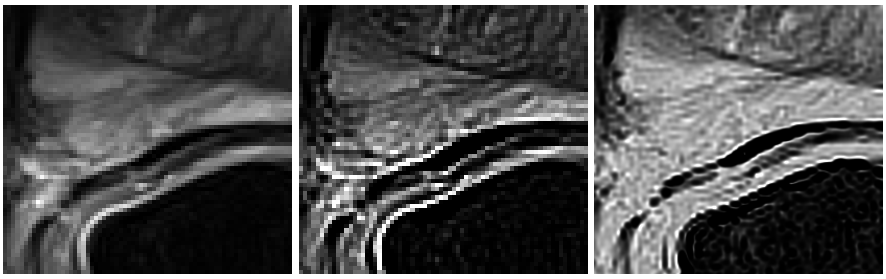

(j) UC (k) BDC (l) CMR

Figure 6.12: CMR imaging results using T2w-MR images.T2w-MR slices of prostate gland (a,g). Compensated T2w using (b,h) BDC method and (c,i) proposed CMR imaging. (d-f) and (j-l) are zoomed regions marked with white boxes on uncorrected (UC) T2w-MR images of (a) and (g).

with the white boxes in Fig. 6.11(a,g) and Fig. 6.12(a,g) and correspondingly displayed in Fig. 6.11(d-f, j-l) and Fig. 6.12(d-f, j-l). As can be seen from the displayed zoomed in regions, compensated MR images using proposed CMR imaging show much less bias inhomogeneities compared to the both uncorrected MR images and compensated MR images using tested BDC method such that provide a more uniform intensity variations for the homogeneous regions of prostate tissue. These results demonstrate the better performance of proposed CMR imaging in terms of bias inhomogeneities correction.

Here, again, comparing of the compensated images produced using BDC method as shown in Fig. 6.11(b,h) and Fig. 6.12(b,h) to the produced compensated images using proposed CMR imaging as shown in Fig. 6.11(c,i) and Fig. 6.12(c,i) clearly demonstrates the better performance of the proposed CMR imaging in terms of jointly correcting for the aberrations due to the bias field inhomogeneity as well as aberrations due to the effect of MR scanner such that the overall image contrast is increased. Due to this, all compensated MR images using proposed CMR imaging look sharper compared to the corresponding uncorrected MR images of Fig. 6.11(a,g) and Fig. 6.12(a,g) and hence, provide a better visualization of different details and structures of the tissue.

To provide a better qualitative evaluation of the results, a highly structured region of prostate tissue was chosen from each DW-MR and T2w-MR images as marked with white boxes on uncorrected (UC) images in Fig. 6.11(a,g) and Fig. 6.12(a,g). The zoomed-in version of these chosen areas are shown in Fig. 6.11(d-f, j-l) and Fig. 6.12(d-f, j-l). Considering these zoomed-in regions show the overall better performance of proposed CMR imaging in terms of jointly aberration correction and noise suppression using different MR imaging modalities. Due to this, compensated images generated using the proposed CMR imaging show a better image contrast and less noise such that the different details and fine structures of the prostate tissue can be better represented and visualized using these images.

- **Quantitative Analysis**

  In order to quantitatively evaluate the efficacy of proposed CMR imaging for producing compensated MR images using different MR image modalities, various metrics including SNR (Eq. 6.11), CNR (Eq. 6.12) as well as CV (Eq. 6.13) were used. Sample of chosen ROIs for calculating of each SNR, CNR and CV values are shown in all Fig. 6.10(a), Fig. 6.11(a) and Fig. 6.12(a) and with the red, blue and green boxes. Here, the ROI inside the red box was used for the aim of SNR calculation, CNR was calculated between the ROIs in red and blue boxes and CV was calculated suing the ROI inside the green box. To perform the quantitative analysis on the results of each image modality, 14 different slices from different patients were used to generate compensated MR images using both

BDC method and CMR imaging and the results were used to calculate the SNR, CNR and CV metrics. The average values for all calculated SNR, CNR and CV metrics are reported in Table 6.12.

Table 6.12: SNR (dB), CNR (dB) and CV for uncorrected MR images and compensated MR images using tested BDC method and proposed CMR imaging.

	SNR (dB)	CNR (dB)	CV
Baseline Phantom	23.29	13.48	0.06
BDC Phantom	19.48	10.05	0.1
CMR Phantom	**29.07**	**18.93**	**0.03**
DWI	21.24	13.91	0.08
BDC DWI	15.48	15.17	0.16
CMR DWI	**25.92**	**25.91**	**0.05**
T2W	13.09	7.32	0.22
BDC T2w	12.33	9.14	0.24
CMR T2w	**18.70**	**13.77**	**0.11**

In overall, the quantitative results of Table. 6.12 shows better SNR and CNR values for the computed CMR images using proposed CMR imaging and for all three performed experiments using the phantom MR images, DW-MR images as well as T2w-MR images. An average SNR improvement of $\sim 6dB$ was obtained for all three performed experiments and compared to the uncorrected MR images. Based on the reported SNR values in Table 6.12, using of tested BDC method was resulted in a SNR reduction compared to the uncorrected MR images in all three performed experiments which shows the weakness of the BDC method in terms of MR noise suppression.

The quantitative results of Table 6.12 also demonstrate that the proposed CMR imaging was resulted in an average CNR improvement of $\sim 8dB$ for all three performed experiments and compared to the uncorrected MR images while the tested BDC method could also increase the CNR values for both experiments using DW-MR images and T2w-MR images and compared to the uncorrected MR images but to a much lesser extent.

Furthermore, the results of CV calculations also confirm the successfulness of proposed

CMR imaging in terms of noise reduction such that on average, CV reduced about ~ 0.07 for the compensated images produced using the proposed CMR imaging while the CV values were increased for all compensated MR images produced using the tested BDC method.

6.5 Summary

A novel compensated magnetic resonance (CMR) imaging is developed to generate compensated MR images with higher overall quality. The developed CMR imaging was set to jointly correct for the different MR imaging degradation factors including MR aberrations due to the intrinsic properties of the utilized MR scanner or the one which are caused by the bias field inhomogeneity plus MR noise and using a unified computational framework. Evaluation of the proposed CMR imaging using different MR imaging modalities in various experiments proved that the proposed CMR imaging is a useful computational approach for the quality enhancement of MR imaging. The proposed CMR imaging can be modified in the future works to incorporate for the other types of MR degradations and to more improve the quality of MR imaging within a purely computational image compensation framework. This could be helpful for the quality enhancement of MR imaging that is required for the better interpretation and diagnosis of MR images by both radiologists and automatic MR processing softwares.

Chapter 7

Conclusions

This thesis dissertation proposes a novel and unified computational framework for compensated medical imaging intended to enhance the overall quality of medical images acquired with different imaging modalities such as MRI and OCT that is desired for many of clinical applications. The proposed computational compensated medical imaging framework provides a general probabilistic model that can be applied to different types of medical imaging techniques to correct for a variety of different degradation issues which are unavoidable in imaging of an issue/organ. Incorporation of the new proposed SFC-CRF model to the formulation of proposed compensated imaging framework makes it possible to include different sort of structural information about the tissue/organ to the framework of compensated imaging. This improves the performance of the proposed computational compensated imaging framework in producing of a true compensated image. A summary of the main thesis contributions is provided as follows along with a future research direction for the proposed work.

7.1 Summary of Thesis Contributions

- In Chapter 3, a novel and general computational cross-domain compensated medical imaging framework is proposed that can be used for producing of a compensated medical image by jointly correcting for multiple different acquisition/reconstruction degradation issues that always arise in using of various types of medical imaging.

- In chapter 4, the proposed probabilistic cross-domain compensated medical imaging framework is used to develop a C-OCT imaging framework which is shown useful for

the quality enhancement of OCT imaging. The developed C-OCT imaging jointly compensates for the effects of optical aberrations and speckle noise issues in OCT imaging and hence generates OCT images with better overall contrast. The developed C-OCT imaging can be used with different types of OCT configurations such as FD-OCT and SS-OCT.

- In chapter 5, a C-SR-OCT imaging framework is developed with the use of probabilistic computational cross-domain compensated medical imaging framework that is proposed in Chapter 3. The designed C-SR-OCT imaging takes advantage of multiple OCT acquisitions to produce a SR-OCT image of higher quality within the framework of proposed cross-domain compensated medical imaging. To this aim, the developed C-SR-OCT imaging jointly corrects for the optical aberration issue, motion artifact and speckle noise which all together destroy the quality of acquired OCT images. The performance of the developed C-SR-OCT imaging is tested using different real and simulated OCT data and is generally shown useful for the quality enhancement of OCT imaging.

- In Chapter 6, a CMR imaging is designed within the framework of proposed computational cross-domain compensated medical imaging that is proposed in Chapter 3. The designed CMR imaging jointly compensate for MR image degradations due to the noise, MR aberrations and bias field inhomogeneities as all accounted in a unified computational compensation framework. The developed CMR imaging is shown useful for improving the overall quality of MR imaging form different MR modalities.

7.2 Future Research

The proposed computational compensated imaging framework in this dissertation provides a foundation for the future research in compensated medical imaging. This work motivates future research in the following directions.

1. All different types of medical imaging techniques suffer from a degradation due to the effect of imaging system itself which partly originates from the effect of system characteristic function. In this work, we only focused on the OCT and MR imaging techniques to perform the system characteristic function compensation using the proposed compensation framework. The computational compensated imaging framework that is proposed in this work provides a general model that can be used for the aim compensating for the effect of system characteristic function in different types of

medical imaging techniques. One general future direction of this work is to apply the proposed compensation framework to the other types of medical imaging techniques such as ultrasound, positron emission tomography and microscopy imaging and for the aim of compensating for the degradations due to the effect of imaging system characteristic function.

2. The computational compensated imaging framework that is proposed in this work is designed in a Bayesian type reconstruction framework which takes advantage of SFC-CRF modeling to find the best estimate of a desired compensated image. Therefore, the overall performance of the proposed compensation framework highly depends on the designing of both unary and potential functions that are incorporated in the MAP framework. One important future direction of this work is to work on designing of new types of unary and pairwise potential functions that can account for different types of degradation issues in various types of medical imaging systems. Particularly, this stream of research can be expanded as two parts,

    - The unary potential function (data fidelity term) of the proposed compensated imaging framework can be modified to account for other types of image degradations that may happen with the use of various types of medical imaging systems. For example, in OCT imaging, the dispersion compensation can be incorporated to the C-OCT imaging framework by designing a proper unary function.
    - In the proposed compensated imaging framework, the incorporated pairwise potential function takes advantage of a fully-connected clique structure to model the data observation and inference interactions. The pairwise potential function can be expanded by taking advantage of other stochastic clique structures such as hierarchical clique structures and deep fully connected clique structures that can be useful for improving the performance of the whole compensation model in dealing with other types of possible degradation issues in different medical imaging techniques. Furthermore, other types of pairwise potential functions can be designed to improve the functionality of compensated medical imaging framework in handling of different types of reconstruction image degradations. For example, in MR imaging the pairwise potential function can be designed to compensate for the Gibss artifact that happens due to the insufficient k-space sampling in MR imaging.

3. As another direction for the future work, the developed super resolution based compensation model that takes advantage of the proposed probabilistic compensated

imaging framework can be used as an efficient compounding method for the quality enhancement of various types of medical imaging such as MRI and microscopy. Using of such a SR medical image compensation framework can be particularly beneficial for the aim of motion artifact compensation which is one major problem in working with different medical imaging techniques. Taking advantage of such a super resolution based compensation model can be a proper foundation for developing of spatial-temporal computational compensation methods which is useful for jointly correction of spatio/temporal degradation issues that may experienced in working with different types of medical imaging techniques.

References

[1] Steven G Adie, Benedikt W Graf, Adeel Ahmad, P Scott Carney, and Stephen A Boppart. Computational adaptive optics for broadband optical interferometric tomography of biological tissue. *Proceedings of the National Academy of Sciences*, 109(19):7175–7180, 2012.

[2] Mohamed N Ahmed, Sameh M Yamany, Nevin Mohamed, Aly A Farag, and Thomas Moriarty. A modified fuzzy C-means algorithm for bias field estimation and segmentation of MRI data. *Medical Imaging, IEEE Transactions on*, 21(3):193–199, 2002.

[3] Avni C Akcay, Kye Lee, and Jannick P Rolland. Dispersion manipulation in optical coherence tomography with fourier-domain optical delay line. In *Biomedical Optics 2005*, pages 512–522. International Society for Optics and Photonics, 2005.

[4] Zohair Al-Ameen, Ghazali Sulong, Md Gapar Md Johar, Neha Verma, Rakesh Kumar, M Dachyar, M Alkhawlani, A Mohsen, H Singh, Sarabjeet Singh, et al. A comprehensive study on fast image deblurring techniques. *International Journal of Advanced Science and Technology*, 44, 2012.

[5] Yaozu An, Yao Lu, and Zhengang Zhai. Spatially varying regularization of image sequences super-resolution. In *Computer Vision–ACCV 2009*, pages 475–484. Springer, 2009.

[6] Gopal B Avinash. Method for correcting inhomogeneity of spatial intensity in an acquired MR image, August 24 1999. US Patent 5,943,433.

[7] Pranjal Awasthi, Aakanksha Gagrani, and Balaraman Ravindran. Image modeling using tree structured conditional random fields. In *IJCAI*, pages 2060–2065, 2007.

[8] GR Ayers and J Christopher Dainty. Iterative blind deconvolution method and its applications. *Optics letters*, 13(7):547–549, 1988.

[9] Tuncer C Aysal and Kenneth E Barner. Rayleigh-maximum-likelihood filtering for speckle reduction of ultrasound images. *Medical Imaging, IEEE Transactions on*, 26(5):712–727, 2007.

[10] Ramy M Bahy, Gouda I Salama, and Tarek A Mahmoud. Adaptive regularization-based super resolution reconstruction technique for multi-focus low-resolution images. *Signal Processing*, 103:155–167, 2014.

[11] Sajjad Hussain Baloch, Erkang Cheng, Tong Fang, and Ying Zhu. Shape based conditional random fields for segmenting intracranial aneurysms, September 9 2014. US Patent 8,831,308.

[12] Marco Bevilacqua. *Algorithms for super-resolution of images and videos based on learning methods*. PhD thesis, Université Rennes 1, 2014.

[13] Chetan Bhole, Nicholas Morsillo, and Christopher J Pal. 3d segmentation in ct imagery with conditional random fields and histograms of oriented gradients. In *MLMI*, pages 326–334. Springer, 2011.

[14] Ameneh Boroomand, Alexander Wong, Edward Li, Daniel S Cho, Betty Ni, and Kostandinka Bizheva. Multi-penalty conditional random field approach to super-resolved reconstruction of optical coherence tomography images. *Biomedical optics express*, 4(10):2032–2050, 2013.

[15] Alexandre Bousse, Ottavia Bertolli, David Atkinson, Simon Arridge, Sebastien Ourselin, Brian Hutton, and Kris Thielemans. Maximum-likelihood joint image reconstruction/motion estimation in attenuation-corrected respiratory gated pet/ct using a single attenuation map. 2015.

[16] Bernhard Brendel, Maximilian von Teuffenbach, Peter B Noël, Franz Pfeiffer, and Thomas Koehler. Penalized maximum likelihood reconstruction for x-ray differential phase-contrast tomography. *Medical physics*, 43(1):188–194, 2016.

[17] Robert W Brown, Y-C Norman Cheng, E Mark Haacke, Michael R Thompson, and Ramesh Venkatesan. *Magnetic resonance imaging: physical principles and sequence design*. John Wiley & Sons, 2014.

[18] D Calvetti, S Morigi, L Reichel, and F Sgallari. Tikhonov regularization and the l-curve for large discrete ill-posed problems. *Journal of computational and applied mathematics*, 123(1):423–446, 2000.

[19] Neill Campbell, Kartic Subr, and Jan Kautz. Fully-connected crfs with non-parametric pairwise potential. In *Proceedings of the IEEE Conference on Computer Vision and Pattern Recognition*, pages 1658–1665, 2013.

[20] Patrizio Campisi and Karen Egiazarian. *Blind image deconvolution: theory and applications*. CRC press, 2007.

[21] Eyal Carmi, Siuyan Liu, Noga Alon, Amos Fiat, and Daniel Fiat. Resolution enhancement in mri. *Magnetic resonance imaging*, 24(2):133–154, 2006.

[22] Shahab Chitchian, Michael A Fiddy, and Nathaniel M Fried. Denoising during optical coherence tomography of the prostate nerves via wavelet shrinkage using dual-tree complex wavelet transform. *Journal of Biomedical Optics*, 14(1):014031–014031, 2009.

[23] Taeg Sang Cho, Neel Joshi, C Lawrence Zitnick, Sing Bing Kang, Richard Szeliski, and William T Freeman. A content-aware image prior. In *Computer Vision and Pattern Recognition (CVPR), 2010 IEEE Conference on*, pages 169–176. IEEE, 2010.

[24] Roberto Cipolla, Sebastiano Battiato, and Giovanni Maria Farinella. *Computer Vision: Detection, recognition and reconstruction*, volume 285. Springer, 2010.

[25] Christakis Constantinides. *Magnetic Resonance Imaging: The Basics*. CRC press, 2014.

[26] Ibrahim Ben Daya, Albert IH Chen, Mohammad Javad Shafiee, Alexander Wong, and John TW Yeow. Compensated row-column ultrasound imaging system using fisher tippett multilayered conditional random field model. *PloS one*, 10(12), 2015.

[27] Arunabha Debnath, Hari Mohan Rai, Chahat Yadav, Anjali Agarwal, and Ankit Bhatia. Deblurring and denoising of magnetic resonance images using blind deconvolution method. *International Journal of Computer Applications*, 81(10), 2013.

[28] AE Desjardins, BJ Vakoc, WY Oh, SM Motaghiannezam, GJ Tearney, and BE Bouma. Angle-resolved optical coherence tomography with sequential angular selectivity for speckle reduction. *Optics express*, 15(10):6200–6209, 2007.

[29] Wolfgang Drexler and James G Fujimoto. *Optical coherence tomography: technology and applications*. Springer Science & Business Media, 2008.

[30] Wolfgang Drexler and James G Fujimoto. *Optical coherence tomography: technology and applications*. Springer Science & Business Media, 2015.

[31] Jinming Duan, Wenqi Lu, Christopher Tench, Irene Gottlob, Frank Proudlock, Niraj Nilesh Samani, and Li Bai. Denoising optical coherence tomography using second order total generalized variation decomposition. *Biomedical Signal Processing and Control*, 24:120–127, 2016.

[32] David Duvenaud, Benjamin Marlin, and Kevin Murphy. Multiscale conditional random fields for semi-supervised labeling and classification. In *Computer and Robot Vision (CRV), 2011 Canadian Conference on*, pages 371–378. IEEE, 2011.

[33] P ERDdS and A R&WI. On random graphs i. *Publ. Math. Debrecen*, 6:290–297, 1959.

[34] Adolf F Fercher, Wolfgang Drexler, Christoph K Hitzenberger, and Theo Lasser. Optical coherence tomography-principles and applications. *Reports on progress in physics*, 66(2):239, 2003.

[35] Adolf F Fercher, Christoph K Hitzenberger, Markus Sticker, Robert Zawadzki, Boris Karamata, and Theo Lasser. Numerical dispersion compensation for partial coherence interferometry and optical coherence tomography. *Optics Express*, 9(12):610–615, 2001.

[36] AF Fercher, CK Hitzenberger, Markus Sticker, Robert Zawadzki, Boris Karamata, and Theo Lasser. Dispersion compensation for optical coherence tomography depth-scan signals by a numerical technique. *Optics Communications*, 204(1):67–74, 2002.

[37] Giorgio Franceschetti, Vito Pascazio, and Gilda Schirinzi. Iterative homomorphic technique for speckle reduction in synthetic-aperture radar imaging. *JOSA A*, 12(4):686–694, 1995.

[38] Nikolas P Galatsanos, Vladimir Z Mesarovic, Rafael Molina, Aggelos K Katsaggelos, and Javier Mateos. Hyperparameter estimation in image restoration problems with partially known blurs. *Optical Engineering*, 41(8):1845–1854, 2002.

[39] Juan J Gómez-Valverde, Juan E Ortuno, Pedro Guerra, Boris Hermann, Behrooz Zabihian, Jose L Rubio-Guivernau, Andres Santos, Wolfgang Drexler, and Maria J Ledesma-Carbayo. Evaluation of speckle reduction with denoising filtering in optical coherence tomography for dermatology. In *Biomedical Imaging (ISBI), 2015 IEEE 12th International Symposium on*, pages 494–497. IEEE, 2015.

[40] Guanghua Gong, Hongming Zhang, and Minyu Yao. Speckle noise reduction algorithm with total variation regularization in optical coherence tomography. *Optics Express*, 23(19):24699–24712, 2015.

[41] Hayit Greenspan. Super-resolution in medical imaging. *The Computer Journal*, 52(1):43–63, 2009.

[42] Manuel Guizar-Sicairos, Samuel T Thurman, and James R Fienup. Efficient subpixel image registration algorithms. *Optics letters*, 33(2):156–158, 2008.

[43] Bahadir Kursat Gunturk and Xin Li. *Image restoration: fundamentals and advances*. CRC Press, 2012.

[44] Jacques Hadamard. Sur les problèmes aux dérivées partielles et leur signification physique. *Princeton university bulletin*, 13(49-52):28, 1902.

[45] Per Christian Hansen. *The L-curve and its use in the numerical treatment of inverse problems*. IMM, Department of Mathematical Modelling, Technical Universityof Denmark, 1999.

[46] Kenneth M Hanson. Introduction to bayesian image analysis. In *Medical Imaging 1993*, pages 716–731. International Society for Optics and Photonics, 1993.

[47] R Harris and G Wesbey. Artifacts in magnetic resonance imaging. In *Magnetic resonance annual. 1988*. 1988.

[48] Qian He and Lihong Huang. Penalized maximum likelihood algorithm for positron emission tomography by using anisotropic median-diffusion. *Mathematical Problems in Engineering*, 2014, 2014.

[49] SA Hojjatoleslami, MRN Avanaki, and A Gh Podoleanu. Image quality improvement in optical coherence tomography using lucy–richardson deconvolution algorithm. *Applied optics*, 52(23):5663–5670, 2013.

[50] Timothy J Holmes and Yi-Hwa Liu. Richardson-lucy/maximum likelihood image restoration algorithm for fluorescence microscopy: further testing. *Applied optics*, 28(22):4930–4938, 1989.

[51] Xiaoping Hu, Valen Johnson, Wing H Wong, and Chin-Tu Chen. Bayesian image processing in magnetic resonance imaging. *Magnetic resonance imaging*, 9(4):611–620, 1991.

[52] Yukihide Iwamoto, Xian-Hua Han, So Sasatani, Kazuhiro Taniguchi, Wei Xiong, and Yen-Wei Chen. Super-resolution of mr volumetric images using sparse representation and self-similarity. In *Pattern Recognition (ICPR), 2012 21st International Conference on*, pages 3758–3761. IEEE, 2012.

[53] Hui Ji and Cornelia Fermuller. Robust wavelet-based super-resolution reconstruction: theory and algorithm. *Pattern Analysis and Machine Intelligence, IEEE Transactions on*, 31(4):649–660, 2009.

[54] Zhongping Jian, Lingfeng Yu, Bin Rao, Bruce J Tromberg, and Zhongping Chen. Three-dimensional speckle suppression in optical coherence tomography based on the curvelet transform. *Optics express*, 18(2):1024–1032, 2010.

[55] Thomas Martini Jørgensen, Jakob Thomadsen, Ulrik Christensen, Wael Soliman, and Birgit Sander. Enhancing the signal-to-noise ratio in ophthalmic optical coherence tomography by image registrationmethod and clinical examples. *Journal of biomedical optics*, 12(4):041208–041208, 2007.

[56] Rinku Kalotra and Sh Anil Sagar. A review: A novel algorithm for blurred image restoration in the field of medical imaging. *International Journal of Advanced Research in Computer and Communication Engineering*, 3(6), 2014.

[57] Gerda Kamberova. Markov random field models: a bayesian approach to computer vision problems. *Technical Reports (CIS)*, page 491, 1992.

[58] Zahra Karimaghaloo, Douglas L Arnold, and Tal Arbel. Adaptive multi-level conditional random fields for detection and segmentation of small enhanced pathology in medical images. *Medical image analysis*, 27:17–30, 2016.

[59] DA Karras, BG Mertzios, D Graveron-Demilly, and D van Ormondt. Improved bayesian mri reconstruction involving neural priors based on a regularization approach. In *Neural Networks, 2003. Proceedings of the International Joint Conference on*, volume 1, pages 596–600. IEEE, 2003.

[60] Dimitris A Karras, Basil G Mertzios, Danielle Graveron-Demilly, and Dirk van Ormondt. Improved mri mining by integrating support vector machine priors in the bayesian restoration. In *Machine Learning and Data Mining in Pattern Recognition*, pages 325–333. Springer, 2005.

[61] Pushmeet Kohli, Philip HS Torr, et al. Robust higher order potentials for enforcing label consistency. *International Journal of Computer Vision*, 82(3):302–324, 2009.

[62] Denis Kouame and Marie Ploquin. Super-resolution in medical imaging: An illustrative approach through ultrasound. In *Biomedical Imaging: From Nano to Macro, 2009. ISBI'09. IEEE International Symposium on*, pages 249–252. IEEE, 2009.

[63] Philipp Krähenbühl and Vladlen Koltun. Efficient inference in fully connected crfs with gaussian edge potentials. *arXiv preprint arXiv:1210.5644*, 2012.

[64] Philipp Krähenbühl and Vladlen Koltun. Parameter learning and convergent inference for dense random fields. In *Proceedings of the 30th International Conference on Machine Learning (ICML-13)*, pages 513–521, 2013.

[65] Abhishek Kumar, Wolfgang Drexler, and Rainer A Leitgeb. Subaperture correlation based digital adaptive optics for full field optical coherence tomography. *Optics express*, 21(9):10850–10866, 2013.

[66] Abhishek Kumar, Tschackad Kamali, René Platzer, Angelika Unterhuber, Wolfgang Drexler, and Rainer A Leitgeb. Anisotropic aberration correction using region of interest based digital adaptive optics in fourier domain oct. *Biomedical optics express*, 6(4):1124–1134, 2015.

[67] P Krishna Kumar, P Darshan, Sheethal Kumar, Rahul Ravindra, Jeny Rajan, Luca Saba, and Jasjit S Suri. Magnetic resonance image denoising using nonlocal maximum likelihood paradigm in dct-framework. *International Journal of Imaging Systems and Technology*, 25(3):256–264, 2015.

[68] Vadim Kuperman. *Magnetic resonance imaging: physical principles and applications*. Academic Press, 2000.

[69] John Kurhanewicz, Daniel Vigneron, Peter Carroll, and Fergus Coakley. Multiparametric magnetic resonance imaging in prostate cancer: present and future. *Current opinion in urology*, 18(1):71, 2008.

[70] Patrick J La Rivière, Junguo Bian, and Phillip A Vargas. Penalized-likelihood sinogram restoration for computed tomography. *Medical Imaging, IEEE Transactions on*, 25(8):1022–1036, 2006.

[71] Patrick J La Rivière and David M Billmire. Reduction of noise-induced streak artifacts in x-ray computed tomography through spline-based penalized-likelihood sinogram smoothing. *Medical Imaging, IEEE Transactions on*, 24(1):105–111, 2005.

[72] Lubor Ladicky, Craig Russell, Pushmeet Kohli, and Philip HS Torr. Associative hierarchical random fields. *Pattern Analysis and Machine Intelligence, IEEE Transactions on*, 36(6):1056–1077, 2014.

[73] John Lafferty, Andrew McCallum, and Fernando CN Pereira. Conditional random fields: Probabilistic models for segmenting and labeling sequence data. 2001.

[74] Henri Lanteri, Muriel Roche, and Claude Aime. Penalized maximum likelihood image restoration with positivity constraints: multiplicative algorithms. *Inverse problems*, 18(5):1397, 2002.

[75] Chi-Hoon Lee, Russell Greiner, and Osmar Zaïane. Efficient spatial classification using decoupled conditional random fields. In *Knowledge Discovery in Databases: PKDD 2006*, pages 272–283. Springer, 2006.

[76] Chi-Hoon Lee, Mark Schmidt, Albert Murtha, Aalo Bistritz, Jöerg Sander, and Russell Greiner. Segmenting brain tumors with conditional random fields and support vector machines. In *Computer vision for biomedical image applications*, pages 469–478. Springer, 2005.

[77] Chunming Li, Rui Huang, Zhaohua Ding, J Chris Gatenby, Dimitris N Metaxas, and John C Gore. A level set method for image segmentation in the presence of intensity inhomogeneities with application to MRI. *Image Processing, IEEE Transactions on*, 20(7):2007–2016, 2011.

[78] Stan Z Li and S Singh. *Markov random field modeling in image analysis*, volume 3. Springer, 2009.

[79] Norman Lippok, Stéphane Coen, Poul Nielsen, and Frédérique Vanholsbeeck. Dispersion compensation in fourier domain optical coherence tomography using the fractional fourier transform. *Optics express*, 20(21):23398–23413, 2012.

[80] Yiheng Liu, Yanmei Liang, Guoguang Mu, and Xiaonong Zhu. Deconvolution methods for image deblurring in optical coherence tomography. *JOSA A*, 26(1):72–77, 2009.

[81] Yuan-Zhi Liu, Nathan D Shemonski, Steven G Adie, Adeel Ahmad, Andrew J Bower, P Scott Carney, and Stephen A Boppart. Computed optical interferometric tomography for high-speed volumetric cellular imaging. *Biomedical optics express*, 5(9):2988–3000, 2014.

[82] Xin Lu, Zhe Lin, Hailin Jin, Jianchao Yang, and James Z Wang. Image-specific prior adaptation for denoising. *Image Processing, IEEE Transactions on*, 24(12):5469–5478, 2015.

[83] Dorothy Lui, Amen Modhafar, Jeffrey Glaister, Alexander Wong, and Masoom A Haider. Monte Carlo bias field correction in endorectal diffusion imaging. *Biomedical Engineering, IEEE Transactions on*, 61(2):368–380, 2014.

[84] Mark A Lukas. Robust generalized cross-validation for choosing the regularization parameter. *Inverse Problems*, 22(5):1883, 2006.

[85] Anjul Maheshwari and David R Williams. Learning optics using vision. *Biomedical Engineering Center for Visual Science University of Rochester Rochester, NY. Retrieved March*, 5:2014, 2001.

[86] Anh Tien Mai, Fabian Bastin, and Michel Toulouse. On optimization algorithms for maximum likelihood estimation. Technical report, CIRRELT Technical Report, 2014.

[87] Susana Marcos, Patricia Rosales, Lourdes Llorente, Sergio Barbero, and Ignacio Jiménez-Alfaro. Balance of corneal horizontal coma by internal optics in eyes with intraocular artificial lenses: evidence of a passive mechanism. *Vision research*, 48(1):70–79, 2008.

[88] Joanne Markham and José-Angel Conchello. Fast maximum-likelihood image-restoration algorithms for three-dimensional fluorescence microscopy. *JOSA A*, 18(5):1062–1071, 2001.

[89] Daniel L Marks, Amy L Oldenburg, J Joshua Reynolds, and Stephen A Boppart. Autofocus algorithm for dispersion correction in optical coherence tomography. *Applied optics*, 42(16):3038–3046, 2003.

[90] Daniel L Marks, Amy L Oldenburg, J Joshua Reynolds, and Stephen A Boppart. Digital algorithm for dispersion correction in optical coherence tomography for homogeneous and stratified media. *Applied optics*, 42(2):204–217, 2003.

[91] Pablo Márquez-Neila, Pushmeet Kohli, Carsten Rother, and Luis Baumela. Non-parametric higher-order random fields for image segmentation. In *Computer Vision–ECCV 2014*, pages 269–284. Springer, 2014.

[92] K Mathew and S Shibu. Wavelet based technique for super resolution image reconstruction. 2011.

[93] Markus A Mayer, Anja Borsdorf, Martin Wagner, Joachim Hornegger, Christian Y Mardin, and Ralf P Tornow. Wavelet denoising of multiframe optical coherence tomography data. *Biomedical optics express*, 3(3):572–589, 2012.

[94] David Merino, Chris Dainty, Adrian Bradu, and Adrian Gh Podoleanu. Adaptive optics enhanced simultaneous en-face optical coherence tomography and scanning laser ophthalmoscopy. *Optics express*, 14(8):3345–3353, 2006.

[95] Peyman Milanfar. *Super-resolution imaging*. CRC press, 2010.

[96] DT Miller, OP Kocaoglu, Q Wang, and S Lee. Adaptive optics and the eye (super resolution oct). *Eye*, 25(3):321–330, 2011.

[97] J Mohan, V Krishnaveni, and Yanhui Guo. A survey on the magnetic resonance image denoising methods. *Biomedical Signal Processing and Control*, 9:56–69, 2014.

[98] Rafael Molina. On the hierarchical bayesian approach to image restoration: applications to astronomical images. *Pattern Analysis and Machine Intelligence, IEEE Transactions on*, 16(11):1122–1128, 1994.

[99] Rafeal Molina, Aggelos K Katsaggelos, and Javier Mateos. Bayesian and regularization methods for hyperparameter estimation in image restoration. *Image Processing, IEEE Transactions on*, 8(2):231–246, 1999.

[100] Snehal More and VV Hanchate. A survey on magnetic resonance image denoising methods. 2016.

[101] Aroop Mukherjee and Soumen Kanrar. Image enhancement with statistical estimation. *arXiv preprint arXiv:1205.1365*, 2012.

[102] Nader M Namazi, N Sibel Goksel, and Ibrahim Miskioglu. A novel approach to image enhancement using the generalized maximum likelihood criterion. In *Circuits and Systems, 1989., Proceedings of the 32nd Midwest Symposium on*, pages 317–320. IEEE, 1989.

[103] Michael K Ng, Huanfeng Shen, Edmund Y Lam, and Liangpei Zhang. A total variation regularization based super-resolution reconstruction algorithm for digital video. *EURASIP Journal on Advances in Signal Processing*, 2007(1):1–16, 2007.

[104] Nhat Nguyen, Peyman Milanfar, and Gene Golub. A computationally efficient superresolution image reconstruction algorithm. *Image Processing, IEEE Transactions on*, 10(4):573–583, 2001.

[105] Nhat Nguyen, Peyman Milanfar, and Gene Golub. Efficient generalized cross-validation with applications to parametric image restoration and resolution enhancement. *Image Processing, IEEE Transactions on*, 10(9):1299–1308, 2001.

[106] Joao P Oliveira, Mario AT Figueiredo, and Jose M Bioucas-Dias. Parametric blur estimation for blind restoration of natural images: linear motion and out-of-focus. *Image Processing, IEEE Transactions on*, 23(1):466–477, 2014.

[107] Jose Orlando, Elena Prokofyeva, and Matthew Blaschko. A discriminatively trained fully connected conditional random field model for blood vessel segmentation in fundus images. 2016.

[108] Aydogan Ozcan, Alberto Bilenca, Adrien E Desjardins, Brett E Bouma, and Guillermo J Tearney. Speckle reduction in optical coherence tomography images using digital filtering. *JOSA A*, 24(7):1901–1910, 2007.

[109] Se Un Park, Nicolas Dobigeon, and Alfred O Hero. Semi-blind sparse image reconstruction with application to mrfm. *Image Processing, IEEE Transactions on*, 21(9):3838–3849, 2012.

[110] Varsha Hemant Patil and Dattatraya S Bormane. Interpolation for super resolution imaging. In *Innovations and Advanced Techniques in Computer and Information Sciences and Engineering*, pages 483–489. Springer, 2007.

[111] Nurmohammed Patwary and Chrysanthe Preza. Image restoration for three-dimensional fluorescence microscopy using an orthonormal basis for efficient representation of depth-variant point-spread functions. *Biomedical optics express*, 6(10):3826–3841, 2015.

[112] Thierry Pecot, Anatole Chessel, Sabine Bardin, Jean Salamero, Patrick Bouthemy, and Charles Kervrann. Conditional random fields for object and background estimation in fluorescence video-microscopy. In *Biomedical Imaging: From Nano to Macro, 2009. ISBI'09. IEEE International Symposium on*, pages 734–737. IEEE, 2009.

[113] Michael Pircher, Erich Go, Rainer Leitgeb, Adolf F Fercher, Christoph K Hitzenberger, et al. Speckle reduction in optical coherence tomography by frequency compounding. *Journal of Biomedical Optics*, 8(3):565–569, 2003.

[114] Carlos Platero and M Carmen Tobar. A label fusion method using conditional random fields with higher-order potentials: Application to hippocampal segmentation. *Artificial intelligence in medicine*, 64(2):117–129, 2015.

[115] P Premaratne and CC Ko. Parametric modeling of blurred images for image restoration. In *Signals, Systems and Computers, 2000. Conference Record of the Thirty-Fourth Asilomar Conference on*, volume 2, pages 1727–1730. IEEE, 2000.

[116] Prabakar Puvanathasan and Kostadinka Bizheva. Interval type-ii fuzzy anisotropic diffusion algorithm for speckle noise reduction in optical coherence tomography images. *Optics express*, 17(2):733–746, 2009.

[117] Ariadna Quattoni, Michael Collins, and Trevor Darrell. Conditional random fields for object recognition. In *Advances in neural information processing systems*, pages 1097–1104, 2004.

[118] Ashish Raj, Yi Wang, and Ramin Zabih. A maximum likelihood approach to parallel imaging with coil sensitivity noise. *Medical Imaging, IEEE Transactions on*, 26(8):1046–1057, 2007.

[119] Deepu Rajan and Subhasis Chaudhuri. Generalized interpolation and its application in super-resolution imaging. *Image and Vision Computing*, 19(13):957–969, 2001.

[120] Jeny Rajan, Ben Jeurissen, Marleen Verhoye, Johan Van Audekerke, and Jan Sijbers. Maximum likelihood estimation-based denoising of magnetic resonance images using restricted local neighborhoods. *Physics in medicine and biology*, 56(16):5221, 2011.

[121] Tyler S Ralston, Steven G Adie, Daniel L Marks, Stephen A Boppart, and P Scott Carney. Cross-validation of interferometric synthetic aperture microscopy and optical coherence tomography. *Optics letters*, 35(10):1683–1685, 2010.

[122] Tyler S Ralston, Daniel L Marks, P Scott Carney, and Stephen A Boppart. Interferometric synthetic aperture microscopy. *Nature Physics*, 3(2):129–134, 2007.

[123] Tyler S Ralston, Daniel L Marks, Farzad Kamalabadi, and Stephen A Boppart. Deconvolution methods for mitigation of transverse blurring in optical coherence tomography. *Image Processing, IEEE Transactions on*, 14(9):1254–1264, 2005.

[124] Satyapal Rathee, Zoly J Koles, and Thomas R Overton. Image restoration in computed tomography: the spatially invariant point spread function. *Medical Imaging, IEEE Transactions on*, 11(4):530–538, 1992.

[125] Irina Rish. An empirical study of the naive Bayes classifier. In *IJCAI 2001 workshop on empirical methods in artificial intelligence*, volume 3, pages 41–46. IBM New York, 2001.

[126] Kosta Ristovski, Vladan Radosavljevic, Slobodan Vucetic, and Zoran Obradovic. Continuous conditional random fields for efficient regression in large fully connected graphs. In *AAAI*, 2013.

[127] M Dirk Robinson, Stephanie J Chiu, JY Lo, CA Toth, JA Izatt, and Sina Farsiu. New applications of super-resolution in medical imaging. *Super-Resolution Imaging*, pages 384–412, 2010.

[128] Matthew D Robson, John C Gore, and R Todd Constable. Measurement of the point spread function in mri using constant time imaging. *Magnetic resonance in medicine*, 38(5):733–740, 1997.

[129] Filip Rooms, Wilfried R Philips, and Javier Portilla. Parametric psf estimation via sparseness maximization in the wavelet domain. In *Optics East*, pages 26–33. International Society for Optics and Photonics, 2004.

[130] Stefan Roth and Michael J Black. Fields of experts: A framework for learning image priors. In *Computer Vision and Pattern Recognition, 2005. CVPR 2005. IEEE Computer Society Conference on*, volume 2, pages 860–867. IEEE, 2005.

[131] Yu A Rozanov. *Markov random fields*. Springer, 1982.

[132] Leonid I Rudin, Stanley Osher, and Emad Fatemi. Nonlinear total variation based noise removal algorithms. *Physica D: Nonlinear Phenomena*, 60(1):259–268, 1992.

[133] Chris Russell. *Higher-Order Inference for Vision Problems*. PhD thesis, Citeseer, 2012.

[134] Harry M Salinas and D Cabrera Fernández. Comparison of pde-based nonlinear diffusion approaches for image enhancement and denoising in optical coherence tomography. *Medical Imaging, IEEE Transactions on*, 26(6):761–771, 2007.

[135] Olivier Salvado, Claudia Hillenbrand, Shaoxiang Zhang, and David L Wilson. Method to correct intensity inhomogeneity in MR images for atherosclerosis characterization. *Medical Imaging, IEEE Transactions on*, 25(5):539–552, 2006.

[136] B Sander, M Larsen, L Thrane, JL Hougaard, and TM Jørgensen. Enhanced optical coherence tomography imaging by multiple scan averaging. *British Journal of Ophthalmology*, 89(2):207–212, 2005.

[137] MJ Shafiee, A Wong, P Siva, and P Fieguth. Efficient bayesian inference using fully connected conditional random fields with stochastic cliques. In *Image Processing (ICIP), 2014 IEEE International Conference on*, pages 4289–4293. IEEE, 2014.

[138] Mohammad Javad Shafiee, Shahid A Haider, Alexander Wong, Dorothy Lui, Andrew Cameron, Ameen Modhafar, Paul Fieguth, and Masoom A Haider. Apparent ultra-high-value diffusion-weighted image reconstruction via hidden conditional random fields. *Medical Imaging, IEEE Transactions on*, 34(5):1111–1124, 2015.

[139] Kritika Sharma and Sheetal Kundra. Restoration of medical images using blind image deconvolution based on ant colony. *International Journal of Computer Applications*, 84(16), 2013.

[140] Nathan D Shemonski, Steven G Adie, Yuan-Zhi Liu, Fredrick A South, P Scott Carney, and Stephen A Boppart. Stability in computed optical interferometric tomography (part i): Stability requirements. *Optics express*, 22(16):19183–19197, 2014.

[141] Kai Shen, Hui Lu, and Michael R Wang. Improving lateral resolution of optical coherence tomography for imaging of skins. In *SPIE BiOS*, pages 97130N–97130N. International Society for Optics and Photonics, 2016.

[142] Guohua Shi, Yun Dai, Ling Wang, Zhihua Ding, Xuejun Rao, and Yudong Zhang. Adaptive optics optical coherence tomography for retina imaging. *Chinese Optics Letters*, 6(6):424–425, 2008.

[143] Jan Sijbers, Arnold Jan den Dekker, Paul Scheunders, and Dirk Van Dyck. Maximum-likelihood estimation of rician distribution parameters. *IEEE Trans. Med. Imaging*, 17(3):357–361, 1998.

[144] Artur Słomski, Zbigniew Rudy, Tomasz Bednarski, Piotr Białas, Eryk Czerwiński, Łukasz Kapłon, Andrzej Kochanowski, Grzegorz Korcyl, Jakub Kowal, Paweł Kowalski, et al. 3d pet image reconstruction based on the maximum likelihood estimation method (mlem) algorithm. *Bio-Algorithms and Med-Systems*, 10(1):1–7, 2014.

[145] Donald L Snyder, Michael I Miller, Lewis J Thomas Jr, and David G Politte. Noise and edge artifacts in maximum-likelihood reconstructions for emission tomography. *Medical Imaging, IEEE Transactions on*, 6(3):228–238, 1987.

[146] Jian Sun, Jian Sun, Zongben Xu, and Heung-Yeung Shum. Image super-resolution using gradient profile prior. In *Computer Vision and Pattern Recognition, 2008. CVPR 2008. IEEE Conference on*, pages 1–8. IEEE, 2008.

[147] Charles Sutton and Andrew McCallum. An introduction to conditional random fields. *Machine Learning*, 4(4):267–373, 2011.

[148] Maciej Szkulmowski and Maciej Wojtkowski. Averaging techniques for oct imaging. *Optics express*, 21(8):9757–9773, 2013.

[149] Hao Tan and Yibin Zheng. Point spread function optimization for mri reconstruction. *algorithms*, 10:12, 2005.

[150] Jing Tang and Arman Rahmim. Bayesian pet image reconstruction incorporating anato-functional joint entropy. *Physics in medicine and biology*, 54(23):7063, 2009.

[151] Marshall F Tappen, Bryan C Russell, and William T Freeman. Exploiting the sparse derivative prior for super-resolution and image demosaicing. In *In IEEE Workshop on Statistical and Computational Theories of Vision*. Citeseer, 2003.

[152] B Thiagarajan and R Bremananth. Brain image segmentation using conditional random field based on modified artificial bee colony optimization algorithm. *Recent Adv. Comput. Sci*, pages 93–106, 2014.

[153] Eric Thiébaut. Introduction to image reconstruction and inverse problems. In *Optics in Astrophysics*, pages 397–422. Springer, 2006.

[154] Andrej Nikolaevich Tikhonov and Vasiliy Yakovlevich Arsenin. Solutions of ill-posed problems. 1977.

[155] Akihito Uji, Tomoaki Murakami, Shigeta Arichika, Yuki Muraoka, Shin Yoshitake, Yoko Dodo, and Nagahisa Yoshimura. Enhanced-resolution optical coherence tomography imaging. *Ophthalmologica*, 235(3):163–172, 2016.

[156] Eric Van Reeth, Ivan WK Tham, Cher Heng Tan, and Chueh Loo Poh. Super-resolution in magnetic resonance imaging: A review. *Concepts in Magnetic Resonance Part A*, 40(6):306–325, 2012.

[157] Gijs van Soest, Martin Villiger, Evelyn Regar, Guillermo J Tearney, Brett E Bouma, and Antonius FW van der Steen. Frequency domain multiplexing for speckle reduction in optical coherence tomography. *Journal of biomedical optics*, 17(7):0760181–0760187, 2012.

[158] Maria Vinas, Carlos Dorronsoro, Daniel Cortes, Daniel Pascual, and Susana Marcos. Longitudinal chromatic aberration of the human eye in the visible and near infrared from wavefront sensing, double-pass and psychophysics. *Biomedical optics express*, 6(3):948–962, 2015.

[159] Vibhav Vineet, Jonathan Warrell, Paul Sturgess, and Philip HS Torr. Improved initialization and gaussian mixture pairwise terms for dense random fields with mean-field inference. In *BMVC*, pages 1–11, 2012.

[160] Vibhav Vineet, Jonathan Warrell, and Philip HS Torr. Filter-based mean-field inference for random fields with higher-order terms and product label-spaces. *International Journal of Computer Vision*, 110(3):290–307, 2014.

[161] Uro Vovk, Franjo Pernus, and Botjan Likar. A review of methods for correction of intensity inhomogeneity in mri. *IEEE transactions on medical imaging*, 26(3):405–421, 2007.

[162] Li-Li Wang and Nelson HC Yung. Improved hierarchical conditional random field model for object segmentation. *Machine Vision and Applications*, 26(7-8):1027–1043, 2015.

[163] Shan Wang, Seung-Hoon Kim, Yue Liu, Hang-Ki Ryu, and Hyo-Moon Cho. Super-resolution algorithm based on discrete fourier transform. In *Advanced Intelligent Computing Theories and Applications. With Aspects of Artificial Intelligence*, pages 368–375. Springer, 2010.

[164] Shenlong Wang, Lei Zhang, and Yan Liang. Nonlocal spectral prior model for low-level vision. In *Computer Vision–ACCV 2012*, pages 231–244. Springer, 2012.

[165] Yun-Heng Wang, Jun-Bao Li, and Ping Fu. Medical image super-resolution analysis with sparse representation. In *Intelligent Information Hiding and Multimedia Signal Processing (IIH-MSP), 2012 Eighth International Conference on*, pages 106–109. IEEE, 2012.

[166] Christian Wojek and Bernt Schiele. A dynamic conditional random field model for joint labeling of object and scene classes. In *Computer Vision–ECCV 2008*, pages 733–747. Springer, 2008.

[167] Maciej Wojtkowski, Vivek J Srinivasan, Tony H Ko, James G Fujimoto, Andrzej Kowalczyk, and Jay S Duker. Ultrahigh-resolution, high-speed, fourier domain optical coherence tomography and methods for dispersion compensation. *Optics express*, 12(11):2404–2422, 2004.

[168] Alexander Wong, Xiao Yu Wang, and Maud Gorbet. Bayesian-based deconvolution fluorescence microscopy using dynamically updated nonstationary expectation estimates. *Scientific reports*, 5, 2015.

[169] Peter D Woolliams, Robert A Ferguson, Christian Hart, Alex Grimwood, and Peter H Tomlins. Spatially deconvolved optical coherence tomography. *Applied optics*, 49(11):2014–2021, 2010.

[170] Mon-Ju Wu, Joseph Karls, Sarah Duenwald-Kuehl, Ray Vanderby Jr, and William Sethares. Spatial and frequency-based super-resolution of ultrasound images. *Computer Methods in Biomechanics and Biomedical Engineering: Imaging & Visualization*, 2(3):146–156, 2014.

[171] Huanyu Xu, Quansen Sun, Nan Luo, Guo Cao, and Deshen Xia. Iterative nonlocal total variation regularization method for image restoration. *PloS one*, 8(6):e65865, 2013.

[172] Jianchao Yang, John Wright, Thomas S Huang, and Yi Ma. Image super-resolution via sparse representation. *Image Processing, IEEE Transactions on*, 19(11):2861–2873, 2010.

[173] Alparslan Yildiz and Yusuf Sinan Akgul. A gradient descent approximation for graph cuts. In *Pattern Recognition*, pages 312–321. Springer, 2009.

[174] Lingfeng Yu, Bin Rao, Jun Zhang, Jianping Su, Qiang Wang, Shuguang Guo, and Zhongping Chen. Improved lateral resolution in optical coherence tomography by digital focusing using two-dimensional numerical diffraction method. *Optics express*, 15(12):7634–7641, 2007.

[175] TS Zaccheo and RA Gonsalves. Iterative maximum-likelihood estimators for positively constrained objects. *JOSA A*, 13(2):236–242, 1996.

[176] Robert J Zawadzki, Steven M Jones, Suman Pilli, Sandra Balderas-Mata, Dae Yu Kim, Scot S Olivier, and John S Werner. Integrated adaptive optics optical coherence tomography and adaptive optics scanning laser ophthalmoscope system for simultaneous cellular resolution in vivo retinal imaging. *Biomedical optics express*, 2(6):1674–1686, 2011.

[177] Huairen Zeng and R Todd Constable. Image distortion correction in epi: comparison of field mapping with point spread function mapping. *Magnetic Resonance in Medicine*, 48(1):137–146, 2002.

[178] Yimeng Zhang and Tsuhan Chen. Efficient inference for fully-connected crfs with stationarity. In *Computer Vision and Pattern Recognition (CVPR), 2012 IEEE Conference on*, pages 582–589. IEEE, 2012.

[179] Ji Zhao, Yanfei Zhong, and Liangpei Zhang. Detail-preserving smoothing classifier based on conditional random fields for high spatial resolution remote sensing imagery. *Geoscience and Remote Sensing, IEEE Transactions on*, 53(5):2440–2452, 2015.

[180] Ningning Zhao, Adrian Basarab, Denis Kouame, and J-Y Tourneret. Restoration of ultrasound images using a hierarchical bayesian model with a generalized gaussian prior. In *Image Processing (ICIP), 2014 IEEE International Conference on*, pages 4577–4581. IEEE, 2014.

[181] Yuanjie Zheng, Murray Grossman, Suyash P Awate, and James C Gee. Automatic correction of intensity nonuniformity from sparseness of gradient distribution in medical images. In *Medical Image Computing and Computer-Assisted Intervention–MICCAI 2009*, pages 852–859. Springer, 2009.

[182] Yingying Zhu, Nandita M Nayak, and Amit K Roy-Chowdhury. Context-aware activity modeling using hierarchical conditional random fields. *Pattern Analysis and Machine Intelligence, IEEE Transactions on*, 37(7):1360–1372, 2015.